Theory of electronic structure and transport in heterostructure nanowires

Viñas Boström, Florinda

2020

Citation for published version (APA):
Viñas Boström, F. (2020). *Theory of electronic structure and transport in heterostructure nanowires*. [Doctoral Thesis (compilation), Solid State Physics]. Department of Physics, Lund University.

Total number of authors:
1

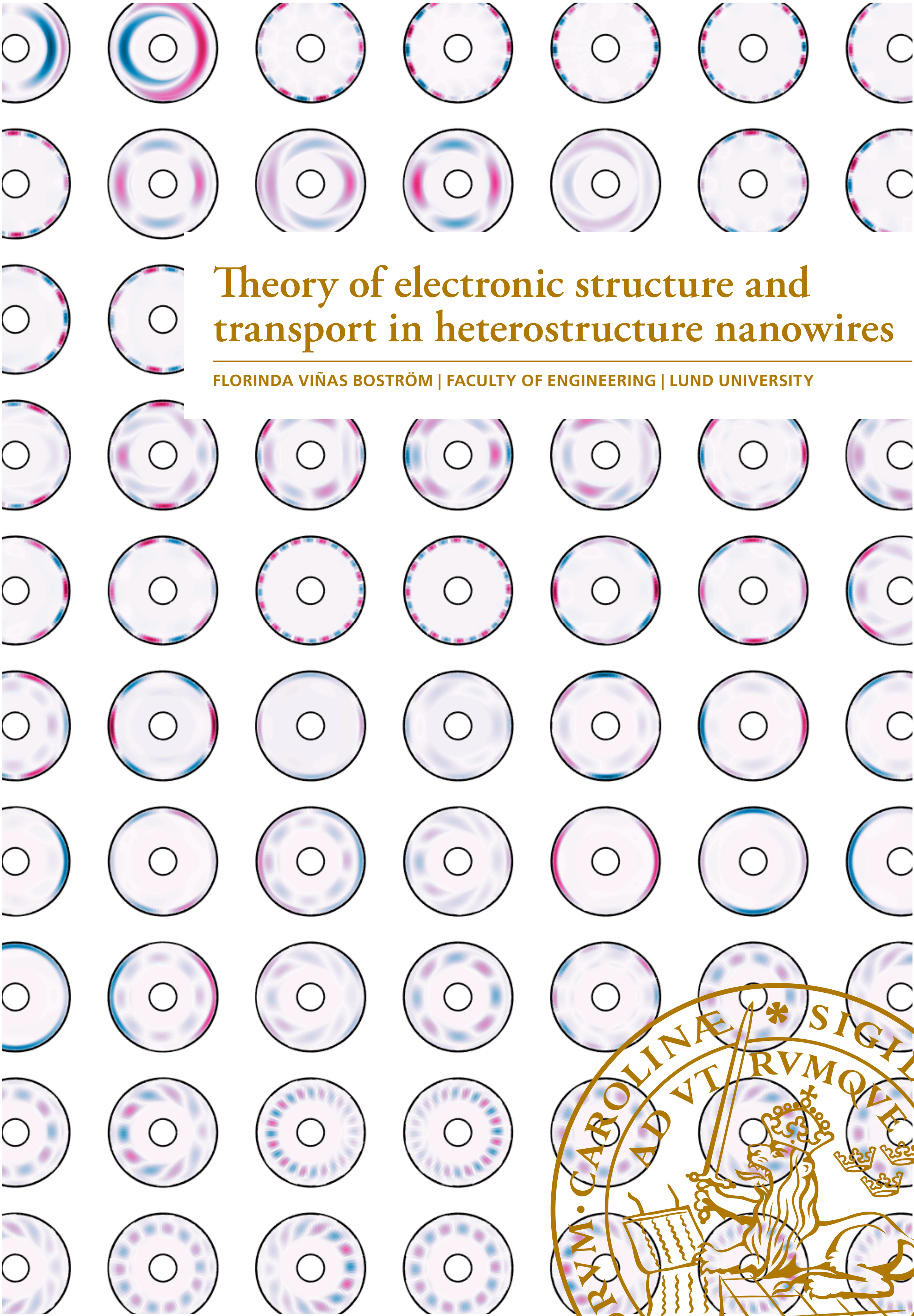

Theory of electronic structure and transport in heterostructure nanowires

FLORINDA VIÑAS BOSTRÖM | FACULTY OF ENGINEERING | LUND UNIVERSITY

Printed by Media-Tryck, Lund 2020 NORDIC SWAN ECOLABEL 3041 0903

LUND
UNIVERSITY

Lund University
Faculty of Engineering
Department of Physics

ISBN 978-91-7895-492-6

9 789178 954926

Theory of electronic structure and transport in heterostructure nanowires

Theory of electronic structure and transport in heterostructure nanowires

by Florinda Viñas Boström

LUND
UNIVERSITY

Thesis for the degree of Doctor of Philosophy

Thesis advisors: Assoc. Prof. Martin Leijnse,
Assoc. Prof. Claes Thelander and Prof. Stephanie Reimann

Faculty opponent: Prof. Milena Grifoni

To be presented, with the permission of the Faculty of Engineering of Lund University, for public criticism in the Rydberg lecture hall (Rydbergsalen) at the Division of Solid State Physics
Department of Physics on Friday, the 8th of May 2020 at 9:00.

Organization
LUND UNIVERSITY

Division of Solid State Physics
Department of Physics
Box 118, SE–221 00 LUND
Sweden

Document name
DOCTORAL DISSERTATION

Date of disputation
2020-05-08

Sponsoring organization

Author(s)
Florinda Viñas Boström

Title and subtitle
Theory of electronic structure and transport in heterostructure nanowires

Abstract

Today, semi-conductor nanowires can be grown with very high precision, using epitaxy. This allows for studies of new nanowire-based quantum devices, likely to be part of novel quantum technologies in the future. This thesis concerns nanostructures based on InAs nanowires. More specifically, it concerns the theoretical treatment of two types of nanowire-based structures: InAs/GaSb core-shell (and core-shell-shell) nanowires, and parallel double quantum dots, made from epitaxially defined single quantum dots in InAs, confined using wurtzite barriers.

For the core-shell(-shell) nanowires, we focus on the band structure of the system, using $\mathbf{k} \cdot \mathbf{p}$ theory to calculate the k-dependent energies and space dependent wave functions. We find that, for the right core and shell thicknesses, a so-called hybridization gap opens up. A hybridization gap is a band gap where conduction- and valence band-like states are inverted, but a band gap appears because of coupling between these bands. In a quantum well such an inverted band gap gives rise to topological edge states. For hollow core-shell-shell InAs/GaSb nanowires, that can be thought up as “rolled-up” quantum wells, we study the wave functions for a finite system, and establish that there are localized end-states, with energies inside the bulk gap. However, in contrast to the topological edge states in two dimensions, the end states are not robust against perturbations.

We have also studied parallel double quantum dots in InAs nanowires. The double quantum dots are created by our experimental collaborators, using a new method, from a single quantum dot in a nanowire, subject to positive side gates. By tuning the side gates the interaction between the two dots formed can be tuned. The double quantum dots are investigated in collaboration with experimentalists, where they are subject to a bias voltage and an external magnetic field. The measured transport data can be very well reproduced using a few-body Hamiltonian for the dot system together with a master equation. We find that in the two-electron regime, the ground state can be tuned between a singlet and a triplet state, either by tuning the side gates or the external magnetic field. At the ground state transition the singlet and triplet states anticross, resulting in an energy difference that can be affected by changing the dot interaction.

It is likely that nanowire-based structures like these will be used in future quantum technologies, and it is then important to understand and model the structure-dependent electronic energies depending on e.g., spin-orbit coupling and large g-factors.

DOKUMENTDATABLAD enl SIS 61 41 21

Key words
electronic structure, electron transport, nano, quantum, InAs, GaSb, topological, nanowires, quantum dots

Classification system and/or index terms (if any)

Supplementary bibliographical information

Language
English

ISSN and key title

ISBN
978-91-7895-492-6 (print)
978-91-7895-493-3 (pdf)

Recipient's notes

Number of pages
151

Price

Security classification

I, the undersigned, being the copyright owner of the abstract of the above-mentioned dissertation, hereby grant to all reference sources the permission to publish and disseminate the abstract of the above-mentioned dissertation.

Signature Florinda Viñas Boström

Date 2020-03-26

Theory of electronic structure and transport in heterostructure nanowires

by Florinda Viñas Boström

LUND
UNIVERSITY

A doctoral thesis at a university in Sweden takes either the form of a single, cohesive research study (monograph) or a summary of research papers (compilation thesis), which the doctoral student has written alone or together with one or several other author(s).

In the latter case the thesis consists of two parts. An introductory text puts the research work into context and summarizes the main points of the papers. Then, the research publications themselves are reproduced, together with a description of the individual contributions of the authors. The research papers may either have been already published or are manuscripts at various stages (in press, submitted, or in draft).

Cover illustration: Wave functions (real part) for InAs/GaSb core-shell-shell nanowires.

Faculty of Engineering, Division of Solid State Physics
Department of Physics
ISBN: 978-91-7895-492-6 (print)
ISBN: 978-91-7895-493-3 (pdf)

Printed in Sweden by Media-Tryck, Lund University, Lund 2020

To Emil,
to Domingo,
and to my mother

Contents

Acknowledgements

During my PhD I received a lot of help form many people. Even though I would like to acknowledge them all here, I have only compiled a short list of the most central persons who helped me with my work.

First: a very big thank you to my supervisors! Martin, for being a great supervisor but also for your personal support during times when I needed it. I admire your deep interest in physics and your ambition, but also your ability to sort out what is important (and what is not so important). Claes for being a good discussion partner and for your patience with theorists! Stephanie for always keeping your door open.

I would like to thank everyone at FTF who have helped me in one way or another. People who left the division: Malin, for teaching me about quantum dots, experimental work and manners. Michael, it was truly an inspiration working with you. Thank you to everyone in my group: Martin J for being a rock, for keeping a positive attitude, and for encouraging a nice work-life balance. Rubén for good chats and for encouraging my future career. Athanasios, for all the hard work you have put in for our collaboration, and for enduring my stress while writing my thesis. Simon, thank you for all the good jokes! Dan, for being a great boss and for giving me a cat!

My office mates: Elke, David and Kristi, a big thank you for keeping up the best office at the division and for being great at Christmas decorations.

A big thank you to all PhD students and postdocs at FTF, you really make our workplace great!

I would also like to thank everyone at mathematical physics! Peter - thank you for helping me to choose to pursue a PhD in physics. A special thank you to Katarina for endless support to me, and to everyone else. Claudio, thank you for your kindness.

A special thank you to all of my friends, you know who you are! Tack till Maja och Knut, ni är bäst! A very big and special thank you goes to my family. Mamma, för att du alltid stöttat mig även när jag inte ens har kunnat förklara vad jag jobbar med. För att du alltid finns där både för mig och Domingo.

Emil! Thank you for tricking me into staying in physics and for always supporting me (mentally, physically and with physics). Also, thank you for helping me with practical stuff (like installing fortan libraries) and for helping me to understand that I actually know a lot of physics by now! By the way, you are still the only guy who I can ask about math (you somehow know more than anyone else). And thank you for being the best dad ever!

Mingo - tack för att du finns och visar mig vad som verkligen är viktigt.

List of publications (with author contributions)

This thesis is based on the following publications, referred to by their Roman numerals:

I **Extracting band structure characteristics of GaSb/InAs core-shell nanowires from thermoelectric properties**

Florinda Viñas, H.Q. Xu, Martin Leijnse
Physical Review B **95**, 115420 (2017)

I wrote the code and carried out the calculations. I analyzed the results together with ML and HQX. I wrote the paper with input from all authors and made all the figures.

II **Band structure and end states in InAs/GaSb core-shell-shell nanowires**

Florinda Viñas Boström, Athanasios Tsintzis, Michael Hell, Martin Leijnse
Manuscript, in preparation

I came up with the idea and planned the project together with MH and ML. I was the main responsible for the project. I wrote the $\mathbf{k} \cdot \mathbf{p}$ code and made the $\mathbf{k} \cdot \mathbf{p}$ calculations. I participated in analyzing the results from the BHZ calculations together with the co-authors. I wrote the main parts of the paper and made the figures together with AT.

III **Tuning the Two-Electron Hybridization and Spin States in Parallel-Coupled InAs Quantum Dots**

Malin Nilsson, **Florinda Viñas Boström**, Sebastian Lehmann, Kimberly A. Dick, Martin Leijnse, Claes Thelander
Physical Review Letters **121**, 156802 (2018)

I was the first theory author, carried out the calculations, and was involved in analyzing the measurement data and the theory results. I wrote the theory part of the paper (supplemental information) and provided feedback on the rest of the paper.

iv **Spectroscopy and level detuning of few-electron spin states in parallel InAs quantum dots**

Claes Thelander, Malin Nilsson, **Florinda Viñas Boström**, Adam Burke, Sebastian Lehmann, Kimberly A. Dick, Martin Leijnse
Physical Review B **98**, 245305 (2018)

I was the first theory author, carried out the calculations, and was involved in analyzing the measurement data and the theory results. I wrote the theory part of the paper (supplemental information) and provided feedback on the rest of the paper.

All papers are reproduced with permission of their respective publishers.

Popular summary in English

The reason I find nanophysics so fascinating is that we can build and study new quantum mechanical systems. Nowadays it is possible to create and engineer systems, so small that quantum mechanics describes their physics, in a laboratory! These small nanostructures can in principle have any shape and consist of different materials, what they have in common is their size: they are on the scale of around $1 - 100$ nm (nanometer). One nm is 10^{-9} m or one billionth of a meter. This means that in one meter there are $1,000,000,000$ nm! I know this might not be so easy to grasp, so let's make a comparison: a nanostructure of tens of nm is roughly the same size as a smaller virus, but ten to a hundred times larger than an atom. However, it is a hundred times smaller than typical bacteria, and less than a thousand times smaller than the thickness of a strand of hair!

Like everything else around us, the nanostructures are made of atoms. The atoms consists of nuclei and electrons, and when the atoms are put together some electrons can move around between the atoms. The electrons are electrically charged, so when they move they can carry an electrical current. However, the electrons are not really free! They are affected by the confinement inside the small nanostructures and are restricted to have certain energies (this is an effect of quantum mechanics).

To find information about the electrons we use mathematical models, and calculate the electrons energies. To model something very small we need to use a quantum mechanical description.

Quantum mechanics is something else than the world we are used to in our everyday lives. As the name suggests, in the small world, things (such as energy) come in packages or *quanta*. Briefly, this means that for small systems, particles or atoms, there are only certain allowed energies, so that only specific velocities, positions or colors are allowed. This has implications in the big world as well! For example, to understand why metals can conduct currents, one needs to use a quantum mechanical description of the atoms in the metal! Another example is gems: their transparency, colors and good insulating properties can only be explained using quantum mechanics.

A prerequisite for the electrons to be able to move around inside a structure is that the material in the system is either a metal or a semiconductor. In a metal, electrons can move under all circumstances, while in a semiconductor the electrons can move only under certain circumstances. This means that a semiconductor sometimes can carry a current, depending on circumstances such as temperature, system size, applied electric field etc. In addition to being an electrically charged particle, the electron is also like a tiny magnet! It has a property called *spin*, that reacts to magnetic fields similar to a compass needle, and can align with a magnetic field.

The energies that are allowed in a nanostructure is to a large extent determined by its shape, size, and material. This means that if we know these things about the nanostructure we can calculate how the electrons will "behave" inside! In fact, inside the nanostructures, the electrons are the only things that we can affect in the systems, since they are the only thing that can move at all. They have electric charge that reacts to voltages and spins that react to magnetic fields.

This thesis concerns electrons inside two different nano "shapes" made of semiconductors: nanowires and quantum dots. Nanowires are small cylinders, and I have studied a special type called a core-shell nanowire. This structure consists of a core (a cylinder) with one or several "shells" of different materials. In a nanowire the electrons can move in one direction only, along the wire. Quantum dots are small in all directions, so the electrons inside cannot move. The quantum dots I have studied are actually made of nanowires, but only from very small segments, so they look like little discs. The electronic properties of the nanowires and the quantum dots can be altered by changing the thickness of the nanowire (or its shells) or by applying a voltage or a magnetic field to the structures.

In the core-shell nanowires, I have studied the effects of interacting electrons and so-called holes. Holes are here the name for a "missing electron" in a large electron quantity (leaving a hole where the missing electron should have been). I have found that in the core-shell nanowires electrons and holes interact and mix, and can live in both the core and the shell simultaneously. I have also suggested how this effect can be seen from experimental electrical measurements. Furthermore, in special cases, some electrons can live only at the ends of the wire!

For the quantum dots, I have collaborated with experimentalists, and together we have investigated the properties of two neighboring quantum dots, where the electrons inside one quantum dot can sense electrons in the other quantum dot. The two neighboring quantum dots are made using a new technique: from a single quantum dot two quantum dots are formed by creating two separate pockets for the electrons. This new method makes it possible to control how much the two quantum dots can interact! This means that if we have two electrons, one in each quantum dot, we can control how the electrons interact and hence how they behave.

In the long run we are interested in applications possibly within electronics and quantum computing. The components of modern electronics are so small that quantum effects are inevitable - in many cases, such as for transistors and LEDs, quantum mechanics is needed to explain how they work. Quantum computers are a new type of computers that function in a different manner than classical computers, by taking advantage of quantum mechanics. They can solve many problems that are impossible for a classical computer to solve. This thesis is a step on the way to finding out how nanowires or quantum dots could be used for these applications.

Populärvetenskaplig sammanfattning på svenska

Idag är det möjligt att konstruera saker som är så små att kvantmekanik behövs för att beskriva dess fysik, och det är dessutom möjligt att designa dessa små strukturers egenskaper i ett laboratorium! Detta är anledningen till att jag tycker nanofysik är så fascinerande - att vi kan bygga och studera nya kvantmekaniska system. Dessa små nanostrukturer kan i princip ha vilken form som helst och bestå av olika material - vad de har gemensamt är storleken: de är ungefär mellan 1 och 100 nanometer (nm) långa. En nm är 10^{-9} m, eller en miljarddels meter. Detta innebär att på en meter går det $1,000,000,000$ nm! Det är inte helt enkelt att förstå hur litet detta faktiskt är, så låt oss göra en jämförelse: en nanostruktur som är några tiotals nm lång har ungefär samma storlek som ett mindre virus, men är tio till hundra gånger större än en atom. Samma nanostruktur är ca hundra gånger mindre än en bakterie, och mer än tusen gånger mindre än tjockleken på ett hårstrå!

Precis som allt annat runt omkring oss är nanostrukturerna uppbyggda av atomer. Varje atom består av en atomkärna och en eller flera elektroner, och när atomerna sätts ihop kan vissa av elektronerna röra sig fritt mellan atomerna. Elektronerna är elektriskt laddade, så när de rör sig utgör de en elektrisk ström. Elektronerna är dock inte helt fria! De påverkas av att de är instängda inuti de små nanostrukturerna och får därför bara anta vissa tillåtna energier (detta är en av konsekvens av kvantmekaniken).

För att ta reda på hur elektronerna beter sig använder vi oss av matematiska modeller och beräknar elektronernas energier. För att kunna modellera något mycket litet måste vi använda en kvantmekanisk beskrivning. Kvantmekaniken beskriver fysik som är väldigt annorlunda än vad vi är vana vid att se i vår vardag. Som namnet antyder är saker (till exempel energi) uppdelade i bestämda mängder, eller kvanta, i den lilla världen. Kort sagt betyder detta att för små system, partiklar eller atomer finns det bara vissa tillåtna energier, så att endast specifika hastigheter, positioner eller färger är tillåtna. Detta har också konsekvenser i den stora världen! Ett exempel på detta är, att för att förstå varför vissa material leder ström, medan andra är isolatorer, måste man använda en kvantmekanisk beskrivning av atomerna i metallen! Ett annat exempel är ädelstenar: deras transparens, färger och dåliga elektriska ledningsförmåga kan förklaras med hjälp av kvantmekanik.

En förutsättning för att elektroner ska kunna röra sig (och bilda en elektrisk ström) inuti ett material, är att materialet antingen är en metall eller en halvledare. I en metall kan elektronerna alltid röra sig, medan elektronerna i en halvledare bara kan röra sig under vissa omständigheter. Detta innebär att en halvledare *ibland* leder ström, beroende på förhållanden såsom hur varmt det är, hur stor materialbit vi har eller om vi har lagt på en elektrisk spänning över materialet.

Vi kan också påverka elektronerna genom att lägga på ett magnetfält. Förutom att vara en elektriskt laddad partikel, så är elektronen också som en liten magnet! Den har en egenskap som kallas *spinn*, som reagerar ett på magnetfält likt en kompassnål och ställer in sig i magnetfältets riktning.

Vilka energier som tillåts i en nanostruktur bestäms till stor del av dess form, storlek och material. Detta innebär att om vi känner till dessa saker om nanostrukturen kan vi räkna ut hur elektronerna kommer att "bete sig" inuti! I nanostrukturerna är det faktiskt bara elektronerna som vi kan påverka, eftersom de ju är det enda som kan röra sig. De har elektrisk laddning som reagerar på spänningar och spinn som reagerar på magnetfält.

Den här avhandlingen handlar om elektroner inuti två olika nanosystem uppbyggda av halvledare: nanotrådar och kvantprickar. Nanotrådar är små cylindrar, och jag har studerat en speciell typ som kallas en kärna-skal nanotråd. Denna struktur består av en kärna (en cylinder) med ett eller flera "skal" som kan bestå av olika halvledarmaterial. I en nanotråd kan elektronerna bara röra sig i en riktning, längs med tråden. Kvantprickar är små i alla riktningar, vilket innebär att elektronerna inuti inte kan röra sig särskilt mycket alls. De kvantprickar jag har studerat är faktiskt tillverkade av nanotrådar, men bara från mycket små segment, så de ser ut som små skivor. Jag har studerat nanotrådar och kvantprickar gjorda av halvledare så att de elektroniska egenskaperna kan ändras genom att ändra tjockleken på nanotråden (eller dess skal) eller genom att lägga på en spänning eller ett magnetfält över strukturerna.

I nanotrådarna har jag räknat på elektroner som växelverkar med så kallade hål. Hål är här namnet på en "elektron som fattas" i en stor mängd elektroner (alltså, ett hål där den försvunna elektronen borde ha varit). Jag har upptäckt att i nanotrådarna med skal,"blandas" elektroner och hål, och blandningen kan finnas i både kärnan och skalet samtidigt. Jag har också föreslagit hur denna effekt kan ses i experiment genom elektriska mätningar. Dessutom har jag sett att under speciella förutsättningar kan vissa elektroner befinna sig endast i trådens ändar!

I arbetet med kvantprickar har jag samarbetat med experimentalister, och tillsammans har vi undersökt egenskaperna hos två närliggande kvantprickar, där elektronerna som befinner sig i en prick kan känna av elektroner i den andra pricken. De två kvantprickarna tillverkas med en ny teknik: en ensam kvantprick kan "delas" och bli till två stycken, genom att två elektron-"fickor" skapas. Denna nya metod gör det möjligt att kontrollera hur mycket de två kvantprickarna kan växelverka! Detta betyder att om vi har två elektroner, en i varje kvantprick, kan vi styra hur elektronerna pratar med varandra, och därmed hur de beter sig.

På lång sikt är vi intresserade av tillämpningar främst inom elektronik och kvantdatorer. Komponenterna i modern elektronik är så små att kvanteffekter är oundvikliga - och i många fall, till exempel för transistorer och lysdioder, behövs kvantmekanik för att förklara hur de fungerar. Kvantdatorer är en ny typ av datorer som fungerar på ett fundamentalt annorlunda sätt jämfört med klassiska datorer - genom att utnyttja kvantmekanik. Dessa nya typer av datorer kommer förhoppningsvis att kunna lösa många problem som är omöjliga för en klassisk dator att lösa. Det är högst troligt att både nanotrådar och kvantprickar kan komma att användas i dessa tillämpningar, och denna avhandling är ett steg på vägen för att ta reda på hur.

Theory of electronic structure and transport in heterostructure nanowires

Part I

Introduction

Chapter 1

Introduction

A large part of condensed matter physics deals with periodic structured materials such as metals and semi-conductors (in contrast to non-crystalline materials). The crystalline periodic structures give rise to electronic bands, which can explain the conductive properties of both metals, insulators, and semi-conductors. The very short explanation for their different behavior is that between the bands, energy gaps open up. If a band just below such a gap is filled with electrons while the first band above the gap is empty, electrons cannot move freely (insulator), whereas in a partly filled band electrons can move and become a current (metal). If the band gap between a filled and an empty band is very small, we call the system a semi-conductor. By creating carriers (e.g., by photo-excitation) above the band gap, the system can carry some current. While some semi-conductors are made up of only one type of atoms, others consist of two (or more) different atoms in a periodic structure. One type of such semi-conductor compounds is the so-called III-V materials. These are crystalline (periodic) materials with two repeating atoms, one from group III and one from group V of the periodic table. This thesis is mainly concerned with two such III-IV compounds: InAs and GaSb.

1.1 Semi-conductor materials and nanostructures

The picture of periodic structures with electronic bands can be seen in contrast to very small nanostructures - quantum dots (QDs) - where the single electron levels are discrete and well-separated from each other. What makes a QD special is that is small in all directions. If we change its extent in space we can tune the difference between the energy levels, making this a very nice system to conduct experiments on, almost like an engineered atom.

Another type of nanostructure is the nanowire; this is as the name suggests a small wire. Since a wire has a much larger extension in one direction than in the other two, we have (approximately) a system with energy bands in one direction, and confinement (like in the QD) in the other two. This means that we can make the wire thicker or thinner, to make the energy bands come closer or further apart. We can also connect this wire (since it is a wire, after all) to an electric circuit relatively easy.

In this thesis we study two types of nanostructures, based on InAs nanowires. In Paper I we look at so-called core-shell nanowires, where an InAs (GaSb) nanowire core has been covered with a GaSb (InAs) shell. In Paper II we study a very similar system to that in Paper I, but with a hole (or an insulator) in the middle of the core. This can be seen as a core-shell-shell nanowire with an insulator core, and an InAs and a GaSb shell. In Papers III and IV we look at double quantum dots (DQDs), situated in InAs nanowires (a DQD is a system of two QDs that can talk to each other). The DQDs we study are connected in parallel to a measurement setup.

1.1.1 Band structure theory

For any one-electron Hamiltonian that describes a lattice periodic system, such as a crystalline solid, we can find the electronic energies as a function of the crystal momentum $\mathbf{k}$. We refer to this as the band structure of the system, since the electronic energies form bands when the electrons are subject to the lattice periodic potential. The theory of electronic band structure is arguably the most important tool to understand solids. It has importance both for analyzing electronic and optical properties, and what can not be found from the band structure, can often be deduced from the corresponding wave functions of the electrons [1].

There are many different approaches to how to model and calculate electronic band structures, the most simple one assuming a free-electron parabola with a modified mass – an effective mass – to adjust for the periodic potential from the atomic lattice. This effective mass model is for most purposes not sufficient to describe semiconductors [2], since it includes only one band, and hence no band gap. On the other side of the spectrum of band structure theories we have the *ab initio* methods. The latin term *ab initio* literally means "from the beginning", and these methods start from the theory of atoms to find the electronic energies, taking the potentials from the nuclei and the electron-electron interactions into account explicitly. While many of these methods, such as Hartree-Fock and density functional theory in the local density approximation take the electron-electron interaction into account through an average field [1], others include the interaction more explicitly, e.g., through many-body perturbation theory [3]. These models are computationally expensive and are limited to bulk systems or small structures [1].

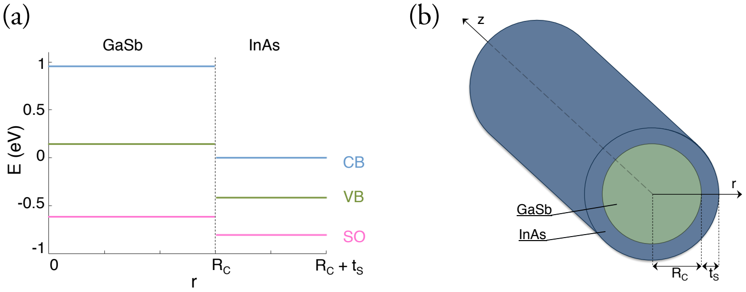

Figure 1.1: (a) Band diagram showing the bulk broken band gap alignment between GaSb and InAs. The band edges are shown for the conduction band (CB), valence band (VB) and split-off band (SO). (b) A core-shell nanowire. Both figures adapted from Paper 1.

For larger systems on the nanoscale (large is a very relative term here), but small enough for quantum confinement effects to be important, we can use an effective model, such as the Kane model of the $\mathbf{k} \cdot \mathbf{p}$ theory. The $\mathbf{k} \cdot \mathbf{p}$ theory is a semiempirical method [4], meaning that we use empirical data as input to our calculations, such as band gap position and band gap size. This model includes several bands, and is not restricted to a parabolic band dispersion. Another type of semi-empirical model is the tight-binding method, where a basis consisting of electronic states localized on individual sites is used. The electrons are allowed to tunnel to the nearby sites, usually tunneling to the neighboring or next-neighboring sites is considered [5]. For the material system studied in this thesis, GaSb and InAs, it is necessary to use a method that includes both conduction and valence bands.

An important part of the Kane model is the spin-orbit coupling (SOC) terms. The SOC is a relativistic effect where the spin of a charged moving particle interacts with the magnetic field that is generated by the moving charge [6]. This effect leads to a splitting of energy levels in atoms, and in semiconductors it causes a splitting of the VBs [7]. The magnitude of this VB splitting is referred to as the split-off gap. For a material such as InAs, it is crucial to include SOC effects in band structure calculations, due to the large split-off gap [8] of this material.

1.2 GaSb/InAs

The III-V material system GaSb/InAs is interesting mainly due to its bulk broken band gap alignment, meaning that the valence band in bulk GaSb lies above the conduction band in bulk InAs, see Fig. 1.1(a). Close to the material interface in a GaSb/InAs heterostructure this band alignment gives rise to hybridizing, spatially separated, electron and hole states, which can lead to a gapped band structure with band inversion. We call a gap in such an inverted structure a hybridization gap, to distinguish it from an ordinary band gap, or from a confinement gap caused by the finite size of a nanostructure.

One reason that the GaSb/InAs material system has gained attention is for its properties in quantum wells (QWs). A QW is a nanostructure, made from a very thin sheet of one, or several, layered, materials. This structure makes the electrons strongly confined in the smallest direction (perpendicular to the sheets). QWs are often referred to as quasi-two-dimensional, since they are approximately two-dimensional objects: if the thin sheets would be infinitely wide and infinitesimally thin, we would have a pure two-dimensional object. However, often the structure in the thin direction is important, such as for heterostructures; we then refer to the QWs as being quasi-two-dimensional. The InAs/GaSb QWs consists of two thin ($\approx 10-20$ nm) layers of GaSb and InAs. It has been suggested that these QWs may host excitonic ground states [9], interesting SOC effects [10], and they are known to be so-called topological insulators (TIs) [11, 12], a concept that will be explained in Chapter 3. The material system of InAs/GaSb has been reported to have interesting properties also in zero dimensions, where coupled and parallel electron-hole QDs have been studied [13, 14]. These QDs are epitaxially defined within core-shell nanowires.

1.3 Core-shell and core-shell-shell nanowires

In Papers I and II we consider core-shell nanowires [15], which are small (around $10-100$ nm in diameter) heterostructures with one semiconductor material in the middle (the core) and one around (the shell), see Fig. 1.1(b). Nanowires made from III-V semiconductor compounds are often hexagonal, but we model them to be cylindrical. Core-shell nanowires have been suggested as components in solar cells [16] and in infrared lasers [17], and they can be grown epitaxially [18, 19, 20] with very good precision. Today it is possible to epitaxially grow core-shell nanowires of GaSb and InAs.

In Paper I we have calculated the band structures of GaSb/InAs and InAs/GaSb core-shell nanowires of dimensions realistic to grow epitaxially. The band structures are used as input to diffusive and ballistic transport calculations to find the conductivities and the Seebeck coefficients for the nanowires. The band structures show far from parabolic bands and there is a large hybridization between electrons and holes.

Today, it is also possible to grow nanowires with multiple shells [15, 13]. In Paper II we propose a core-shell-shell nanowire made of an AlSb inner core and InAs and GaSb shells. The AlSb has a much larger band gap than InAs and GaSb, so it is an insulator. The nanowire could hence be regarded as a hollow core-shell-shell wire, even though in practice it has an inner core of an insulating barrier material, making it suitable for the growth processes available today. We use a BHZ model together with $\mathbf{k} \cdot \mathbf{p}$ theory to calculate the band structures and wave functions of such core-shell nanowires. The resulting band structures are compared to those of two-dimensional QWs in the topological regime. Our goal is to understand if we have end states in the nanowire system, similar to the topological edge states present in the two-dimensional QWs.

1.4 Quantum dots

In Papers III and IV we investigate an epitaxially grown QD in an InAs nanowire, that becomes a DQD under the influence of positive side gates. This setup gives a DQD coupled in parallel in the contacted nanowire. We study the spin states in the DQD under an applied magnetic field, a varying interdot coupling and a detuning of the QD one-electron levels. This is done in collaboration with experimentalists. With a few-electron model with one one-electron level in each QD, and a master equation transport model, we can reproduce the experimental data.

1.5 Thesis outline

The thesis is organized in the following manner:

In the first part we introduce the theoretical framework of the models used in Papers I – IV. In Chapters 2 – 4 we introduce the framework of $\mathbf{k} \cdot \mathbf{p}$ theory, some basic theory of topological insulators, and one-electron transport methods, relevant for Papers I and II. In Chapters 5 – 7, relevant for Papers III and IV, we discuss single and double QDs, how their properties are measured and modeled, and we present the master equation formalism used for the QD transport calculations. In the second part of the thesis we discuss the results from Papers I–IV. The thesis is ended with an outlook.

Chapter 2

$\mathbf{k} \cdot \mathbf{p}$ theory

In this chapter, we present the basics of the eight-band $\mathbf{k} \cdot \mathbf{p}$ method, often called the Kane model, used in Papers I and II. We aim at defining concepts and quantities and discuss approximations and limitations that are relevant for this thesis. However, for a complete description of the $\mathbf{k} \cdot \mathbf{p}$ method, the reader is referred to the works in e.g., Refs. [7, 21, 4, 22, 23, 24]. It is worth noting that even though $\mathbf{k} \cdot \mathbf{p}$ theory was developed in the 1950s [22], and has been widely used since, many discrepancies in notation and definitions exist. We do not try to follow any of the existing notations strictly, but instead define all quantities introduced to avoid uncertainties as far as possible.

Originally, the $\mathbf{k} \cdot \mathbf{p}$ method was developed to calculate the band structure of bulk materials [22]. The $\mathbf{k} \cdot \mathbf{p}$ bulk Hamiltonian has to be modified for finite systems and for heterostructures (and for systems with internal or external electric or magnetic fields), since the derivation of the bulk Hamiltonian assumes that the Bloch theorem can be applied. By using the envelope function approximation (EFA) [25, 4], a similar Hamiltonian can be derived describing systems lacking lattice translation symmetry. It can be shown [7] that it is possible to go from the $\mathbf{k} \cdot \mathbf{p}$ Hamiltonian to the EFA Hamiltonian by substituting $\mathbf{k} \rightarrow -i\nabla$, but this substitution introduces an operator ordering problem. The derivations for the $\mathbf{k} \cdot \mathbf{p}$ and the EFA Hamiltonians are very similar, but will both be presented in this thesis for completeness. This chapter is organized as follows: We first present the $\mathbf{k} \cdot \mathbf{p}$ equation, valid for bulk. In the following section we restrict ourselves to an eight-band model, the Kane model, for zincblende. In Section 2.3 the EFA is introduced, used to model finite systems and heterostructures. In the last sections we discuss how we solve the $\mathbf{k} \cdot \mathbf{p}$ equations to obtain the band structures and wave functions.

2.1 The $\mathbf{k}\cdot\mathbf{p}$ equation

We attempt to make a hand-waving derivation of the $\mathbf{k}\cdot\mathbf{p}$ equation valid for bulk. A similar equation for a finite system and/or a heterostructure can be found in Ref. [7]. We start from the (one-electron) Schrödinger equation (SE) $H\psi_{n\mathbf{k}}(\mathbf{r}) = E_n(\mathbf{k})\psi_{n\mathbf{k}}(\mathbf{r})$ for the Bloch spinors $\psi_{n\mathbf{k}}(\mathbf{r}) = \mathrm{e}^{i\mathbf{k}\cdot\mathbf{r}}u_{n\mathbf{k}}(\mathbf{r}) = \mathrm{e}^{i\mathbf{k}\cdot\mathbf{r}}\langle\mathbf{r}\,|n\mathbf{k}\rangle$, and the Hamiltonian

$$H = \frac{p^2}{2m_0} + V_0(\mathbf{r}) + \frac{\hbar}{4m_0^2c^2}\mathbf{p}\cdot\sigma\times(\nabla V_0(\mathbf{r})), \tag{2.1}$$

where n is the band index and $V_0(\mathbf{r})$ is the lattice periodic crystal potential. The last term accounts for SOC effects. The only included SOC here is of atomic origin and stems from the Pauli SOC term. This term is found from a non-relativistic expansion of the Dirac equation [7]. Operating with p^2 on the plane-wave part of the wave function, the SE reads

$$\left[\frac{p^2}{2m_0} + V_0 + \frac{\hbar^2k^2}{2m_0} + \frac{\hbar}{m_0}\mathbf{k}\cdot\pi + \frac{\hbar}{4m_0^2c^2}\mathbf{p}\cdot\sigma\times(\nabla V_0)\right]|n\mathbf{k}\rangle = E_n(\mathbf{k})\,|n\mathbf{k}\rangle \tag{2.2}$$

with $\pi \equiv \mathbf{p} + \frac{\hbar}{4m_0c^2}\sigma\times(\nabla V_0)$. If we insert π into the SE in Eq. 2.2 we find that one of the terms is $\frac{\hbar}{m_0}\mathbf{k}\cdot\mathbf{p}$. This is the term $\mathbf{k}\cdot\mathbf{p}$ theory is named from. However, note that this term is *not* arising from the SOC. We will use the approximation $\pi = \mathbf{p}$, neglecting the $\mathbf{k}$-dependent part of the SOC interaction since this term is small compared to the term [21, 7]

$$H_{SO} = \frac{\hbar}{4m_0^2c^2}\mathbf{p}\cdot\sigma\times(\nabla V_0). \tag{2.3}$$

The index n is a common index for orbital motion and spin, necessary to use when taking SOC into account, since spin is not a good quantum number by itself anymore. This is also the band classification arising from the double group irreducible representations [7]. However, the states are still degenerate Kramers pairs since time-reversal symmetry is not broken. The eigenfunctions of the Hamiltonian in Eq. 2.1 *without* the SOC term, $\{|\nu\mathbf{k}_0\rangle\}$, are a complete orthonormal basis for the SE for any choice of $\mathbf{k}_0$, so that we can expand $|n\mathbf{k}\rangle$ in terms of these (here we make the choice $\mathbf{k}_0 = 0$, since this is where we have our direct band gap in our special case, but any other choice is possible):

$$|n\mathbf{k}\rangle = \sum_{\nu'\sigma'} c_{n\nu'\sigma'}(\mathbf{k})\,|\nu'\sigma'\rangle \tag{2.4}$$

with $|\nu'\sigma'\rangle = |\nu'0\rangle\otimes|\sigma'\rangle$. The reason that we choose to expand in this basis is that we will treat the SOC as a perturbation [22, 4, 23, 7]. The remote band coupling from H_{SO} (and H'_{SO}) is not included in the Kane Hamiltonian.

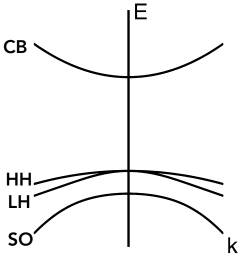

Figure 2.1: The four doubly degenerate bands (eight bands in total) included in the Kane model: conduction band (CB), heavy hole (HH), light hole (LH) and split-off (SO) band.

Now we multiply the SE (Eq. 2.2) from the left by $\langle \nu\sigma|$ and use the eigenvalue equation for $|\nu\sigma\rangle$ to obtain

$$\begin{aligned}\sum_{\nu'\sigma'}\left\{\left[E_{\nu'}(0)+\frac{\hbar^2k^2}{2m_0}\right]\delta_{\nu\nu'}\delta_{\sigma\sigma'}+\frac{\hbar}{m_0}\mathbf{k}\cdot\mathbf{P}_{\nu\nu',\sigma\sigma'}+\Delta_{\nu\nu',\sigma\sigma'}\right\}c_{n\nu'\sigma'}(\mathbf{k})\\ =E_n(\mathbf{k})c_{n\nu'\sigma'}(\mathbf{k})\end{aligned} \tag{2.5}$$

where [7]

$$\mathbf{P}_{\nu\nu',\sigma\sigma'}=\langle\nu\sigma|\,\pi\,|\nu'\sigma'\rangle, \tag{2.6}$$

and

$$\Delta_{\nu\nu',\sigma\sigma'}=\frac{\hbar}{4m_0^2c^2}\langle\nu\sigma|\,[\mathbf{p}\cdot\sigma\times(\nabla V_0)]\,|\nu'\sigma'\rangle. \tag{2.7}$$

The constant SOC elements Δ cause splitting of the otherwise degenerate VB states at $\mathbf{k}=0$, into a so-called split-off band.

2.2 The Kane model

The Hamiltonian presented above is infinite-dimensional, but in practice we are mostly interested in a finite number of bands, N, near the band gap. In the Kane model we take $N=8$ bands into account explicitly: the conduction band, (CB), and three valence bands, the heavy hole (HH), light hole (LH), and the split-off band (SO), all two-fold Kramers degenerate. These bands can be seen in Fig. 2.1. The $\mathbf{k}\cdot\mathbf{p}$ and the SOC interactions are taken into account for these bands explicitly, but remote bands are treated using Löwdin perturbation theory [4, 26], so that our SE becomes an eigenvalue problem of dimension N.

Here, the 8×8 $\mathbf{k}\cdot\mathbf{p}$ Kane matrices are presented, together with a discussion of the parameters used in our model. The matrix representations presented in this section are valid for zincblende, but not for wurtzite crystal structures. The corresponding Kane Hamiltonian for wurtzite is similar to that for zincblende, but has 19 parameters instead of ten [21]. For a discussion on wurtzite modeling using $\mathbf{k} \cdot \mathbf{p}$ theory, see e.g., Refs. [7, 21, 4].

We will present the Kane Hamiltonian for bulk in a the Bloch basis

$$\{|S\uparrow\rangle, |S\downarrow\rangle, |X\uparrow\rangle, |Y\uparrow\rangle, |Z\uparrow\rangle, |X\downarrow\rangle, |Y\downarrow\rangle, |Z\downarrow\rangle\}, \tag{2.8}$$

with one s-like CB and three p-like VBs states, where $|X\uparrow\rangle = |X\rangle\,|\uparrow\rangle$ etc. This basis can be related to a pure band basis

$$\{|S\uparrow\rangle, |S\downarrow\rangle, |HH\uparrow\rangle, |LH\uparrow\rangle, |LH\downarrow\rangle, |HH\downarrow\rangle, |SO\uparrow\rangle, |SO\downarrow\rangle\} \tag{2.9}$$

by

$$\begin{aligned}
|HH\uparrow\rangle &= -\frac{1}{\sqrt{2}}\left(|X\rangle + i\,|Y\rangle\right)|\uparrow\rangle \\
|LH\uparrow\rangle &= \frac{1}{\sqrt{6}}\left[-\left(|X\rangle + i\,|Y\rangle\,|\downarrow\rangle\right) + 2\,|Z\rangle\,|\uparrow\rangle\right] \\
|LH\downarrow\rangle &= \frac{1}{\sqrt{6}}\left[\left(|X\rangle - i\,|Y\rangle\,|\uparrow\rangle\right) + 2\,|Z\rangle\,|\downarrow\rangle\right] \\
|HH\downarrow\rangle &= \frac{1}{\sqrt{2}}\left(|X\rangle - i\,|Y\rangle\right)|\downarrow\rangle \\
|SO\uparrow\rangle &= -\frac{1}{\sqrt{3}}\left[\left(|X\rangle + i\,|Y\rangle\,|\downarrow\rangle\right) + |Z\rangle\,|\uparrow\rangle\right] \\
|SO\downarrow\rangle &= -\frac{1}{\sqrt{3}}\left[\left(|X\rangle - i\,|Y\rangle\,|\uparrow\rangle\right) - |Z\rangle\,|\downarrow\rangle\right].
\end{aligned} \tag{2.10}$$

The reason for using the Bloch basis instead of the band basis, is that the eight-band Hamiltonian then takes a simpler and more elegant form.

The Kane Hamiltonian in the Bloch basis (Eq. 2.8) is given by [4, 24, 21]

$$H_8 = H_0 + H_{SO} \tag{2.11}$$

where

$$H_0 = \left(\begin{array}{cc|c|c}
H_{cc} & 0 & H_{cv} & 0 \\
0 & H_{cc} & 0 & H_{cv} \\
\hline
H_{vc} & 0 & H_{vv} & 0 \\
\hline
0 & H_{vc} & 0 & H_{vv}
\end{array}\right) \tag{2.12}$$

and

$$H_{SO} = \frac{1}{3}\Delta_{SO}\begin{pmatrix} 0 & 0 & 0 & 0 & 0 & 0 & 0 & 0 \\ 0 & 0 & 0 & 0 & 0 & 0 & 0 & 0 \\ 0 & 0 & 0 & -i & 0 & 0 & 0 & 1 \\ 0 & 0 & i & 0 & 0 & 0 & 0 & -i \\ 0 & 0 & 0 & 0 & 0 & -1 & i & 0 \\ 0 & 0 & 0 & 0 & -1 & 0 & i & 0 \\ 0 & 0 & 0 & 0 & -i & -i & 0 & 0 \\ 0 & 0 & 1 & i & 0 & 0 & 0 & 0 \end{pmatrix}. \tag{2.13}$$

The submatrices of H are given by

$$H_{cc} = E_c + k_x A k_x + k_y A k_y + k_z A k_z, \tag{2.14}$$

$$H_{cv} = \begin{pmatrix} k_y B k_z + iP k_x & k_z B k_x + iP k_y & k_x B k_y + iP k_z \end{pmatrix}, \tag{2.15}$$

$$H_{vc} = H_{cv}^{\dagger}, \tag{2.16}$$

where † s is used for the Hermitian conjugate, and

$$\begin{aligned} H_{vv} = {} & \left(E_v' + \frac{\hbar^2}{2m_0}\mathbf{k}^2\right)\begin{pmatrix} 1 & 0 & 0 \\ 0 & 1 & 0 \\ 0 & 0 & 1 \end{pmatrix} \\ & + \begin{pmatrix} k_i M k_i + k_x(L-M)k_x & k_x N^+ k_y + k_y N^- k_x & k_x N^+ k_z + k_z N^- k_x \\ k_y N^+ k_x + k_x N^- k_y & k_i M k_i + k_y(L-M)k_y & k_y N^+ k_z + k_z N^- k_y \\ k_z N^+ k_x + k_x N^- k_z & k_z N^+ k_y + k_y N^- k_z & k_i M k_i + k_z(L-M)k_z \end{pmatrix} \end{aligned} \tag{2.17}$$

where E_c and $E_v = E_v' + \Delta_{SO}/3$ are the CB and VB edge energies, and we have introduced the notation $k_i M k_i = k_x M k_x + k_y M k_y + k_z M k_z$. The parameter P is related to the Kane energy E_P through $P = \sqrt{\frac{\hbar^2}{2m_0}E_P}$.

The coupling to remote bands is accounted for through the second-order-in-k matrix elements in H_{cv}, H_{vc} and H_{vv}. The parameter A is given by $A = \frac{\hbar^2}{2m_0}S$ where $S = \frac{m_0}{m_{CB}^*} - \frac{2E_P}{3E_g} - \frac{E_P}{3(E_g+\Delta_{SO})} = 1 + 2F$ [21]. The parameter B originates from the $\mathbf{k}\cdot\mathbf{p}$ -term in Eq. 2.2 and accounts for bulk inversion asymmetry in zincblende, which will be discussed in Section 2.5. It is often set to zero [27, 28, 24, 29, 30, 31], approximating the zincblende structure to be inversion symmetric (i.e., a diamond structure). We use this approximation and assume that $B = 0$ throughout this thesis.

The parameters L, M, N^+ and N^- are calculated from the Luttinger parameters γ_1, γ_2 and γ_3 as [31, 21]

$$L = -\frac{\hbar^2}{2m_0}(\gamma_1 + 4\gamma_2) + \frac{P^2}{E_g} \tag{2.18}$$

$$M = -\frac{\hbar^2}{2m_0}(\gamma_1 - 2\gamma_2) \tag{2.19}$$

$$N^- = M - \frac{\hbar^2}{2m_0} \tag{2.20}$$

$$N^+ = -6\frac{\hbar^2}{2m_0}\gamma_3 + \frac{P^2}{E_g} - N^-. \tag{2.21}$$

In bulk we can use $N^+ = N^- = N/2$, where $N = N^+ + N^-$, since N^+ and N^- commute with all k_i in Eq. 2.18 in that case.

To calculate for a structure grown in another crystallographic direction than [100], [010] or [001], usually identified with the x, y, and z coordinates, the coordinate system needs to be rotated. This rotation process is discussed in Appendix A.

2.3 The envelope function approximation

For systems lacking lattice translation symmetry, such as low-dimensional structures, heterostructures, strained systems, and systems with applied fields, the $\mathbf{k} \cdot \mathbf{p}$ equation is not valid. Instead we derive an equation in the EFA. It turns out that the EFA Hamiltonian is very similar to the $\mathbf{k} \cdot \mathbf{p}$ Hamiltonian in the end, but it is important to state that they are not completely identical. The Hamiltonian we start from in this case is similar to the $\mathbf{k} \cdot \mathbf{p}$ Hamiltonian, but with an extra potential term $V(\mathbf{r})$

$$H = \frac{(-i\hbar\nabla)^2}{2m_0} + V_0(\mathbf{r}) + \frac{\hbar}{4m_0^2c^2}(-i\hbar\nabla) \cdot \sigma \times (\nabla V_0) + V(\mathbf{r}). \tag{2.22}$$

Here we have assumed that no external magnetic or electric fields are present. Note that there is no $\mathbf{k} \cdot \mathbf{p}$ term in this Hamiltonian, and that we cannot use the Bloch theorem as we did in Section 2.1, since lattice translation symmetry is broken. We wish to solve the SE $H\Psi(\mathbf{r}) = E\Psi(\mathbf{r})$ for this Hamiltonian. We expand the wave function $\Psi(\mathbf{r})$ in Bloch functions at $\mathbf{k}_0 = 0$,

$$\Psi(\mathbf{r}) = \sum_{\nu'\sigma'} \psi_{\nu'\sigma'}(\mathbf{r}) u_{\nu'0}(\mathbf{r}) \left|\sigma'\right\rangle. \tag{2.23}$$

The ψ are envelope functions, the u oscillating Bloch functions and $|\sigma\rangle$ are the spin eigenstates. We insert the expansion into the SE, multiply from he left by $\langle\sigma|\, u^*_{\nu'0}(\mathbf{r})$ and integrate over one unit cell. To be able to carry out the integration we assume that $V(\mathbf{r})$ and

$\psi_{\nu'\sigma'}(\mathbf{r})$ are slowly varying and can be taken outside the integral. Using this approximation we get

$$\sum_{\nu'\sigma'} \left[\left(E_{\nu'}(0) + \frac{(-i\hbar\nabla)^2}{2m_0} + V(\mathbf{r}) \right) \delta_{\nu\nu'}\delta_{\sigma\sigma'} + \right. \\ \left. \frac{1}{m_0}(-i\hbar\nabla) \cdot \mathbf{P}_{\nu\nu',\sigma\sigma'} + \Delta_{\nu\nu',\sigma\sigma'} \right] \psi_{\nu'\sigma'}(\mathbf{r}) = E\psi_{\nu'\sigma'}(\mathbf{r}). \tag{2.24}$$

The EFA SE is now a system of coupled differential equations, with its eigenfunctions being multicomponent spinors. Using Löwdin perturbation theory we can scale down from the case with infinitely many bands, to an N-dimensional system that only includes N bands explicitly, as we did in Section 2.2 for the Kane model with $N = 8$.

In most practical implementations, the matrix elements $\mathbf{P}$ and Δ, together with the material parameters, are taken from experiments or *ab initio* calculations for bulk systems. Additionally, we have to input the bulk band edge energies to our calculations. For a heterostructure, this is done by assuming that the parameters are constant in each of the materials separately, and that they vary step-like at the material interface [4, 24]. Furthermore, at the material interface the EFA assumption that the potential varies slowly is not valid. An implication of this is that the results of the $\mathbf{k} \cdot \mathbf{p}$ calculations will not be reliable very close (some Å) to the material interfaces [4].

2.3.1 Operator ordering in the Kane Hamiltonian

It is often argued that we can go from the $\mathbf{k} \cdot \mathbf{p}$ Hamiltonian to the EFA Hamiltonian by substituting $\hbar\mathbf{k} = \mathbf{p} \rightarrow -i\hbar\nabla$ and adding the external potential $V(\mathbf{r})$ (if $V(\mathbf{r}) = 0$, the $\mathbf{k}$ here is the wave vector). This is in some sense true, but introduces problems with operator ordering. For a system with more than one material, the operators $\mathbf{k} \rightarrow -i\nabla$ do not commute with the space-dependent $\mathbf{k} \cdot \mathbf{p}$ -parameters. In the case of a finite magnetic field, the components of $\mathbf{k}$ do not even commute with each other. However, apart from the operator ordering, the 8-band EFA Hamiltonian in matrix form will look just like the Kane Hamiltonian in Eq. 2.11 if we substitute $\nabla \rightarrow i\mathbf{k}$. The problem will then turn into a system of eight coupled partial differential equations.

Some authors [4, 24] use a symmetrization scheme to go from the $\mathbf{k} \cdot \mathbf{p}$ to the EFA Hamiltonian, and make the bulk Hamiltonian in Eq. 2.11 valid for a heterostructure by forcing all Hamiltonian matrix elements to be Hermitian, by letting $kQ(r) \rightarrow \frac{1}{2}[kQ(r) + Q(r)k]$ for a material dependent parameter $Q(r)$. However, we prefer to use the EFA formalism where a Hamiltonian for heterostructures is derived taking boundary conditions into account, so that it has the correct operator ordering to begin with. In practice, the only matrix elements that will be different in the two approaches are[1]

1. The elements in H_{vv} involving the N^+ and N^- parameters
2. All elements in H_{cv} and H_{vc}

If we use the approximation $N^+ = N^- = N/2$, the EFA and the symmetrized version will be the same for these elements. In the special case of the InAs/GaSb and GaSb/InAs core-shell nanowires, using this approximation for N_+ and N_- yields (almost) the same result as using the expressions for N_+ and N_- given by Eqs. 2.20 and 2.21, hence these elements will not be further discussed here.

For the elements in H_{cv} and H_{vc}, we assume that $B = 0$, as mentioned above. What is left to resolve is then the ordering of the P–operator and k_i, $i = x, y, z$. According to Foreman all elements in H_{cv} in the Hamiltonian involving P should be proportional to Pk_i, so that

$$H_{cv} = \begin{pmatrix} iPk_x & iPk_y & iPk_z \end{pmatrix} \tag{2.25}$$

and $H_{vc} = H_{cv}^\dagger$ [31]. This leads to a Hermitian Hamiltonian for a general heterostructure. For $A = 0$ (an approximation often used) this is the only operator ordering that gives a Hamiltonian that is mathematically consistent, in the sense that for all other operator orderings there will be boundary conditions that cannot be satisfied in the limit $A \to 0$ [31].

It is common to see a version of the Kane Hamiltonian identical with the one presented here, but with

$$H_{vc} = \begin{pmatrix} -ik_xP & -ik_yP & -ik_zP \end{pmatrix}^T \tag{2.26}$$

This leads to a non-Hermitian Hamiltonian if not $k = k^\dagger$, which is in general not true for $\mathbf{k} \to -i\nabla$. If one replaces $k \to k^\dagger$ in this version of H_{vc} it holds that $H_{vc} = H_{cv}^\dagger$, so that the full Hamiltonian is Hermitian. In a numerical implementation the best way to set up the Hamiltonian matrix is to set $H_{vc} = H_{cv}^\dagger$ with H_{cv} given by Ref. [31], and it is then not necessary to write down an explicit analytical expression for H_{vc}. In practice, Hermiticity of the total Hamiltonian matrix is often assumed in numerical diagonalization schemes, so that we only need to specify the upper right (or lower left) half of the Hamiltonian.

2.4 Spurious solutions

One of the challenges with the $\mathbf{k} \cdot \mathbf{p}$ method is the existence of spurious solutions. These are solutions which are correct solutions to the $\mathbf{k} \cdot \mathbf{p}$ equation in a mathematical sense, but

---

[1] Matrix elements that are second-order-in-k will be the same in the EFA approach and in the symmetrization scheme.

unphysical [31, 21]. One explanation for this phenomenon is that the $\mathbf{k} \cdot \mathbf{p}$ equations are valid only for small k (or k close to k_0). However, when we employ the EFA, $k \to -i\nabla$, solutions that in bulk would correspond to large k values can give rise to non-physical solutions [32].

2.4.1 Choosing parameters to avoid spurious solutions

All parameters in the Hamiltonian are in general functions of $\mathbf{r}$, and when using the EFA, the crystal momentum $\mathbf{k}$ becomes an operator, so that it does not commute with the space dependent parameters. The spurious solutions arise due to a term proportional to k^4 in the secular equation [31]. It was suggested by Foreman [31] to set $A = 0$ to avoid spurious solutions, since the k^4 term then becomes zero. The term A scales the band bending of the CB, and to maintain the correct effective mass of the CB he showed that the value of E_P should then be adjusted according to

$$E_P = \left(\frac{m_0}{m_c}\right) \frac{E_g(E_g + \Delta_{SO})}{E_g + \frac{2}{3}\Delta_{SO}}. \tag{2.27}$$

The Kane energy E_P enters the Kane Hamiltonian through the optical parameter $P = \sqrt{\frac{\hbar^2}{2m_0}E_P}$, and scales the linear-in-k coupling between the CBs and the VBs. Another alternative to get rid of the k^4 term in the secular equation is to neglect all couplings to remote bands [31]. Doing this would require the CB and the VB effective masses to be determined by one parameter only. Hence, it is a better alternative to set only $A = 0$ and rescale E_P accordingly. However, another alternative used by some [21] is to neglect the effect of the remote bands on the CB.[2] This approach is implemented by setting $A = \frac{\hbar^2}{2m_0}$ (sometimes referred to as $A = 1$ using natural units) and adjusting E_P in a similar fashion as before:

$$E_P = \left(\frac{m_0}{m_c} - 1\right) \frac{E_g(E_g + \Delta_{SO})}{E_g + \frac{2}{3}\Delta_{SO}}. \tag{2.28}$$

It is common practice to set $A = \frac{\hbar^2}{2m_0}$, even if E_P is not accordingly adjusted.

It may seem odd that we can just change the value of our parameters and that there is no consensus on how this should be done. However, taking into account that spurious solutions are unphysical results with errors that grow with problem size (e.g., the number of basis functions used), adjusting the parameters is not only something you could do, but in fact something that should be done in many cases.

In Chapter 9 we discuss an additional method to avoid spurious solutions. In addition to the methods mentioned above, we have found that adding insulator barriers to a semiconductor heterostructure can remove spurious solutions. We believe that the reason for this

---

[2] This can be a rather controversial subject.

behavior is that we then get rid of the abrupt material interface (between the semiconductor and the vacuum), where the wave function must tend to zero very quickly, which can render oscillations and overshooting.

2.5 Inversion asymmetry

The lack of inversion symmetry in zincblende heterostructures causes spin-degenerate bands to split.These effects can be divided into bulk inversion asymmetry (BIA) terms (from crystal structure) and structural inversion asymmetry (SIA) terms (from finite crystal systems that breaks inversion asymmetry due to their nanoscale structure, i.e., InAs/GaSb QWs).

The parameter B in Eq. 2.11 (Kane Hamiltonian) accounts for bulk inversion asymmetry (BIA) in zincblende structures. All zincblende structures (except diamond structure) lack a center of inversion, so that B should be non-zero [7]. This term causes spin-splitting in second order in k, and mixes the CB and VB [7].

In addition to BIA, structural inversion asymmetry (SIA) can split spin degenerate bands, in structures that breaks inversion symmetry. The SIA is to a large extent taken into account implicitly in the Kane model [21], where structure is accounted for when solving the equations. However, in effective models based on $\mathbf{k} \cdot \mathbf{p}$ theory (such as the BHZ model, introduced in Chapter 3) the SIA terms must be introduced explicitly. The SIA terms split the CB in linear order in k, but higher order terms mix both CB and VB with each other and within the bands [7]. The linear-in-k coupling is often referred to as the Rashba term, but sometimes SIA splitting of any order is called Rashba splitting. Additional spin splitting SIA terms are needed in the presence of electric field [7], but we do not consider such effects (similar to Refs. [33, 34], but in contrast to Ref. [11] which uses a self-consistent Poisson solver together with the $\mathbf{k} \cdot \mathbf{p}$ model, and Ref. [10], imposing a linear voltage drop).

For single material nanowire systems, the BIA spin split affects only $k \neq 0$ and is not contributing in the high-symmetry directions [001] and [111] [21]. However, for heterostructures, B can cause spin splitting in all directions of $\mathbf{k}$ [21]. We assume that B is small and set it to zero, following many other authors, see for example Refs. [27, 28, 24, 29, 30, 35, 31, 10, 34, 36]. In Ref. [27] BIA is not taken into account since it is much smaller in the QWs than the SIA.

It is important to note that even though BIA and SIA cause splitting of spin-degenerate states, they cannot split Kramers pairs. Instead they split the spatial inversion symmetry pairs $\{E_\uparrow(\mathbf{k}), E_\uparrow(-\mathbf{k})\}$. The Kramers pairs $\{E_\uparrow(\mathbf{k}), E_\downarrow(-\mathbf{k})\}$ cannot be split as long as the system obeys time reversal symmetry. For systems that are both space inversion and time reversal invariant, we will then have doubly degenerate states for all $\mathbf{k}$, since then $E_\uparrow(\mathbf{k}) = E_\downarrow(\mathbf{k})$ must hold for all states.

2.6 Basis expansion of envelope functions

We solve the eight partial differential equations of the EFA SE by inserting a complete basis function expansion in the directions where the structure is finite. When calculating band structures and wave functions for the QW in Paper II, we take only the z direction to be finite. However, for our cylindrical systems (the nanowires) we assume that we have translation invariance in the z-direction, and take our system to be finite in the x- and y-directions.

The basis function expansion is truncated to yield a finite eigenvalue problem. We write our wave function as an expansion

$$\psi(\mathbf{r}) = \sum_{mnl} F_{n,l}(k_i)\, U_{m,n,l}(\mathbf{r}) \tag{2.29}$$

where $F_{n,l}(k_i)$ is a *smooth, continuos*, function over the existing wave vectors k_i (in the directions where translational symmetry applies) and $U_{m,n,l}(\mathbf{r})$ is a *complete set of orthogonal basis functions* over the whole structure. The indices $\{m, n, l\}$ label the basis functions in the finite directions of the problem. This means that for a nanowire with confinement in two directions, only two indices are needed, and for a QW that is confined in one direction, only one index is needed,

In principle any complete basis could be chosen to expand in. However, to be able to use as few basis functions as possible one needs to choose a basis with functions that relatively well describes the wave functions for the bands close to the band gap. Which type of functions one should expand in hence depends on the spatial geometry of the problem. If a basis that is not well-suited is used in the implementation, it can in practice be impossible to converge the calculations.

For the QWs we use a plane wave basis expansion. For the cylindrical nanowires considered in this thesis a basis of Bessel functions (i.e., the solutions to the SE in a cylindrical infinite potential well)

$$U_{n,l}(\mathbf{r}) = J_n(\alpha_{nl}\frac{r}{R})e^{in\theta}e^{ik_z z}, \tag{2.30}$$

is used. When we consider core-shell nanowires with an insulator core, we model them to be hollow in the middle to avoid large computational costs, using the basis expansion

$$U_{n,l}(\mathbf{r}) = \frac{2}{\sqrt{\pi r}} \sin\left(\frac{R-r}{R_C-R} l\pi\right) e^{in\theta}e^{ik_z z}. \tag{2.31}$$

This is a complete basis and is chosen since it is an approximation of the solution to the Bessel equation for a hollow cylinder for large r [37]. Furthermore, it is easily adaptable to the Dirichlet boundary conditions that the wave function should vanish both at the inner and the outer border of the system.

2.7 Calculating the wave functions using the $\mathbf{k} \cdot \mathbf{p}$ method

Until this point, the focus has been on the energy dispersion obtained from solving the eigenvalue problem of the $\mathbf{k} \cdot \mathbf{p}$ Hamiltonian. Since we are also interested in the wave functions, some theory and some notation is presented here. This is done for the cylindrical systems. Following Ref. [24], we write the total wave function in the Kane model as

$$\Psi(\mathbf{r}) = \sum_{n=1}^{8} U_n(\mathbf{r})\psi_n(\mathbf{r}), \tag{2.32}$$

with $U_n(\mathbf{r})$ as Bloch functions and $\psi_n(\mathbf{r})$ envelope functions (where we take $\mathbf{r} \to r, \theta$ and multiply with $e^{ik_z z}$ for a cylindrical structure such as a nanowire, assumed to be grown in the z-direction). When the SE is rewritten as the $\mathbf{k} \cdot \mathbf{p}$ equation, the Bloch functions cancel, so that our eigenvalue problem is just

$$H\psi(\mathbf{r}) = E\psi(\mathbf{r}), \tag{2.33}$$

where H is the Kane Hamiltonian given by Eq. 2.11 and

$$\psi(\mathbf{r}) = [\psi_1(\mathbf{r}) \quad \psi_2(\mathbf{r}) \quad \dots \quad \psi_8(\mathbf{r})]^T. \tag{2.34}$$

To solve these coupled differential equations we expand the envelope functions in radial and angular basis functions, $R_{j,l}(r)$ and $\Theta_{j,l}(\theta)$, respectively, as

$$\psi_n(\mathbf{r}) = \sum_{j=-J,l=1}^{j=J,l=L} F_n(j,l) N_{j,l} R_{j,l}(r)\Theta_{j,l}(\theta), \tag{2.35}$$

using the j- and l-dependent normalization constant $N_{j,l}$. We are here only considering the special case of a cylindrical structure, infinite in z, the general expansion can found in Ref. [24]. Solving the equations numerically will give us $F_n(j,l)$ as the eigenvectors. To obtain the $X = 8 \cdot ((2 \cdot J + 1) + L)$ wave functions we must reassemble them from the eigenvectors obtained from diagonalizing the Hamiltonian. For the wave function we find

$$\Psi(r,\theta) = \sum_{n=1}^{8} \psi_n = \sum_{n=1}^{8} \sum_{j,l} F_n(j,l) N_{j,l} R_{j,l}(r)\Theta_{j,l}(\theta), \tag{2.36}$$

and correspondingly for the probability density ρ we find

$$\rho(r,\theta) = |\Psi(r,\theta)|^2 = \sum_{n=1}^{8} |\psi_n|^2 = \sum_{n=1}^{8} |\sum_{j,l} F_n(j,l) N_{j,l} R_{j,l}(r)\Theta_{j,l}(\theta)|^2, \tag{2.37}$$

where we have used that $|U_n(\mathbf{r})|^2 = 1$.

Chapter 3

Topological insulators

In the last fifteen years or so, topological materials have gained a lot of attention. It is a broad and theoretically vast and deep subject, that has attracted the interest of many physicists, and we do not attempt to cover the whole subject here. In this chapter we focus on quantum spin Hall (QSH) insulators, but it should be mentioned that other topological systems exist, including e.g., the fractional, integer and anomalous Hall effects and topological superconductors.

One of the most promising applications for topological materials lies within quantum information processing. For example, in topological superconductors topologically protected states with non-abelian exchange statistics are one suggestion for realizing qubits [38].

3.1 Topological materials

Topological phases are non-local, meaning that they cannot be described by a local order parameter [41]. Instead, the topological materials can be classified according to the fundamental symmetries of time-reversal, particle-hole and chirality, together with their dimensionality [39], see Table 3.1. This classification leads to ten different so-called symmetry classes, including all possible combinations of these three symmetries. For every class and every specific dimensionality in the symmetry table there exists (or does not exist for a topologically trivial system) a topological invariant n. The topological invariant is an integer, $n \in \mathbb{Z}$ or $n \in \mathbb{Z}_2$, that can only change if the system undergoes a topological phase transition. This is where the name "topological" in physics comes from, because it has similarities with topological properties in mathematics. Topology in mathematics describes objects that can be categorized by an integer alone, such as the number of holes (one) in a donut. Here, we can label a physical system with an integer, that tells us in which

Table 3.1: The Altland-Zirnbauer periodic table of topological materials. Ten symmetry classes are defined by their behavior under time-reversal symmetry (eigenvalue $\mathcal{T}$), particle hole-symmetry (eigenvalue $\mathcal{C}$) and chiral symmetry (eigenvalue $\mathcal{P} = \mathcal{T}\mathcal{C}$) in dimensions d. The table is periodic for $d \to d + 8$. The symmetry classes marked with ‡ requires fine tuning of the Hamiltonian, and is thus hard to realize in a real physical system. Adapted from references [39] and [40].

Symmetry class	$\mathcal{T}^2$	$\mathcal{C}^2$	$\mathcal{P}$	$d = 1$	2	3	4	5	6	7	8
A	0	0	0	0	$\mathbb{Z}$	0	$\mathbb{Z}$	0	$\mathbb{Z}$	0	$\mathbb{Z}$
AIII‡	0	0	1	$\mathbb{Z}$	0	$\mathbb{Z}$	0	$\mathbb{Z}$	0	$\mathbb{Z}$	0
AI	1	0	0	0	0	0	$\mathbb{Z}$	0	$\mathbb{Z}_2$	$\mathbb{Z}_2$	$\mathbb{Z}$
BDI‡	1	1	1	$\mathbb{Z}$	0	0	0	$\mathbb{Z}$	0	$\mathbb{Z}_2$	$\mathbb{Z}_2$
D	0	1	0	$\mathbb{Z}_2$	$\mathbb{Z}$	0	0	0	$\mathbb{Z}$	0	$\mathbb{Z}_2$
DIII	-1	1	1	$\mathbb{Z}_2$	$\mathbb{Z}_2$	$\mathbb{Z}$	0	0	0	$\mathbb{Z}$	0
AII	-1	0	0	0	$\mathbb{Z}_2$	$\mathbb{Z}_2$	$\mathbb{Z}$	0	0	0	$\mathbb{Z}$
CII‡	-1	-1	1	$\mathbb{Z}$	0	$\mathbb{Z}_2$	$\mathbb{Z}_2$	$\mathbb{Z}$	0	0	0
C	0	-1	0	0	$\mathbb{Z}$	0	$\mathbb{Z}_2$	$\mathbb{Z}_2$	$\mathbb{Z}$	0	0
CI	1	-1	1	0	0	$\mathbb{Z}$	0	$\mathbb{Z}_2$	$\mathbb{Z}_2$	$\mathbb{Z}$	0

topological phase we are in.

For certain topological phases there exist more or less exotic properties which are interesting to study for many reasons, because (among other things) they are topologically protected. This means that these properties cannot be affected by perturbations, but are instead robust and can only be destroyed if the system undergoes a topological phase transition (or if one of the three classifying symmetries are changed - then the system can change topological class). For the topological insulators with topological invariant $n \in \mathbb{Z}_2$, the system can be either in a topologically trivial phase ($n = 0$), or in a topologically non-trivial phase ($n = 1$) . In the topologically trivial phase the system behaves as an ordinary insulator, while in the topologically non-trivial phase topologically protected states at the end, edges or surfaces are present.

3.1.1 Topological insulators with time-reversal symmetry

The QSH insulators belong to symmetry class AII in Table 3.1 [40], meaning that they obey time-reversal symmetry (with a time-reversal operator $\mathcal{T}$ that squares to $\mathcal{T}^2 = -1$), but not particle-hole, or chiral symmetry. A two-dimensional QSH insulator is an insulator (or semiconductor) with additional spin-momentum-locked electronic states at its surface, living inside the insulating bulk gap. These QSH edge states propagate without backscattering, as long as no time-reversal breaking mechanism, such as magnetic impurities, are present. There are also three-dimensional TIs in the AII symmetry class.

The bulk gap of a topological insulator in the topological phase is special, since it has inverted bands. Band inversion means that some CB-like bands are found below the band gap, while some VB-like bands lie above the gap. We call such an inverted gap a *hybridiza-*

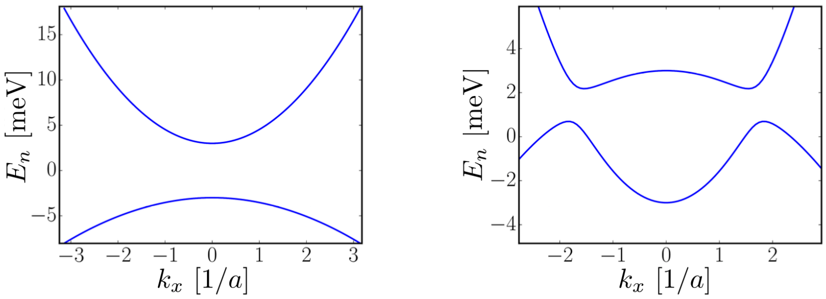

Figure 3.1: Left: A confinement gap for a quantum well in the trivial regime. Right: A hybridization gap, for the same quantum well, but in the topological phase.

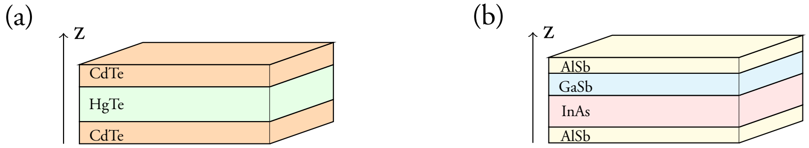

Figure 3.2: The geometry of the (a) HgTe/CdTe QW and the (b) InAs/GaSb QW with AlSb barriers. By varying the thickness of the HgTe middle layer in (a), the system can be tuned between a topological regime ($w > w_c$) with inverted bands, and a trivial regime ($w < w_c$) with a normal band gap. Figure (b) adapted from Paper II.

tion gap. In Fig. 3.1 we show such a hybridization gap, together with a normal confinement gap.

In 2006 the authors of Ref. [42] showed that band inversion, via closing of the band gap, can signal a topological phase transition. This implies that, as long as we do not break time-reversal symmetry a topological insulator in the topological phase will stay in that nontrivial phase as long as there is no closure of the bulk gap. This result can be used to greatly simplify the analysis of TIs. We can compute the topological invariant and/or look for edge states of the system in a limit where the complexity of the Hamiltonian has been greatly reduced (e.g., by tuning parameters to zero), knowing that as long as this simplification of the system does not imply any closing of the band gaps, all topological properties will remain intact. Another approach is to introduce an effective low-energy Hamiltonian to study the states around (and in) the bulk gap. This is done in the BHZ model [42].

3.2 Two-dimensional topological insulators

The two-dimensional TIs were first predicted to exist in graphene [43]. However, graphene TIs have not been realized experimentally, due to the small energy gap in graphene resulting from the material's small SOC [42]. Instead it was QWs made from layered HgTe and CdTe (see Fig. 3.2) that proved to be the first experimentally realizable TI [44]. These materials are made up from heavy atoms, with large SOC, leading to relatively large band gaps (in comparison with graphene). It has been shown [11, 12] that also QWs made from InAs and GaSb are TIs. While the gap size in HgTe/CdTe QWs can be tuned by changing the thickness of HgTe in the QWs, the gap in the InAs/GaSb QWs can in addition be tuned by a gate voltage [45]. This is of course a great advantage for practical purposes.

For a topological phase transition to take place in a TI, it is necessary for the band gap to close and reopen. An effective model (later called the BHZ model) of the bands closest to the band gap in a TI was proposed by Bernevig, Hughes and Zhang in Ref. [42]. This model can be derived from a multi-band $\mathbf{k} \cdot \mathbf{p}$ Hamiltonian [42, 33], or obtained as a low-k approximation to a tight-binding model [42]. It is also possible to find the Hamiltonian using symmetry arguments only. The BHZ Hamiltonian usually takes its parameters from fitting with $\mathbf{k} \cdot \mathbf{p}$ calculations [42, 33, 11]. Using their model,Bernevig, Hughes and Zhang showed that the TI is in the topologically non-trivial phase when the CB and VB are inverted (as long as the system still has an effective bulk band gap) [42]. In the trivial phase the CB lies above the VB. By showing that the gap was not closed when tuning parameters to zero, hence simplifying the model, an analysis of the topological phase could be performed for a simpler system than was modelled originally. In HgTe/CdTe the bulk inversion asymmetry can be taken out of the calculations in this way [42].

One of the reasons that we are so interested in two-dimensional TIs is because they exhibit the QSH effect. The QSH effect is similar to the quantum Hall effect, but requires no external magnetic field. An ordinary quantum Hall system has edge modes propagating in one direction on its edges, so that on a single edge a charge current is present. However, for a QSH insulator, the edge states are spin polarized, so that particles with opposite spin are counterpropagating. This is sometimes referred to as spin-momentum locking or helical edge states. This means that, in contrast to the quantum Hall insulator, a single edge of the QSH insulator carries no net charge current. The edge states are topologically protected, in the sense that as long as time-reversal symmetry is not broken and we persist in the topologically non-trivial phase, the edge states are robust against perturbations. This means that non-magnetic impurities cannot cause backscattering of the edge states. However, when magnetic impurities are present, time-reversal symmetry is broken, and the edge states can be affected [46, 47].

3.2.1 The BHZ model

The BHZ model was originally proposed for HgTe/CdTe QWs, but has also been used for GaSb/InAs QWs, see Fig. 3.2(a)-(b) [11]. We stress the difference between these two systems; in the former the band inversion takes place in the HgTe, while in the latter the electrons and the holes lives in different materials (in InAs and GaSb, respectively) and it is then the full system that is the TI. It includes one CB and one VB, both Kramers degenerate, so that we will have a four band Hamiltonian [42]:

$$H_{BHZ} = \begin{pmatrix} H(k) & 0 \\ 0 & H^*(-k) \end{pmatrix}, \tag{3.1}$$

with

$$H(k) = \varepsilon(k)\sigma_0 + \sum_{i=x,y,z} d_i(k)\sigma_i, \tag{3.2}$$

$$\mathbf{d} = \begin{pmatrix} Ak_x \\ -Ak_y \\ M - B(k_x^2 + k_y^2) \end{pmatrix}, \tag{3.3}$$

and

$$\varepsilon(k) = C - D(k_x^2 + k_y^2). \tag{3.4}$$

In Paper II, when we model InAs/GaSb QWs, we also add a SIA term to the Hamiltonian in Eq. 3.1. We include SIA terms up to third order in k:

$$H_{SIA} = \begin{pmatrix} 0 & H_{SIA}^{2\times 2} \\ (H_{SIA}^{2\times 2})^\dagger & 0 \end{pmatrix}, \tag{3.5}$$

where

$$H_{SIA}^{2\times 2} = \begin{pmatrix} -iR_0 k_- & -S_0 k_-^2 \\ S_0 k_-^2 & iT_0 k_-^3 \end{pmatrix}, \tag{3.6}$$

and we have introduced $k_\pm = k_x \pm ik_y$.

It is possible to diagonalize the full BHZ Hamiltonian analytically. The mass parameter M changes sign at a critical width $w = w_c$ of HgTe, where the band gap closes, or in the more general case, when a topological phase transition takes place. However, while we can use this model to find the bulk properties for a two-dimensional system, we need to modify it for a system finite in x or y, so that we can study the edges and the possible edge states.

The presence of topological edge states can in practice be deduced from two different approaches. The first way consists of employing a model of a finite system, i.e., with edges, and study the energy spectrum together with the wave functions. The edge state reside inside the bulk band gap, where each of the edge state bands has a different velocity direction and are *not* Kramers degenerate. However, Kramers theorem is still not violated, since $E_+(k) = E_-(-k)$ holds for the Kramers partners E_+ and E_-. Possible edge states must be tested for robustness to exclude the possibility of a non-topological origin. This method is employed in Paper II. The second approach is using the so-called bulk boundary correspondence, where the presence of topological edge modes is deduced from the topological invariant $\mathbb{Z}_2$ calculated from the corresponding bulk system [48]. The $\mathbb{Z}_2$ invariant ν is given by

$$\nu = C \mod 2, \tag{3.7}$$

where C is the Chern number. The Chern number can in turn be computed from the Berry curvature, [49] and is related to a geometrical phase of the wave function [50], as well as to the Hall conductance [42].

For a HgTe/CdTe QW, we can relate the QW width w for HgTe to the topological invariant. When $w < w_c$ ($w > w_c$) the invariant is $\nu = 0$ ($\nu = 1$), so that for $w = w_c$ the system undergoes a topological phase transition. Furthermore, when $w < w_c$ the QSH conductance is zero, while for $w > w_c$ it is finite. This implies that when the system is in the inverted regime (CB below VB), so that $\nu = 1$, it is in a non-trivial topological phase, whereas for the normal band ordering when $\nu = 0$ it is in the topologically trivial phase. The reason that we can relate w to the topological invariant like this, is that the width of the HgTe QW determines if the bands are inverted or not. For a InAs/GaSb QW, we must know both the widths of the InAs layer and the GaSb layer to determine if we are in the topological phase. This is because in this system, electrons from InAs and holes from GaSb hybridize so that an inverted gap opens up.

Chapter 4

Diffusive and ballistic transport

To analyze the electron transport through the core-shell nanowires, we calculate the conductivity and the Seebeck coefficient for a nanowire subject to a voltage drop and a temperature difference, see Fig. 4.1. The calculations are made in two different limits: the diffusive limit, using the Boltzmann equation, and the ballistic limit. The reason for calculating the transport in these two different limits is that even though nanowires are known to show diffusive transport behavior, ballistic transport has been reported in shorter nanowire segments [51, 52, 53]. In this chapter we present the formalism of the methods, while the results are discussed in Chapter 8.

4.1 Electronic transport and thermoelectrics in quasi-one-dimensional systems

For a current density, J, we can write its contributions from an electrical bias V and a temperature gradient ∇T as

$$J = -\sigma \nabla V - \sigma_T \nabla T \tag{4.1}$$

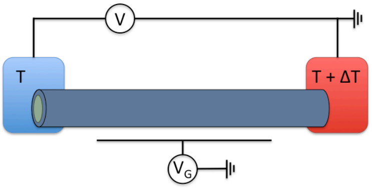

Figure 4.1: Sketch of the transport setup for the core-shell nanowire. Figure adapted from Paper I.

in a linear response regime. Here σ is the electrical conductivity (from an applied voltage), and σ_T is the "thermoelectrical conductivity" (from a temperature difference). Equation 4.1 is similar to Ohm's law, but has an extra term accounting for a charge current that arises due to a temperature gradient. We can also express this in terms of a current I and the conductances G and G_T, as

$$I = GV + G_T \Delta T. \tag{4.2}$$

We calculate the one-dimensional conductivities $\sigma = Gl/A$ and $\sigma_T = G_T l/A$ separately, where l is the nanowire length and A is its area, to be able to determine the Seebeck coefficient from

$$S = \frac{\sigma_T}{\sigma} = \frac{G_T}{G}. \tag{4.3}$$

The Seebeck coefficient is a measure of the thermoelectric properties of a system, or more specifically,

$$V_{th} = S\Delta T, \tag{4.4}$$

a proportionality constant for how the system relates a thermally induced voltage V_{th} in an open-circuit configuration to a temperature difference.

The conductance is proportional to the conductivity,

$$G = \sigma \frac{A}{l}, \tag{4.5}$$

scaled by the area A and the length l of the wire. In the diffusive limit we calculate the conductivity, since this is the quantity corresponding to the conductance, that is not dependent on A and l. However, in the ballistic limit the conductance is independent of l, since we assume that there is no scattering in the nanowire. Since we do not want to assume any specific wire length, we instead calculate G in the ballistic limit and compare to σ calculated in the diffusive limit.

4.2 Diffusive limit

We want to derive an expression for J, similar to Eq. 4.1, from the Boltzmann equation. Doing this, we are able to identify expressions for σ and S. In a semiclassical limit, we can find the current density from the distribution function. The method is inspired by Ref. [54], but we make no assumption about parabolicity of the bands, and we include all bands from our $\mathbf{k} \cdot \mathbf{p}$ results in our calculations. We here derive the equations used, in a similar manner to Ref. [55]. To obtain the distribution function, we solve the Boltzmann equation in the linear response regime, using the relaxation time approximation (RTA). By assuming a constant relaxation time, τ, for the time it takes for the electron distribution to relax, the integral part of the Boltzmann equation can be simplified, so that the equation can be solved; this is what we refer to as the RTA.

In equilibrium, the distribution is given by the Fermi-Dirac distribution

$$f_0(\mathbf{r},\mathbf{k}) = \frac{1}{1+\mathrm{e}^{[E(\mathbf{r},\mathbf{k})-E_F]/k_BT}} \tag{4.6}$$

where E is the energy, E_F is the Fermi level, $\mathbf{r}$ and $\mathbf{k}$ are real space and crystal momentum coordinates, and k_B is the Boltzmann constant. Close to equilibrium we can write the distribution of electrons as a sum of the equilibrium distribution and a non-equilibrium part δf,

$$f = f_0 + \delta f. \tag{4.7}$$

To find f we use the Boltzmann equation [56, 55]

$$\frac{df}{dt} + \mathbf{v}\cdot\nabla_{\mathbf{r}}f + \mathbf{F}\cdot\frac{1}{\hbar}\nabla_{\mathbf{k}}f = \left.\frac{df}{dt}\right|_{coll}, \tag{4.8}$$

with the velocity $\mathbf{v} = \frac{1}{\hbar}\nabla_{\mathbf{k}}E(\mathbf{r},\mathbf{k})$ and the force $\mathbf{F} = \nabla_{\mathbf{r}}E(\mathbf{r},\mathbf{k})$. The left hand side originates from the semiclassical equations of motion for the electrons, and the right hand side is an integral that accounts for scattering processes. In the RTA this scattering integral becomes

$$\left.\frac{df}{dt}\right|_{coll} = -\frac{\delta f}{\tau_f}. \tag{4.9}$$

Furthermore we use the assumption that we are close to equilibrium by approximating $\frac{df}{dt} = 0$, so that the Boltzmann equation becomes

$$\mathbf{v}\cdot\nabla_{\mathbf{r}}(f_0+\delta f) + \mathbf{F}\cdot\frac{1}{\hbar}\nabla_{\mathbf{k}}(f_0+\delta f) = -\frac{\delta f}{\tau_f}. \tag{4.10}$$

Now we assume that we are close to equilibrium, so that $f_0 \gg \delta f$ and $|\nabla_{\mathbf{r},\mathbf{k}}f_0| \gg |\nabla_{\mathbf{r},\mathbf{k}}\delta f|$. Based on these assumptions we make the approximation that we can remove small terms, which gives us an equation for the out-of-equilibrium part of the distribution function,

$$\mathbf{v}\cdot\nabla_{\mathbf{r}}f_0 + \mathbf{F}\cdot\frac{1}{\hbar}\nabla_{\mathbf{k}}f_0 = -\frac{\delta f}{\tau_f}, \tag{4.11}$$

that we can use to find an expression for $\mathbf{J}$. Since the equilibrium part of the distribution function given by the Fermi-Dirac distribution in Eq. 4.6 is symmetric in $\mathbf{k}$, it does not contribute to the current. Hence we can find the desired transport properties from δf.

The total number of carriers is given as a sum over all possible momenta (states in the first Brillouin zone), so that the average carrier density is

$$n(\mathbf{r},t) = \frac{1}{\Omega}\sum_{\mathbf{k}} f(\mathbf{r},\mathbf{k},t), \tag{4.12}$$

where we have introduced a small normalization volume Ω. The electron current density is given by this sum, weighted with carrier velocity and charge ($-e$ for the electron)

$$\mathbf{J}(\mathbf{r}, t) = -\frac{e}{\Omega}\sum_{\mathbf{k}} \mathbf{v}(\mathbf{k}) f(\mathbf{r}, \mathbf{k}, t) \tag{4.13}$$

We can here insert the expression for the distribution function given by Eq. 4.11 and compare to the expression for the current density in Eq. 4.1 to find σ and S. To avoid summations, we go from sums to integrals in the standard way

$$\sum_{\mathbf{k}} g(\mathbf{k}) \rightarrow \frac{\Omega}{4\pi^3}\int g(\mathbf{k}) d^3 k, \tag{4.14}$$

or in one dimension

$$\sum_{k} \rightarrow \frac{L}{2\pi}\int dk. \tag{4.15}$$

The integrals are carried out over the first Brillouin zone. We find the expressions for the conductivities as

$$\sigma = 2e^2 \int v^2(k)\tau \left(-\frac{\partial f(E, E_F)}{\partial E}\right) dk, \tag{4.16}$$

and

$$\sigma_T = -2eT\int v^2(k)\tau(E - E_F)\left(-\frac{\partial f(E, E_F)}{\partial E}\right) dk. \tag{4.17}$$

4.2.1 Inter- and intraband relaxation

In Paper 1 we have considered a case where no interband relaxation is possible, so that we can treat each conducting channel separately. We here justify this approach, by showing that by allowing all channels to scatter to every other channel, the resulting transport properties will remain the same. Generalizing the conductivity so that we can allow for interband relaxation, the conductivity in each band n (where $n = 1, 2, \ldots, N$), is given by

$$\bar{\sigma} = \begin{pmatrix} \sigma_1 \\ \sigma_2 \\ \vdots \\ \sigma_N \end{pmatrix} = \int \bar{\tau}\mathbf{g}(k) dk \tag{4.18}$$

where $\bar{\tau}$ is a matrix with relaxation times in and between bands, and

$$\mathbf{g}(k) = 2e^2 \begin{pmatrix} v_1^2(k)\left(-\frac{\partial f_1}{\partial E}\right) \\ v_2^2(k)\left(-\frac{\partial f_2}{\partial E}\right) \\ \vdots \\ v_2^N(k)\left(-\frac{\partial f_N}{\partial E}\right) \end{pmatrix}. \tag{4.19}$$

The total conductivity is given by a sum over the conductivities in all bands,

$$\sigma_{tot} = \sum_n \sigma_n. \tag{4.20}$$

We consider two cases; the first allows for intraband relaxation only, while the second one allows for relaxation between all bands. When only intraband relaxation is allowed, the relaxation matrix is given by $\bar{\tau} = \tau \mathbb{1}$, so that the coupled equations in (4.18) become uncoupled:

$$\sigma_n^{intra} = \int \tau g_n(k) dk \tag{4.21}$$

and our total conductivity is

$$\sigma_{tot}^{intra} = \sum_n \sigma_n^{intra} = \sum_n \int \tau g_n(k) dk. \tag{4.22}$$

For the second case, we limit our analysis to a case where all bands relax to all other bands with equal probability. We have our relaxation time matrix as

$$\bar{\tau} = \tau_N \begin{pmatrix} 1 & 1 & \dots & 1 \\ 1 & 1 & & \\ \vdots & & \ddots & \\ 1 & & & 1 \end{pmatrix}, \tag{4.23}$$

leading to the conductivity

$$\sigma_n^{inter} = \sum_{n'} \int \tau_N g_{n'}(k) dk, \tag{4.24}$$

and in total

$$\sigma_{tot}^{inter} = \sum_n \sigma_n^{inter} = \sum_n \sum_{n'} \int \tau_N g_{n'}(k) dk = N \sum_{n'} \int \tau_N g_{n'}(k) dk, \tag{4.25}$$

so if $\tau_N = \tau / N$ we have that $\sigma_{tot}^{intra} = \sigma_{tot}^{inter}$.

4.3 Ballistic limit

Following Ref. [5], we find the following expressions for the conductances, G and G_T, from a small applied voltage V and a small temperature difference ΔT, respectively:

$$G = \frac{e^2}{2\pi} \int_{-\infty}^{\infty} \left(-\frac{\partial f(E, E_F)}{\partial E} \right) \left(v_{\rightarrow}(k) - v_{\leftarrow}(k) \right) T(k) dk \tag{4.26}$$

$$G_T = -\frac{e}{2\pi} \int_{-\infty}^{\infty} \frac{E - E_F}{T} \left(-\frac{\partial f(E, E_F)}{\partial E} \right) \left(v_{\rightarrow}(k) - v_{\leftarrow}(k) \right) T(k) dk \tag{4.27}$$

with $v_{\rightarrow}$ ($v_{\leftarrow}$) being the velocity of rightmoving (leftmoving) electrons, and $T(k) = \mathbb{1}$ the scattering matrix (we assume that no scattering elements are present in the nanowire). Here we have assumed that we have Kramers degeneracy, $E_{\uparrow}(-k) = E_{\downarrow}(k)$, so that $E(k)$ must be even, and the first order term vanishes under the k-integral when expanding the integrand in Taylor series in k.

4.4 Mott formula

An alternative way of calculating the Seebeck coefficient is using the Mott formula [57]. In a low temperature limit, S can be approximated by

$$S = \frac{\pi^2}{3} \frac{k_B^2 T}{e} \left. \frac{d(\ln \sigma(E))}{dE} \right|_{E=E_F} \tag{4.28}$$

in the diffusive limit. Likewise, we can write down an approximate expression for the Seebeck coefficient in the ballistic limit using the conductance G instead of the conductivity σ.

We compare the calculated conductivities and conductances, and the Seebeck coefficient calculated in the diffusive and the ballistic limits. The results are discussed in Chapter 8.

Chapter 5

Quantum dots

Quantum dots are (quasi-)zero-dimensional structures, confining electrons in all spatial directions. Physically, they can be thought of as artificial atoms, in the sense that the electron energy levels are quantized due to the confinement potential. QDs can be realized in many different ways [58], but here we focus on QDs that are epitaxially grown between wurtzite barriers in zincblende InAs nanowires. However, apart from epitaxial growth, QDs can be realized in other ways, e.g., by applying gates to a two-dimensional electron gas to create electron confining potentials.

In Papers III and IV we study parallel DQDs and the evolution of the electron energy levels under a magnetic field and one-electron level detuning. In contrast to the $\mathbf{k} \cdot \mathbf{p}$ model employed in Papers I and II, we need a many-body Hamiltonian to describe the QD systems in Papers III and IV. The main reason for this is that in the QDs we study, the energy scale of the Coulomb interaction between electrons is relatively large and governs some of the most important physical effects. We begin this chapter by briefly explaining the mechanisms of a single QD in an electrical measurement setup. Our treatment follows the more detailed discussions in Refs. [59, 60, 61].

5.1 Constant interaction model: Coulomb blockade

We consider a single QD, tunnel coupled to source and drain contacts, and capacitively coupled to a gate, see Fig. 5.1. We are interested in probing the QD spectrum using transport measurements, and from a theoretical point of view, to calculate the spectra of and the transport through a QD. There are two main effects that are taken into account here: the quantized energy levels of the QD and the Coulomb repulsion between the electrons populating the QD. The simplest model for this is the constant interaction model. The

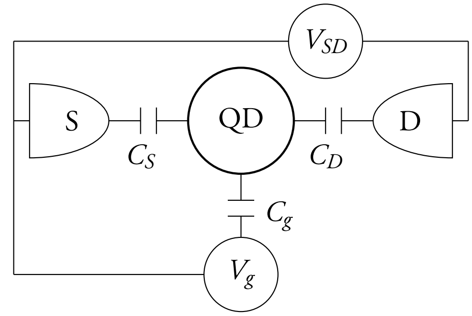

Figure 5.1: Measurement setup for a quantum dot tunnel coupled to source and drain contacts, with applied voltage V_{SD}, and capacitively coupled to a gate voltage V_g.

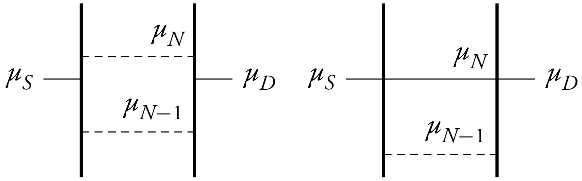

Figure 5.2: QD in Coulomb blockade (left) and transport (right) regime

total energy $E(N)$ of the N electrons on the QD is given by

$$E(N) = \sum_{i=1}^{N} \varepsilon_i + E_{stat}(N) \tag{5.1}$$

where ε_i are the single-electron levels (including spin, so that $\varepsilon_1 = \varepsilon_2$ etc. when no magnetic field is present) and

$$E_{stat}(N) = \frac{eN^2}{2C} \tag{5.2}$$

the electrostatic energy from all electrons in the QD. We define the single particle level spacing between states i and $i+1$ as

$$\Delta_{i+1} = \varepsilon_{i+1} - \varepsilon_i, \tag{5.3}$$

and the chemical potential μ_N in the QD as the energy needed to add an Nth electron,

$$\mu_N = E(N) - E(N-1), \tag{5.4}$$

given that the QD is already occupied by $N-1$ electrons. For a Kramers degenerate system, note that $\Delta_{i+1} = 0$ for an even electron number $i+1$. The charging energy of the QD is given by $U = \frac{e}{C}$, where $C = C_g + C_S + C_D$ is the self-capacitance of the QD, using the gate, source, and drain capacitances defined in Fig. 5.1. The charging energy is determined by the size of the QD (smaller QD implies larger U because of the increased Coulomb interaction).

We assume in the rest of this chapter that both the temperature and the tunnel coupling to the leads are small in comparison to the charging energy. Furthermore, we can write the charging energy in terms of the electrostatic energy as

$$U = E_C(N+1) - E_C(N) \tag{5.5}$$

where the difference E_C in electrostatic energy is

$$E_C(N) = E_{stat}(N) - E_{stat}(N-1). \tag{5.6}$$

With the use of equations 5.1,5.3, 5.4, 5.5, and 5.6 we can write the difference between two chemical potentials as

$$\mu_N - \mu_{N-1} = \Delta_N + U. \tag{5.7}$$

The gate voltage will result in the addition of an additional term to the total energy in Eq. 5.1 so that

$$E(N, V_g) = \sum_{i=1}^{N} \varepsilon_i + E_{stat}(N) - |e| N \alpha_g V_g. \tag{5.8}$$

Here the lever arm $\alpha_g = C_g/(C_D + C_S + C_g)$ is introduced. If we use this gate dependent expression for the total energy to calculate the chemical potential in Eq. 5.4 we find that

$$\mu_N(V_g) = \mu_N(V_g = 0) - |e|\alpha_g V_g, \tag{5.9}$$

so that the chemical potentials can be tuned linearly with the gate.

The QD and lead systems can be in one of two regimes, either in a Coulomb blockade or a transport regime, shown in Fig. 5.2, where transport can only take place if the QD chemical potentials is aligned with the chemical potentials of the source and drain contacts. Note that we here only tune the gate voltage, the bias voltage V_{SD} is kept at a fixed small value. The Coulomb blockade mechanism implies that if we measure the conductance through the QD, while sweeping the gate voltage V_g, we will see peaks in the conductance. We can write μ_N in terms of $V_g^{(N)}$, the gate voltage for where I has its Nth peak, so that the chemical potential (and eventually the single electron spectrum) can be deduced from this measurement, using Eq. 5.9. The peaks appear when $\mu_S = \mu_D = \mu_N(V_g^{(N)}) = \mu_N(V_g = 0) - |e|\alpha_g V_g^{(N)}$, so the difference between two peaks at $V_g^{(N)}$ and $V_g^{(N+1)}$ can be written as

$$V_g^{(N+1)} - V_g^{(N)} = \frac{\mu_{N+1}(V_g = 0) - \mu_N(V_g = 0)}{|e|\alpha_g} = \frac{\Delta_{N+1} + U}{|e|\alpha_g}. \tag{5.10}$$

For an external parameter, such as an applied magnetic field, we can see how the V_g position of the peaks evolve with varying parameter strength. If the capacitances in the system and the background charge are unchanged (this is usually a good approximation), $V_g^{(N)}$ is a measure of how ε_N evolves with the external parameter. Hence we study the difference of the peaks to find the QD spectrum.

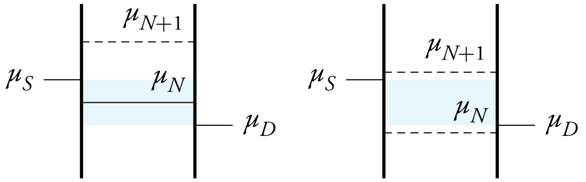

Figure 5.3: QD in transport (left) and Coulomb blockade (right) regime

5.1.1 Charge stability diagrams: Coulomb diamonds

We now lift the restriction on V_{SD} that it should be very small (but we assume that V_{SD} is applied symmetrically to source and drain contacts). The transport through the QD is then also affected by changes in V_{SD}, which is usually tuned in experiments together with V_g. The finite bias voltage results in a bias window where transport can take place, see Fig. 5.3. In the Coulomb blockade regime there is no QD chemical potential in the bias window (defined as $\mu_D - \mu_S$, marked with blue in Fig. 5.3), and the transport through the system is blocked. However, the blockade can be lifted by tuning the gate voltage so that a chemical potential is situated in the bias window. As long as there is a QD chemical potential μ_N inside the bias window, transport can take place, and the electron number fluctuates between N and $N - 1$, as in the last section. Similarly if there are M chemical potentials in the bias window the electron number on the QD can fluctuate between N and $N - M$.

The transport through the QD, now affected by two quantities, is often understood in terms of charge stability diagrams. The system is subject to sweeping of both the gate voltage and the bias voltage, and the resulting current I, or more commonly, the differential conductance dI/dV_{SD} is plotted as a function of both voltages in a two-dimensional plot. We will here give the very basics of the charge stability diagrams for single QDs, that exhibits the typical Coulomb diamonds, necessary to understand the results of Papers III and IV.

Figure 5.4 shows a sketch of a typical charge stability diagram for a single QD. The transport processes are clearly visible as lines in dI/dV_{SD}, since at these lines the current changes. Inside the lines (white areas), around $V_{SD} = 0$, in the larger diamond-shaped areas, the system is in Coulomb blockade, and no transport can take place. The fully depleted system ($N = 0$) is shown by a large non-closed structure at low gate voltage. When V_g is increased, more electrons can populate the QD. For odd occupation number N, the diamonds are smaller, since it is close in energy to add the one-electron Kramers partner to the last occupied one-electron energy level, compared to the Coulomb repulsion energy inside the QD. This can be seen from

$$\mu_{N+1} - \mu_N = \Delta_{N+1} + U = \begin{cases} U, & N \text{ odd} \\ \epsilon_{N+1} - \epsilon_N + U, & N \text{ even} \end{cases} \tag{5.11}$$

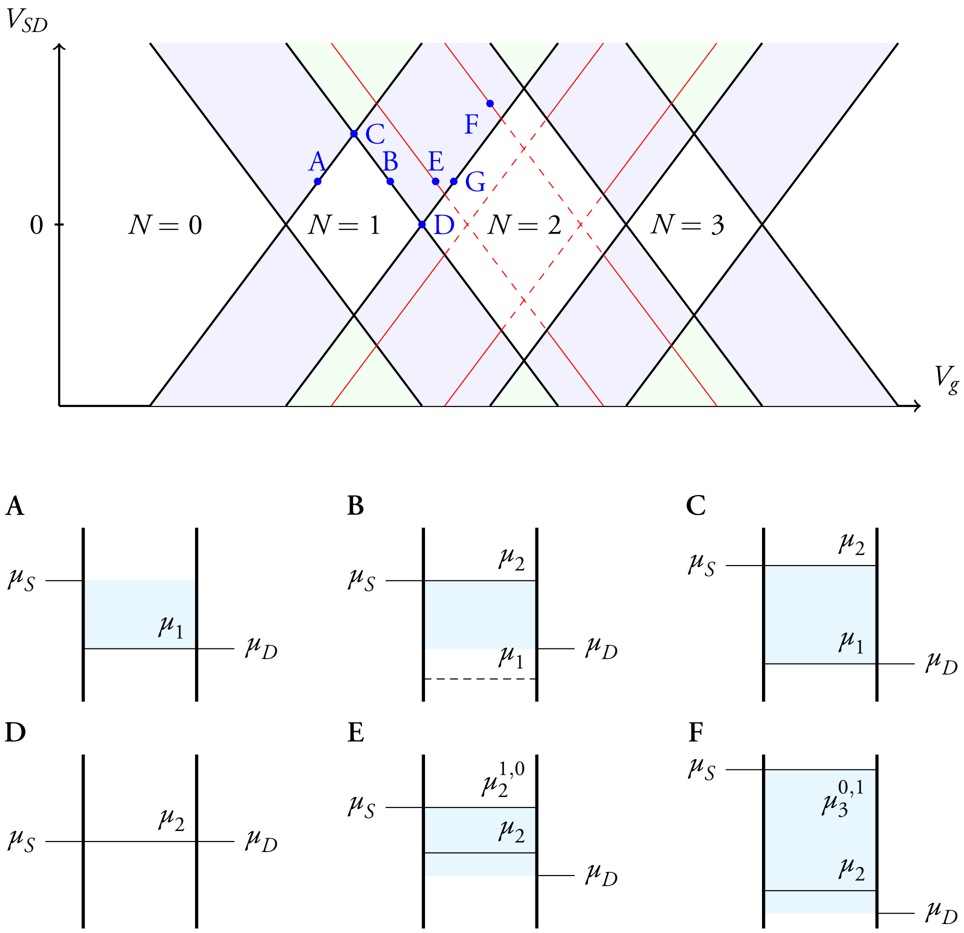

Figure 5.4: Above: Coulomb diamonds for N electrons in the quantum dot. Below: Sketch of the chemical potentials at the marked points in the charge stability diagram

where we have used Eq. 5.7, together with the fact that $\Delta_{i+1} = 0$ for an even $i + 1$. For an even occupation number, the diamonds are larger, since it is not only Coulomb blockade that suppresses transport, but also the fact that the electron needs a higher energy to go to the next single-electron level (since two spins occupy a spin-degenerate level).

As an example we, discuss the $N = 1$ diamond (for $V_{SD} \geq 0$). At the lines enclosing it towards lower gate voltages, the energy level μ_1 aligns with μ_D (marked A in Fig. 5.4), while the line towards higher V_g corresponds to when $\mu_2 = \mu_S$ (marked B). Where these lines intersect (C) both μ_1 and μ_2 enters the transport window, i.e., $\mu_1 = \mu_D$ and $\mu_2 = \mu_S$. This means that above this point, in the green shaded area in the sketch, two-electrons can occupy the QD, and the occupancy can fluctuate between $N = 0, 1$ and 2. Where the $N = 1$ and $N = 2$ diamonds meet (D) we have that $\mu_2 = \mu_D = \mu_S$, so transport is not forbidden. In the regime between point D and the green two-electron area above C, marked in blue, one level is situated in the bias window, so that one or zero electrons can populate the QD, and tunneling in and out from the QD is possible.

5.1.2 Excited states

Apart from the ground state transition lines that enclose the Coulomb blockade diamonds, it is also possible to see transport involving excited states in the QD, when the bias voltage becomes larger than the one-particle level spacing: $eV_{SD} > \Delta_{N+1}$ [60, 59]. It is interesting to study the excited state transition lines, since their spacing (or the spacing between them and the lines from ground state transitions) gives us the single particle level spacing (in a similar manner as in Eq. 5.10). We use the definition $\mu_N^{n,m} = E^n(N) - E^m(N-1)$ for a transition to and/or from an excited state, where $E^n(N)$ is the (energy of the) nth excited N state (and $E^m(N-1)$ is the mth excited $N-1$ state). We define $\mu_N^{n,0}$ so that $\mu_N^{n,0} > \mu_N^{0,0} = \mu_N$ for all $n > 0$.

An example of an excited state line can be seen at mark E in Fig. 5.4, where an excited energy level for $N = 2$ enters the bias window, so that the QD goes from the $N = 1$ ground state to an excited $N = 2$ state. This line lies in a regime where transport is already permitted, and N fluctuates between $N = 1$ and $N = 2$ (μ_2 enters the bias window at mark B and leaves it at G). However, such an excited state cannot contribute to transport "on its own" in the bias window; if μ_N leaves the bias window, so does all $\mu_N^{1,0}$, $\mu_N^{2,0}$ ... etc. This is because we define the excited state as $\mu_N^{1,0} = E_N^1 - E_{N-1}^0$, where E_N^1 is the first excited N-electron state. This means that when $\mu_N < \mu_D$, there can be no Nth electron in the QD, and the excited state cannot contribute to transport anymore.

It is also possible to go from an excited N state, to a ground state or to an excited state with $N-1$ electrons. Such a transition line can be seen at mark F in Fig. 5.4 for $N = 3$. This line appears when transport from an excited $N = 2$ state to the $N = 3$ ground state becomes possible, i.e., when $\mu_3^{0,1}$ enters the bias window. For transitions that start from an excited state relaxation times become important. If the relaxation times are very short these transitions will not be visible.

Chapter 6

Parallel double quantum dots

Papers III and IV both treat electron transport through a parallel DQD. The main idea is to probe the spin states in the DQD in a transport measurement setup. This project is done in the framework of an experimental collaboration, but we here focus mainly on the theory part of the project.

6.1 Parallel and serial quantum dots

DQDs can be connected either in serial or in parallel in a measurement setup. In serial DQDs transport through the system can take place only when both chemical potentials in the QDs are aligned. It is also possible to go via excited states, leading to triangular windows in the gate and bias voltages where transport can be studied. In such a configuration a leakage current can flow in the spin blockade regime, because of spin relaxation [62, 63, 64, 65, 66]. However, for parallel DQDs there is no similar blockade mechanism of the transport; electrons can tunnel through either of the QDs irrespective of the existence of an aligned level in the other QD. Instead it is possible to directly probe the spin transitions using tunnel spectroscopy via electrical measurements.

The DQD we study is made from epitaxially defined single QDs in InAs nanowires, subject to side gates that create two electron pockets, or a DQD, inside the disc-shaped single QD, see Fig. 6.1. Using source and drain contacts at the ends of the wire (or, anywhere on the wire outside the QD), the DQD will be electrically contacted in parallel in the measurement setup. The DQD can be fully depleted and we can tune the interdot coupling using the side gates. Furthermore, we can detune the one-electron energy levels in each of the QDs without blocking the transport, something that is not possible in serial DQDs, which gives better possibilities for spectroscopy of the system.

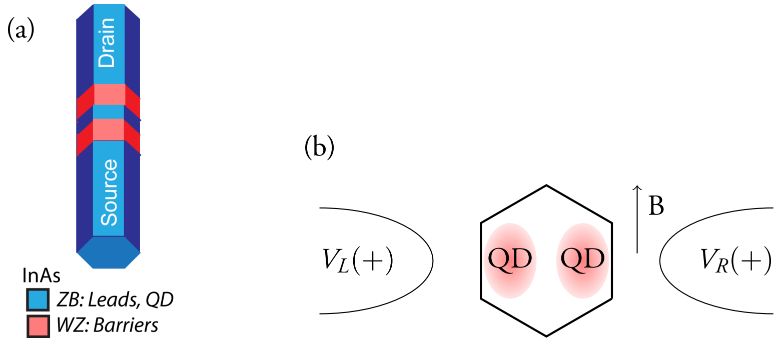

Figure 6.1: Sketches showing (a) epitaxially defined single quantum dot in the InAs nanowire and (b) the formation of the DQD using sidegates on the epitaxially defined QD. Figure (a) adapted from Paper IV.

Many earlier works on parallel DQDs where performed using GaAs [67, 68, 69, 70] which has a small *g*-factor (compared to that of InAs) , so that the spin splitting cannot be resolved if B is not very large. In InAs DQDs the hyperfine interaction is small (compared to that in GaAs) [63, 64], so that we can find the coupling strength due to SOC between singlet and triplet states from the magnitude of the anticrossing of the states under a magnetic field (approximating the hyperfine coupling to be zero).

The model we use to reproduce the experimental results consists of a simple few-electron Hamiltonian with a single electron energy level on each QD, including exchange energy, SOC and the Zeeman effect. In the next section we present the Hamiltonian used to calculate the energies of the isolated DQD system. The resulting spectrum is used as input to a master equation, presented in Chapter 7. In the rest of this chapter we discuss some results from Papers III and IV.

6.2 Model

The DQD is modeled using a few-electron Hamiltonian with one single-electron energy level on each QD, similar to the model used in Ref. [71]. The use of such a simple model is motivated by the good match of the theoretical and the experimental results in Papers III and IV. We assume that the one-electron energy levels are unaffected by the number N of electrons populating the QDs. The Hamiltonian is given by

$$H = H_0 + H_{SO} + H_B \tag{6.1}$$

with

$$\begin{aligned} H_0 = & \sum_{\substack{i=1,2\\ \sigma=\uparrow,\downarrow}} \epsilon_i c^\dagger_{i\sigma} c_{i\sigma} - \sum_{\substack{i,j=1,2\\ i\neq j\\ \sigma=\uparrow,\downarrow}} t c^\dagger_{i\sigma} c_{j\sigma} \\ & + \sum_{\substack{i,j=1,2\\ i\neq j\\ \sigma,\sigma'=\uparrow,\downarrow}} \left[\frac{U_{ii}}{2} \delta_{\sigma\neq\sigma'} c^\dagger_{i\sigma} c^\dagger_{i\sigma'} c_{i\sigma'} c_{i\sigma} + \frac{U_{ij}}{2} c^\dagger_{i\sigma} c^\dagger_{j\sigma'} c_{j\sigma'} c_{i\sigma} - \frac{V_x}{2} c^\dagger_{i\sigma} c^\dagger_{j\sigma'} c_{j\sigma} c_{i\sigma'} \right], \end{aligned} \tag{6.2}$$

$$H_{SO} = \sum_{\substack{i,j=1,2\\ i\neq j}} (-1)^i i t_{SO} (-c^\dagger_{i\uparrow} c_{j\uparrow} + c^\dagger_{i\downarrow} c_{j\downarrow}), \tag{6.3}$$

and

$$H_B = \sum_{i=1,2} \frac{B}{2} \left[\cos\theta (c^\dagger_{i\uparrow} c_{i\uparrow} - c^\dagger_{i\downarrow} c_{i\downarrow}) + \sin\theta (c^\dagger_{i\uparrow} c_{i\downarrow} + c^\dagger_{i\downarrow} c_{i\uparrow}) \right], \tag{6.4}$$

where ϵ_i is the one-electron energy on QD i, U_{ii} and U_{ij} the intradot and interdot charging energies, respectively, and V_x the value of the exchange integral. The spin-orbit coupling parameter t_{SO} is assumed to be linear in t so that $t_{SO} = \alpha t$, since it accounts for a tunneling process and a spin flip. The magnetic field term B in the Hamiltonian is assumed to be the same on the two QDs, and is related to the applied magnetic field $\mathbf{B_{ext}}$ through the effective g-factor $|g^*|$ and the Bohr magneton μ_B as $B = \mu_B |g^*| B_{ext}$, where $B_{ext} = |\mathbf{B_{ext}}|$. We assume that $|g^*|$ is unchanged during the measurements. The quantization axis is chosen along the SO field direction (along $\mathbf{B_{SO}}$). The angle between $\mathbf{B_{SO}}$ and $\mathbf{B_{ext}}$ [72] is set to $\theta = \pi/2$. We do not include any hyperfine interaction in the model, since it is small [63, 64] and the experimental data could be well-reproduced without it.

6.3 One- and two-electron states

The one-electron energy levels can be adjusted using the sidegates V_L and V_R according to

$$\begin{aligned} \epsilon_L &= \alpha_{LL} V_L + \alpha_{RL} V_R \\ \epsilon_R &= \alpha_{LR} V_L + \alpha_{RR} V_R \end{aligned} \tag{6.5}$$

where the lever arms α_{ij} accounts for how much gate V_i affects ϵ_j. However, we use a detuning parameter Δ to model the detuning, defined so that $\epsilon_2 - \epsilon_1 = \Delta$. Irrespective of the detuning, the one-electron eigenstates can be considered in a weak or a strong coupling regime, shown for the one-electron states in Fig. 6.2. If the coupling between the QDs is weak ($t \to 0$), the eigenstates are given by the doublet states $D(\uparrow, 0)$ and $D(0, \downarrow)$. These

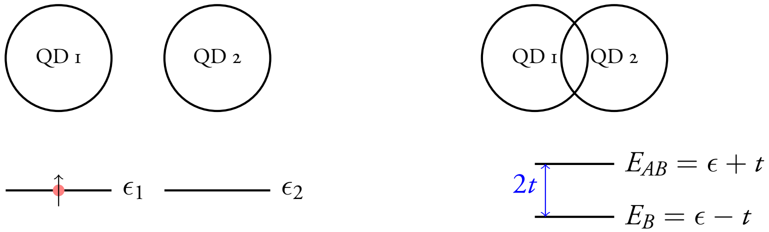

Figure 6.2: One electron states in a weak coupling regime (left) and a strong coupling regime (right). In the weak coupling regime $E = \epsilon_1 = \epsilon_2$, while in the strong coupling regime the tunneling coupling splits the degenerate energies into bonding and anti-bonding states. In the left panel we have indicated the doublet state $D(\uparrow, 0)$.

Figure 6.3: Detuning between the single electron energy levels in the quantum dots. The two-electron ground state changes when detuning the one electron levels. When the detuning becomes strong enough to overcome the Coulomb repulsion, the S(2,0) becomes the ground state.

states are pairwise degenerate for a finite level detuning and zero magnetic field. In a regime where the coupling is large, the ground states are instead given by bonding ($B(\uparrow)$, $B(\downarrow)$) and anti-bonding states ($AB(\uparrow)$, $AB(\downarrow)$).

When two electrons occupy the DQD the eigenstates are given by singlet (S) and triplet (T) states. Figure 6.3 shows how the two-particle states evolve under detuning of the one-electron levels (but under a zero magnetic field $B = 0$). For the two-electron occupation we define the exchange energy as

$$J = E(S(1,1)) - E(T(1,1)), \tag{6.6}$$

where the energies are for $B = 0$. This implies that J will increase with t. Note that although V_x is related to the singlet triplet separation J, they are not the same quantity. If the one-electron levels are aligned (so that $\Delta = 0$) and $B = 0$, the singlet state $S(1,1)$ with one electron in each QD is the ground state for $J < 0$ (if $J > 0$, the triplet state $T(1,1)$ is the ground state). The excited singlet states $S(2,0)$ and $S(0,2)$ are (very) high in energy compared to the ground state and the three-fold degenerate triplet state $T(1,1)$. Under detuning the $S(2,0)$ (or $S(0,2)$) state will become the ground state when Δ is large enough.

Under a magnetic field the triplet states will split into $T_+(1,1)$ (lowest in energy), $T_0(1,1)$ and $T_-(1,1)$. For a critical value of the magnetic field the lowest lying triplet state will anticross with the singlet ground state, so that a ground state transition takes place. A similar transition takes place between the triplet state $T_+(1,1)$ and the singlet state $S(2,0)$ when increasing the detuning strength (under a finite magnetic field).

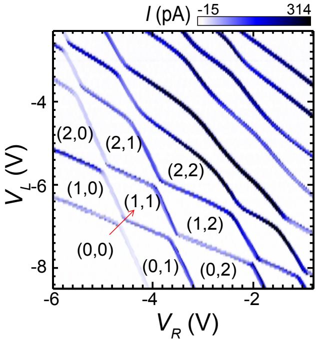

Figure 6.4: Honeycomb charge stability diagram for the double quantum dot. Figure adapted from Paper III.

6.4 Charge stability diagrams for the DQD

Honeycomb charge stability diagrams are a way to visualize the current data from a parallel DQD experiment, similar to the Coulomb diamonds mentioned in Chapter 5, but showing the current I as a function of both side gates. An example is given in Fig. 6.4, taken from Paper III. In a similar way to the Coulomb diamonds we can see when the system is subject to Coulomb blockade and when there is transport through the system. The different blockade regimes are labeled (N_L, N_R) for when there is occupancy N_L and N_R in the left and the right QD, respectively.

To gain more information about a specific transition between two DQD states, we can again study Coulomb diamonds, but plotted against a voltage vector $V_{L,R}$ instead of the gate voltage, typically taken as the red arrow in Fig. 6.4, so that we go as straight as possible from one electron configuration to another. The simplest way to choose this vector is of course $V_{L,R} = \frac{1}{\sqrt{2}}(V_L + V_R)$. However, in practice there are lever arms coupling the gate voltages to the system differently, that have to be taken into account. The voltage vector quantity $V_{L,R}$ can effectively be seen as a gate voltage applied to both QDs in our system, since it leaves the interdot tunnel coupling t approximately constant, while tuning the single electron energy levels in each QD.

Chapter 7

Transport through the double quantum dot

For the few-body Hamiltonian used to describe the DQD in Papers iii and iv we need to employ a different transport method than the ones described in Chapter 4. This is because we now consider transport through many-body quantum states in the QD, which a one-electron transport model fails to describe. We wish to calculate the current through the DQD system, and hence the current through the nanowire. This is achieved by using a master equation solved for the non-equilibrium populations, derived using a lowest order perturbation expansion in the tunnel couplings between the DQDs and the source/drain contacts. The transport model is used together with the calculated energies from the Hamiltonian for the DQD system, given in equation 6.1. In this chapter we first introduce the Hamiltonian for the full system, containing both the DQD and the source and drain contacts. In the following section we present a general introduction to the master equation formalism. For a detailed discussion, see e.g., Refs. [73, 74]. In the following sections we present the transport equations we solve to calculate the current for Papers iii and iv.

7.1 Hamiltonian for the full system

The Hamiltonian for the full system, including the DQD and the source and drain leads is given by

$$H_{tot} = H + H_R + H_T \tag{7.1}$$

where H is the DQD Hamiltonian (Eq. 6.1), assumed to be diagonalized for the many-body eigenstates $\{|a\rangle\}$ in the DQD, so that $H = \sum_a E_a |a\rangle\langle a|$. The probability for the DQD to be in state $|a\rangle$ is given by P_a. The source and drain contacts are considered in the reservoir Hamiltonian $H_R = \sum_r H_r$, where the reservoir index in this case is given by $r = S, D$ (but this can easily be generalized to a system with arbitrarily many reservoirs). The source and drain leads are modeled by

$$H_r = \sum_{\sigma k} E_{r\sigma k} c^{\dagger}_{r\sigma k} c_{r\sigma k}, \tag{7.2}$$

where $c^{\dagger}_{r\sigma k}$ $(c_{r\sigma k})$ creates (annihilates) an electron in the lead r with energy $E_{r\sigma k}$ and spin polarization σ. We assume that electron distributions in the reservoirs r can be described by Fermi functions

$$f_r(E - \mu_r) = \frac{1}{1 + \mathrm{e}^{(E-\mu_r)/k_B T}}, \tag{7.3}$$

and that they are so large that the chemical potential μ_r is fixed and their physical properties can be assumed to be unaffected by adding or removing an electron. This means that the densities in the leads are the same for all times. The tunneling between the DQD and the leads is described by

$$H_T = \sum_{r\sigma kN} \sum_{\substack{a' \in N \\ a \in N-1}} \left(T^{d'a}_{r\sigma} \left| d' \right\rangle \left\langle a \right| c_{r\sigma k} + (T^{ad'}_{r\sigma})^* \left| a \right\rangle \left\langle d' \right| c^{\dagger}_{r\sigma k} \right), \tag{7.4}$$

where we have introduced the transition matrix $T^{ad'}_{r\sigma}$. The elements of $T^{ad'}_{r\sigma}$ are calculated according to

$$T^{ad'}_{r\sigma} = \sum_{d=1,2} t_r t_d \langle d' | \, d^{\dagger}_{d\sigma} \, | a \rangle + h.c. \tag{7.5}$$

using the coupling parameters t_1, t_2, t_S and t_D for the separate QDs and for the source and drain, respectively. The operator $d^{\dagger}_{d\sigma}$ $(d_{d\sigma})$ creates (annihilates) an electron in dot d with spin σ.

The spin index σ sees to that the process is allowed (spin is a good quantum number and is conserved outside the DQD). The transition probabilities $t_{aa'}$ between states $|a\rangle$ and $|d'\rangle$ is found from solving for the isolated DQD system.

7.2 The master equation

The main idea of the master equation approach, is that we are mainly interested in some small system (in our case the DQD) coupled to a number of reservoirs (such as the source and drain contacts). We are mainly interested in the small system, and want to find an equation for its density operator. In short, a density operator $\rho(\tau)$ (at time τ) for a mixed ensemble can be defined as

$$\rho(\tau) = \sum_a p_a \left| \Psi_a(\tau) \right\rangle \left\langle \Psi_a(\tau) \right| \tag{7.6}$$

with probabilities p_a to be in the states $|\Psi_a(\tau)\rangle$. Here we consider $\rho(\tau)$ to be the density operator for the full system, including the DQD and the source and drain contacts. The master equation is an equation for the time evolution of the density operator and can be derived from the von Neumann equation

$$\frac{d\rho(\tau)}{d\tau} = -\frac{i}{\hbar}\left[H_{tot}, \rho(\tau)\right] \tag{7.7}$$

where we have introduced the Hamiltonian of the full system H_{tot} . We integrate the equation of motion from some initial time τ_0 to τ and take the trace of the density operator over the reservoir states to find an equation for the reduced density operator $\rho_S(\tau) = \mathrm{tr}_R\{\rho(\tau)\}$, since the physical properties we are interested in are contained in this reduced density operator for the small system. The resulting equation is the master equation. The master equation is given in general form like

$$\frac{d}{d\tau}\rho_S(\tau) = \int d\tau' W(\tau - \tau')\rho(\tau') \tag{7.8}$$

where W is some problem-dependent kernel dependent on H_{tot}. The master equation is typically solved under a number of approximations, suitable for the system. We consider one of the simplest cases, a rate equation.

The density operator is considered to be independent of time, since we want to solve for a stationary state, so it can be taken out of the integral in Eq. 7.8. In addition, we do not consider any coherences (non-diagonal elements in the density matrix), which is a good approximation in the limit where the interdot coupling τ is very large. However, if τ would become very small this would be violated, and we would need to have a more sophisticated model, allowing for coherent states. The fact that we don not take coherences into account results in a density matrix for the DQD that can be chosen to be diagonal (in the same basis) for all times τ.

7.3 Rate equation

Because our density matrix is approximated as a diagonal matrix, we simply write it as a vector $\mathbf{P} = \mathrm{diag}(P)$, containing the probabilities $P_a(\tau) = \langle a| \rho_S(\tau) |a\rangle$ for the many-body eigenstates $\{|a\rangle\}$ in our DQD. The master equation for the DQD can then be written on the form [75, 76]

$$\frac{d\mathbf{P}}{d\tau} = M\mathbf{P}, \tag{7.9}$$

where the matrix M contains all possible transitions in the full system. We are interested in the stationary solution $\frac{d\mathbf{P}}{d\tau} = 0$.

For a given state $|a'\rangle$ with $N_{a'} = N_a + 1$ and $N_{a''} = N_{a'} + 1$, an explicit version of the rate equation can be written down as

$$
\begin{aligned}
\frac{dP_{a'}}{d\tau} = \sum_r \Bigg[& \sum_a \Gamma^r_{a'a} \left(f_{r,a'a} P_a - \bar{f}_{r,a'a} P_{a'} \right) \\
& + \sum_{a''} \Gamma^r_{a''a'} \left(\bar{f}_{r,a''a'} P_{a''} - f_{r,a''a'} P_{a'} \right) + R_{a'} \Bigg],
\end{aligned}
\tag{7.10}
$$

where the shorthand notations $f_{r,a'a} = f_r(E_{a'} - E_a - \mu_r)$ and $\bar{f}_{r,a'a} = 1 - f_r(E_{a'} - E_a - \mu_r)$ have been introduced. The tunnel rates $\Gamma^r_{aa'}$ for taking the DQD from state a' to a by tunneling to/from reservoir r are found from the Fermi golden rule [77]

$$
\Gamma^r_{aa'} = \frac{2\pi}{\hbar} \sum_{k\sigma} |T^{aa'}_{r\sigma}|^2 \delta(E_a - E_{a'} - E_k).
\tag{7.11}
$$

Here energy conservation is assumed, meaning that only first order processes are allowed. The term $R_{a'}$ accounts for relation within the DQD. It is given by

$$
R_{a'} = \sum_{a'_X} \left(\gamma_{a'_X a'} P_{a'_X} - \gamma_{a' a'_X} P_{a'} \right)
\tag{7.12}
$$

with the summation over all states $\{|a'_X\rangle\}$ that has the same number of electrons as $|a'\rangle$, and relaxation rates $\gamma_{a'a'_x}$,

$$
\gamma_{aa_X} = \begin{cases} T^{relax}_{aa_X}, & E_{a_X} < E_a \\ T^{relax}_{aa_X} \mathrm{e}^{-(E_{a_X} - E_a)/k_B T}, & E_{a_X} \geq E_a \end{cases}
\tag{7.13}
$$

where we have introduced the relaxation matrix T^{relax}. The relaxation matrix T^{relax} can be seen as an analogue to the transition matrix for the tunneling, and can in principle be defined through a relaxation Hamiltonian. However, in Papers III and IV T^{relax} is set to zero. Relaxation rates with constant relaxation times for all states have been used when analyzing the results (e.g., to see which conductance lines are from transitions starting from excited states).

To solve Eq. 7.9 we impose the boundary condition $\mathrm{tr}\{\rho_S\} = 1$, i.e., $\sum_a P_a = 1$. We then use the calculated probabilities to obtain the current in Section 7.4.

7.4 Current through the system

We wish to obtain the current through the small system, defined as the current $I_r(\tau)$ into (or out from) one the reservoirs:

$$
I_r(\tau) = \mathrm{tr}_{tot} \hat{I}_r \rho(\tau)
\tag{7.14}
$$

where the trace is taken over the full system. The current operator $\hat{I}_r$ is defined as

$$\hat{I}_r = -\frac{d}{d\tau} N_r = -i[H_T, N_r], \tag{7.15}$$

where the number operators in the reservoirs are given by $N_r = \sum_{\sigma k} c^{\dagger}_{r\sigma k} c_{r\sigma k}$.

Using tunnel rates Γ, we can then calculate the current in reservoir r from

$$I_r = \sum_{a,a'} \left[P_a \Gamma^r_{a'a} f_r(E_{a'} - E_a - \mu_r) - P_{a'} \Gamma^r_{aa'} \left(1 - f_r(E_a - E_{a'} - \mu_r)\right)\right] \tag{7.16}$$

which is the same as the total current through the system.

Part II

Main results of the research papers

Chapter 8

Results and discussion about Paper 1

In Paper 1 we calculated band structures for InAs/GaSb and GaSb/InAs core-shell nanowires, using the Kane model introduced in Chapter 2. We focused on thicker nanowires than those that have been studied before, since they are easier to grow. In addition to the band structure calculations, we use the obtained energies as input to the transport equations in Chapter 4. This is done to investigate if the interesting band features can be seen from electric and thermoelectric transport properties, that are studied as a function of the chemical potential.

The band structures show that both InAs/GaSb and GaSb/InAs core shell nanowires exhibit a large hybridization of electron like and hole like states, and that by changing the shell thickness of the core-shell nanowires, the system can be tuned from metallic to insulating. In addition, for the case of nanowires with GaSb cores and InAs shells, the band structures exhibit a closing, reopening and reclosing of the band gap when increasing the shell thickness. Our transport calculations, together with the calculated band structures, show that it is possible to find some of the most interesting band structure features by performing thermoelectric measurements of the Seebeck coefficient as a function of gate voltage.

8.1 Band structures

The band structures of the core-shell nanowires are affected by two geometric properties: the core radius and the shell thickness. In Paper 1 we have limited our analysis to core-shell nanowires with a core radius $R_C = 20$ nm. Apart from the fact that we are interested in nanowires that can be grown and characterized experimentally, and that other theoretical studies have focused mostly on thinner wires, the reason for this is that we want to keep

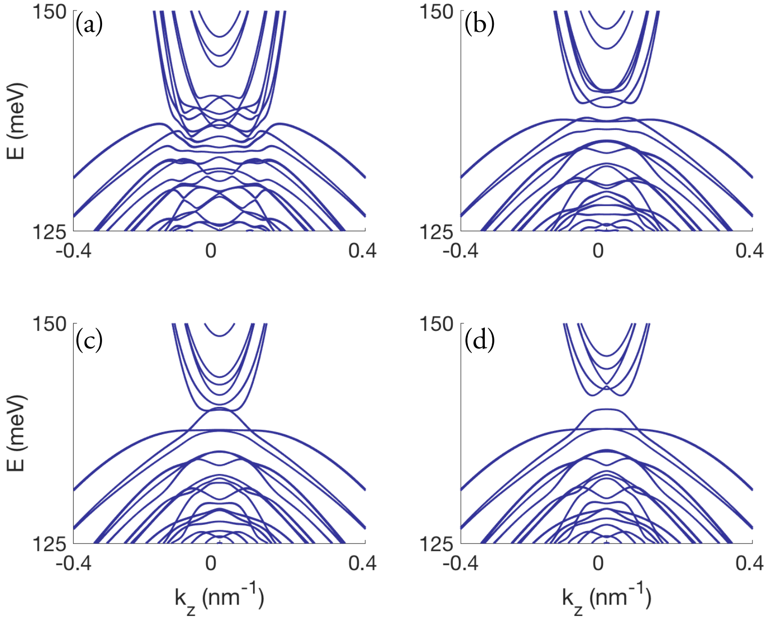

Figure 8.1: Calculated band structures for a nanowire with a GaSb core with radius $R_C = 20$ nm, and an InAs shell with shell thickness (a) $t_S = 8.5$ nm, (b) $t_S = 7.8$ nm, (c) $t_S = 7.62$ nm, and (d) $t_S = 7.5$ nm. Figure adapted from Paper 1.

some parameter fixed. Alternatively, one could keep the total radius (or even the shell thickness) fixed, and perform a similar analysis to the one presented in Paper 1.

In Paper 1 we study nanowires both with GaSb and InAs cores, with InAs and GaSb shells, respectively. In both cases we show that by decreasing the shell thickness, the band structure can be tuned from gapless to gapped, i.e., a band gap opens up. In Fig. 8.1 we show the resulting bands presented in Paper 1 for the case with a GaSb core and an InAs shell. In Fig. 8.1(a) the system is metallic, in Fig. 8.1(b) a hybridization gap opens up, which then closes when the shell thickness is decreased further in Fig. 8.1(c), and in Fig. 8.1(d) a gap reopens. For nanowires with InAs cores and GaSb shells the closing and reopening of the gap is not present (cf. Fig. 3 in Paper 1).

To be able to put our results in a larger context we also carry out calculations on thinner and thicker nanowires (smaller and larger core radii) than those presented in Paper 1. For thinner GaSb/InAs nanowires a larger hybridization gap is found (in agreement with e.g., Ref [35]); an example of this can be seen in the left panel Fig. 8.2. For InAs/GaSb core-shell nanowires we find that a hybridization gap indeed exists for nanowires with thinner core radii, consistent with Ref. [35]. An example of such a case is shown in the right panel of Fig. 8.2.

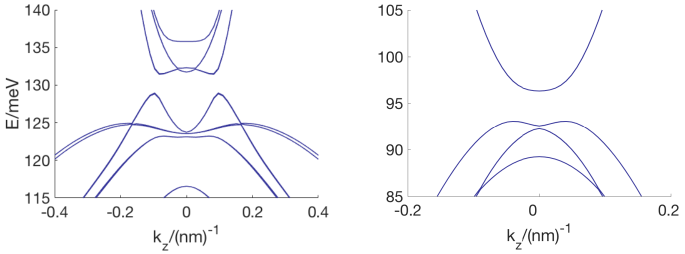

Figure 8.2: Left: Band structure for a GaSb/InAs core-shell nanowire with a core radius of $R_C = 10$ nm and shell thickness $t_s = 8.2$ nm. The hybridization gap is 2.5 meV. Right: Band structure for an InAs/GaSb core-shell nanowire with a core radius of $R_C = 9$ nm and shell thickness $t_s = 3.7$ nm. Parameters as in Paper I.

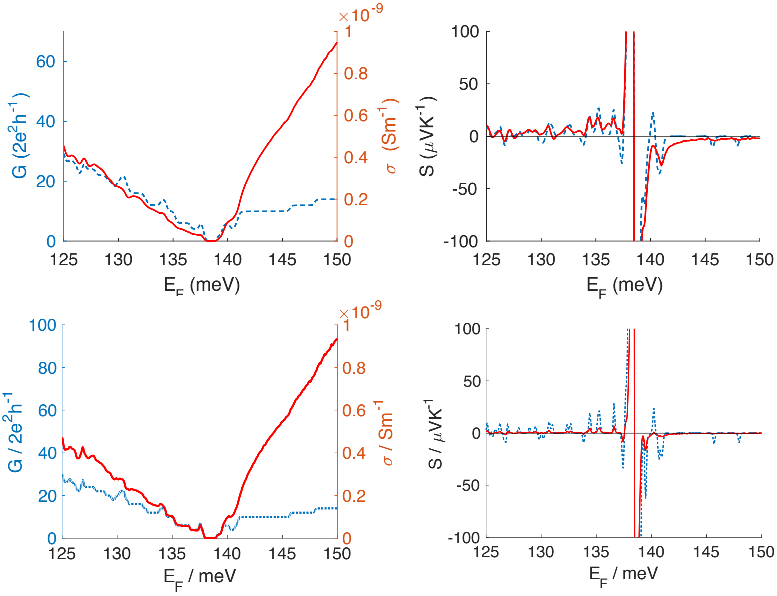

Figure 8.3: Left: Conductivities and conductances as a function of Fermi level (that can be controlled by a gate voltage) for a GaSb/InAs core-shell nanowire with $R_C = 20$ nm and $t_s = 7.8$ nm, corresponding to the band structure in Fig. 8.1 for $T = 1$ K (upper panel) and $T = 0.5$ K (lower panel). Right: The corresponding Seebeck coefficients. Figure adapted from Paper I.

8.2 Transport results

For both nanowire types, we used the band structures as input to calculate the conductivity, the conductance and the Seebeck coefficient in the diffusive and ballistic limits discussed in Chapter 4. The transport properties are calculated as a function of E_F, a quantity which can be controlled by a gate voltage. In both cases, we see that the conductivity (calculated in the diffusive limit) and the conductance (calculated in the ballistic limit) are similar (see upper panel of Fig. 8.3 for an example, or see Fig. 4 and Fig. 5 in Paper I for full results).

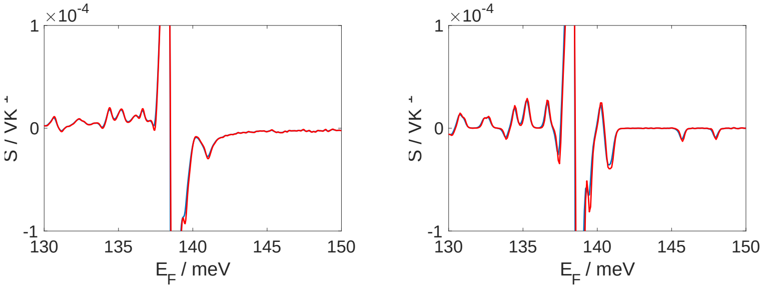

Figure 8.4: Left: The Seebeck coefficient as a function of Fermi level (that can be controlled by a gate voltage) calculated from the Mott formula (red) in the diffusive limit, and from Eqs. 4.16--4.17 for a GaSb/InAs core-shell nanowire with a core radius of $R_C = 20$ nm and shell thickness $t_s = 7.8$ nm. Right: The Seebeck coefficient calculated, for the same nanowire, from the Mott formula (red) in the ballistic limit, and from Eqs. 4.26--4.27. Parameters as in Paper I.

This is also the case for the calculated Seebeck coefficient in the two limits. We see that the conductivity and the conductance drops to zero when E_F lies in a band gap, hence we can distinguish between the gapped and the metallic systems from studying these quantities.

The Seebeck coefficient is more interesting to study, since its sign reveals the charge of the carriers dominating transport (negative for electrons and positive for holes). For the nanowires with GaSb core and InAs shell we see that this feature can be used to distinguish between the hybridization gap and the confinement gap in Fig. 8.1(b) and Fig. 8.1(d), respectively. For any gapped system the Seebeck coefficient as a function of E_F always has a large positive peak followed by a larger negative peak around the band gap. When we have a hybridization gap the Seebeck coefficient exhibits a negative peak, in energy just below the large positive peak, see right panel of Fig. 8.3. When there is no gap in the band structure, it is possible to see where the CB ends from the calculated Seebeck coefficient. This is signaled by the in energy lowest lying negative peak; see Fig. 5(f) in Paper I.

For the transport calculations we used a temperature of $T = 1$ K in Paper I. This temperature is low enough to resolve the interesting features, which are further enhanced at even lower temperatures (cf. Fig. 8.3). Another reason for not using a lower temperature is that the calculations of transport properties become significantly heavier.

In Fig. 8.4 we show an example of the Seebeck coefficient calculated from the Mott formula compared to the Seebeck coefficient calculated from Eqs. 4.16–4.17 and 4.26–4.27. We find that the Seebeck coefficient calculated from the Mott formula is very similar to the Seebeck coefficient calculated as in Chapter 4 in the two separate limits.

Chapter 9

Results and discussion about Paper II

We know from previous works that a two-dimensional QW of InAs/GaSb is a TI [11, 12]. It belongs to the symmetry class AII [40], which is characterized by the topological invariant $\mathbb{Z}_2$ in two dimensions, while being topologically trivial in one dimension, see Table 3.1 in Chapter 3. However, the quasi-one-dimensional nanowire is not a strictly one-dimensional system; one could consider the rotational symmetry around the growth axis and assign a k-index in the angular direction, even though such index can take only quantized values.

Exploiting the geometry of a core-core-shell nanowire, it is possible to look for topological properties in such a system. We consider a thought deformation from a two-dimensional sheet, that is "rolled-up" into a hollow core-shell-shell nanowire with a hole through its center axis, see Fig. 9.1. Such a core-shell-shell nanowire could in principle be grown with the techniques available today.

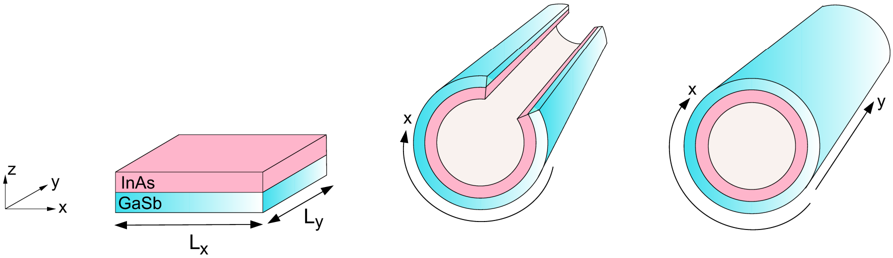

Figure 9.1: Left: The modeled quantum well (here depicted without AlSb barriers). The pure two-dimensional system corresponds to taking $L_x, L_y \to \infty$. Middle: The quantum well is thought of as being rolled-up. Right: The rolled-up system has periodic boundary conditions in x. It is similar to a core-shell nanowire, but has an empty core and two shells made of different materials.

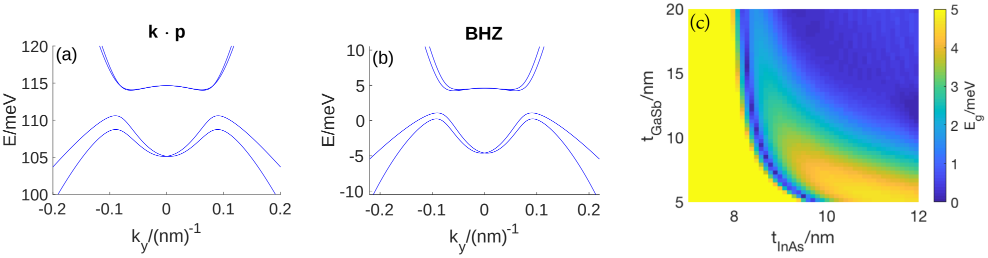

Figure 9.2: Band structures for a quantum well calculated using (a) the Kane model and (b) the BHZ model, shown for $k_x = 0$. The material layer thicknesses are given by $t_{InAs} = 11$ nm, $t_{GaSb} = 5$ nm, and $t_{AlSb} = 14$ nm. The parameters for the BHZ model can be found in Table 9.1. (c) Quantum well gap size plotted on a color scale, as a function of InAs and GaSb layer thicknesses. Here $k_x = 0$. The maximum value of the colormap is set to 5 meV, so that all values $E_g \geq 5$ meV will be the same color. Here AlSb barriers of $t_{AlSb} = 10$ nm are used. Parameters for the $\mathbf{k} \cdot \mathbf{p}$ calculations taken from Ref. [36].

In Paper II we study hollow InAs/GaSb core-shell-shell nanowires and make comparisons to InAs/GaSb QWs. The QW system is known for exhibiting the quantum spin hall effect in the topological phase. We show that the hybridization gap persists in the core-shell-shell system, and that if the nanowires are made finite in the growth direction the system hosts edge (or end) states at the ends of the wire. However, these end states are two-fold degenerate in each Kramers sector, and are not robust against disorder applied in the axial direction of the nanowire.

The band structures for the QWs and the core-shell-shell nanowires are calculated using the Kane model introduced in Chapter 2. A BHZ model, as presented in Chapter 3, is then used to reproduce the band structures, so that we find suitable parameters to use in further BHZ calculations. These calculations are used to study a finite nanowire system, and used together with a tight-binding scheme to study the effects of disorder, both in the radial and in the axial directions.

In this chapter we focus on the $\mathbf{k} \cdot \mathbf{p}$ calculations of the QWs and the core-shell-shell nanowires related to the results of Paper II. However, we make a few comparisons to results from BHZ calculations.

We start by modeling a QW with infinite extension in the x- and y-directions, so that L_x, $L_y \to \infty$ in Fig. 9.1. We discuss problems with spurious solutions in the $\mathbf{k} \cdot \mathbf{p}$ calculations for QWs, and how to avoid these. Then we turn to $\mathbf{k} \cdot \mathbf{p}$ calculations for a corresponding core-shell-shell nanowire, and show resulting band structures and wave functions. We end this chapter with a short discussion of the results from BHZ calculations of a finite core-shell-shell nanowire.

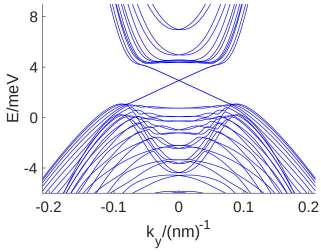

Figure 9.3: Band structure from the BHZ calculations of a QW with open boundary conditions in the y-direction showing the system in the topological regime, with mid-gap edge states. The parameters for the BHZ model can be found in Table 9.1.

9.1 InAs/GaAs quantum well

We start by analyzing $\mathbf{k} \cdot \mathbf{p}$ calculations of an InAs/GaSb QW. This system has been modeled before [36, 11, 28], so it is a good starting point for testing parameters and convergence. In our calculations in this chapter the commonly occurring parameter set, introduced in Ref. [36], for InAs/GaSb is used (referred to as the Halvorsen parameter set). The reason for using a different parameter set than in Paper 1, is that we want to be able to compare to the calculations of the QW band structures with those from other groups. However, in Paper 1 we also chose parameter set so that our calculations could be compared to results from previous works [35, 78].

In Fig. 9.2(a) we show band structures for a QW with InAs and GaSb sandwiched in between AlSb barriers. The thicknesses of the layers are given by $t_{InAs} = 11$ nm, $t_{GaSb} = 5$ nm and $t_{AlSb} = 14$ nm, chosen so that we are in a regime with a hybridization gap. This hybridization gap is here given by $E_g = 3.4$ meV. A version calculated with the BHZ model is shown in Fig. 9.2. Note that in both Figs. 9.2(a) and (b) the bands are degenerate only at $k_y = 0$, a degeneracy that is split for all other values of k_y due to the SIA.

If we do not include AlSb barriers in the $\mathbf{k} \cdot \mathbf{p}$ calculations for the QW the resulting band structures show spurious solution. This will be discussed in detail in the next section.

In Fig. 9.2(c) we have calculated the size of the effective band gap for varying thicknesses of the InAs and GaSb layers in the QW. The effective gap size is taken as the energy difference of the lowest point in energy of the bands above the gap, and the highest point in energy for the bands below the gap. These points are in general taken for different values of k_y. Since the band gap closing and reopening can signal a topological phase transition, this plot can be used to find a QW in the desired topological regime.

Using the BHZ model together with a tight-binding scheme, we have calculated the energy dispersion for a QW structure finite in the x direction. Figure 9.3 shows the band structure for such a finite-in-x QW structure in the topological regime, with mid-gap edge states.

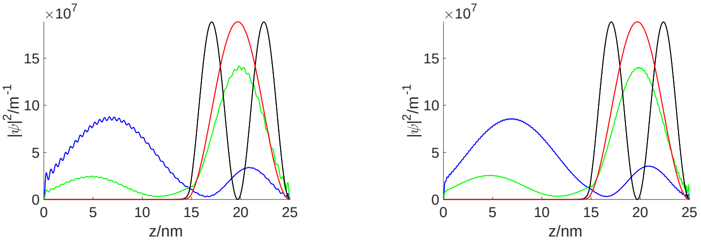

Figure 9.4: Probability densities from the $\mathbf{k}\cdot\mathbf{p}$ simulations of the QW with layered InAs ($t_{InAs} = 15$ nm) and GaSb ($t_{GaSb} = 10$ nm). Here the parameters are taken from Ref. [8], but with adjusted E_P and A according to Ref. [31] (like in Paper I). The number of basis functions are given by $J = 100$ (left) and $J = 200$ (right).

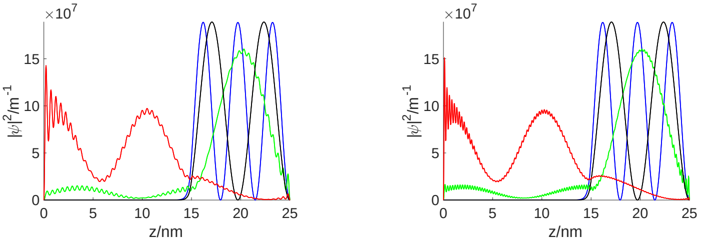

Figure 9.5: Probability densities from the $\mathbf{k}\cdot\mathbf{p}$ simulations of the QW with layered InAs ($t_{InAs} = 15$ nm) and GaSb ($t_{GaSb} = 10$ nm). The parameters are taken from Ref. [36]. The number of basis functions are given by $J = 100$ (left) and $J = 200$ (right).

These edge states are robust against disorder (not shown), a known results from works of other groups [11, 12]. For this system the disorder causes a shift of all edge state energies by some amount, while the spacing between the levels remain constant. This signals that the edge modes are topologically protected.

9.1.1 Quantum well with and without AlSb barriers

In the $\mathbf{k}\cdot\mathbf{p}$ calculations we consider a QW of layered InAs and GaSb. Without any additional barrier material around the semiconductors, the calculated wave functions oscillate in an unphysical manner, see Figs. 9.4 and 9.5. The reason that we consider those oscillations unphysical is that the ground state wave function oscillates very rapidly. For the parameter set used in Paper I, oscillations die off for around $J > 200$ basis functions. This is a significantly higher number of basis functions than was needed for convergence of the calculations for core-shell nanowires in Paper I, where (depending on size) around $20 - 25$ functions were needed in the radial and the angular direction each.

There is an additional erroneous feature at the boundaries of the sample, which is much more pronounced when using the Halvorsen parameter set (cf. Fig. 9.5). The wave functions do not seem to converge towards a physically reasonable result: they do not tend to zero close to boundaries. There is also a kink at the material interface, which is not present when

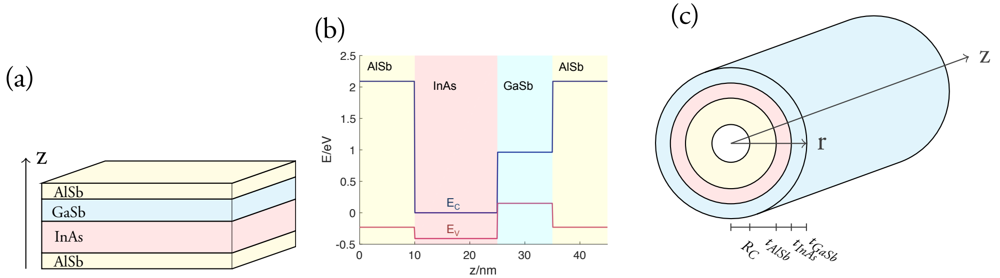

Figure 9.6: (a) The InAs/GaSb quantum well with AlSb barriers. (b) Band diagram of bulk band edges for InAs, GaSb and AlSb. (c) The core-shell-shell nanowire we solve for in Paper II.

using the other parameter set; however, this kink can also be seen in Ref. [36]. For both parameter sets used in the simulations, the oscillation frequency increases with an increased number of basis functions. However, while the amplitude decreases and tends to zero (so that we reach convergence) for the parameter set used in Paper I, it is not significantly reduced for the wave functions calculated using the Halvorsen parameter set. Nevertheless, for calculations of the core-shell-shell nanowires, more than 200 basis functions in the radial direction is in practice impossible, since we have an additional, angular, direction to consider as well.[1] In total, the matrix size we need to solve for for the nanowires is $8LN \times 8LN$, where L is the number of basis functions in the radial direction, and N is the number of basis functions in the angular direction (cf. Eq. 2.31). For the radial part we need many more basis functions than were needed for the simulations of the core-shell wires, in practice around $L = 70$. One aspect of why we need more radial basis functions for the (hollow) core-shell-shell nanowires than for the solid core-shell nanowires is that we use a different basis to expand in. It is not far-fetched to think that cylindrical Bessel functions are better for describing the states in a cylindrical wire, than the basis we use for the core-shell-shell calculations is for describing states in a shell; the basis we use for the core-shell-shell calculations is an approximation of the Bessel functions valid for $r \to \infty$. We need a few more angular basis functions for the core-shell-shell system than for the core-shell nanowires. There could be a difference in angular behavior for when we have a shell (origin not contained) and for when we have a wire (origin contained), but the difference can also be caused by the larger circumference of the core-shell-shell nanowires.

Another interesting feature in the calculations that yields spurious solutions, is that we see "alternating convergence" with respect to odd or even number of basis functions used, i.e., that the results seem to oscillate between two distinct solutions while slowly converging. We do not understand this phenomenon, but advice that it should be tested for in $\mathbf{k} \cdot \mathbf{p}$ calculations.

---

[1] The radial direction is where we consider the different material layers for the nanowires, similar to the growth direction (z in Fig. 9.1) for the QWs.

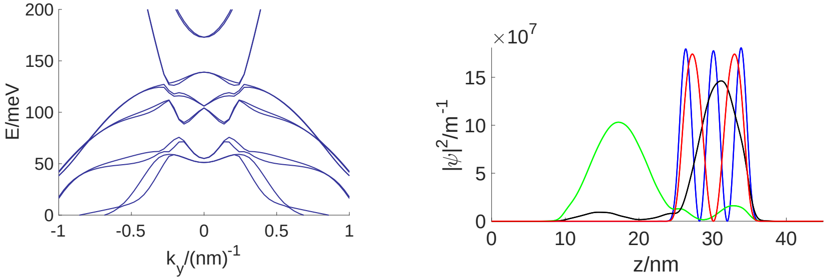

Figure 9.7: Left: Band structure of the InAs/GaSb QW with AlSb barriers on both sides. The thicknesses of the material layers are given by $t_{InAs} = 15$ nm, $t_{GaSb} = 10$ nm, and $t_{AlSb} = 10$ nm. The parameters are taken from Ref. [36] and the number of basis functions is $J = 40$. Right: Corresponding probability densities for lowest lying states at $k_y = 0$.

To overcome the convergence problems for the QWs, and to be able to compare our simulations to previous works [11, 34, 28, 36], we add AlSb barriers to the QWs, see Fig. 9.6(a). As shown in the band diagram in Fig. 9.6(b), AlSb is an insulator, with a much larger bulk band gap than both InAs and GaSb. In Fig. 9.7, we show that this solves the problem with erroneously oscillating wave functions. Our calculated band structures and probability densities are also in good agreement with the previous results by other groups [11, 34, 28, 36]. When using AlSb barriers, we obtain similar results from both parameters sets.

Using 10 nm AlSb barriers on each side, we need $J = 40$ basis functions to converge our simulations (using the Halvorsen parameter set). This is indeed a higher number of basis functions than needed in the radial direction for the core-shell nanowires. However, even though we do not see (or expect) significant parts of the wave functions to leak out into the AlSb barriers (for the states around the gap), the $\mathbf{k} \cdot \mathbf{p}$ solver still has to take into account four different material regions. With two of these regions being more or less impenetrable, it is not surprising that this would require a larger basis.

For the core-shell-shell nanowires we have seen that one inner AlSb barrier, inside the inner (InAs) shell, is enough to obtain well-behaved wave functions (not shown). Such an inner AlSb barrier is used for the results in the next section. This is also how we imagine that a hollow InAs/GaSb core-shell-shell nanowire would be grown; with a solid AlSb core. However, due to the basis we use, we only include an inner AlSb shell, and keep the inner core-part empty. In Fig. 9.6(c) we show such a hollow core-shell-shell nanowire.

9.2 InAs/GaSb core-shell-shell nanowire

In this section we calculate band structures and wave functions for a core-shell-shell nanowire, like the one shown in Fig. 9.6(c). We have chosen to keep the total radius fixed to $R =$

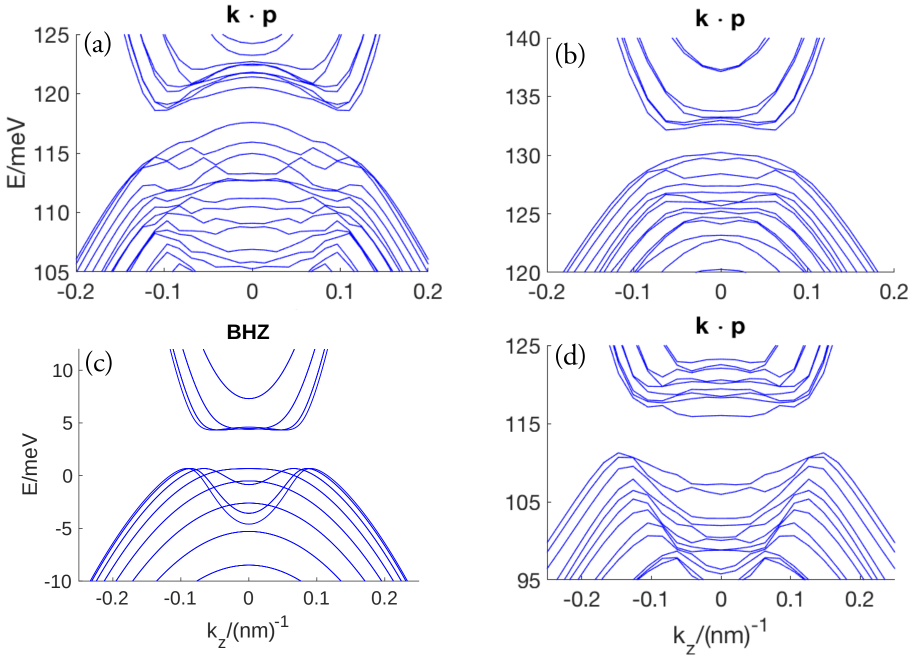

Figure 9.8: Band structures for a core-shell-shell nanowire, calculated using the Kane model, with $R_c = 10$ nm, $t_{AlSb} = 14$ nm (a) $t_{InAs} = 9.5$ nm and $t_{GaSb} = 6.5$ nm, and (b) $t_{InAs} = 11$ nm and $t_{GaSb} = 5$ nm. (c) Band structure calculated using the BHZ model with parameters from Table 9.1 and $R_{BHZ} = 32$ nm. (d) Band structure for a core-shell-shell nanowire, calculated using the Kane model, with $R_C = 10$ nm, $t_{GaSb} = 5$ nm, $t_{InAs} = 11$ nm and $t_{AlSb} = 5$ nm. Parameters for the $\mathbf{k} \cdot \mathbf{p}$ calculations taken from Ref. [36].

40 nm in all $\mathbf{k} \cdot \mathbf{p}$ calculations, an experimentally feasible value, but also chosen so that the length (thickness) scales are comparable in the QW and the nanowire calculations. However, we have chosen not to include an outer AlSb shell, since it is an advantage to not have an extra material shell in an actual growth process. Furthermore, it is not needed for convergence, but merely adds to the computational cost. From a theoretical point of view, the inner AlSb layer could be exchanged for another insulator material (such as vacuum), without altering the overall physical properties of the system to any larger extent.

In Fig. 9.8 we show band structures for the core-shell-shell nanowire. In Fig. 9.8(a) the thicknesses for the InAs and GaSb material layers are given by $t_{InAs} = 11$ nm and $t_{GaSb} = 5$ nm, the same thicknesses as for the QW in Fig. 9.2. The empty core radius is given by $R_C = 10$ nm and the AlSb shell thickness is given by $t_{AlSb} = 14$ nm. We see that the energy gap for the core-shell-shell nanowire becomes much smaller, $E_g = 1.0$ meV, compared to that for the QW of $E_g = 3.4$ meV. The main reason for this, is the additional confinement in the nanowire. Furthermore, the band structure shows many subbands, both from radial and angular confinement. The subbands from the angular confinement are much closer in energy to each other than the subbands from radial confinement. Comparing the length scales, we see that this is reasonable: the angular confinement is related to the circumference of the wire, $2\pi R \approx 250$ nm, while the radial confinement depends on the shell thickness, $t \approx 5 - 16$ nm. In Fig. 9.8(b) we show the band structure for a core-shell-shell nanowire where the material thicknesses are adjusted to $t_{InAs} = 9.5$ nm and $t_{GaSb} = 6.5$ nm. In this case, the hybridization gap is larger (compared to Fig. 9.8a), $E_g = 1.9$ meV. Here we have kept the AlSb shell thickness fixed at $t_{AlSb} = 14$ nm. However, adjusting the AlSb shell thickness, the empty core and/or the total nanowire radius, could likely yield a larger hybridization gap.

In Fig. 9.8(c) we show the band structure for a core-shell-shell nanowire, reproduced by the BHZ model. The radius for the "rolled-up" QW is $R = 32$ nm, and the parameters from the fitting of the QW band structures are used (cf. Table 9.1), except for R_0 and T_0 that are set to zero, to account for the fact that structural inversion symmetry is present in the core-shell-shell nanowire.

In theory it is possible to create core-shell-shell structures which have a much larger hybridization gap. Figure 9.8(d) shows the band structure of such a core-shell-shell nanowire with a somewhat different material distribution. Here a vacuum core (of $R_C = 10$ nm) is covered by an inner GaSb shell ($t_{GaSb} = 5$ nm), an InAs shell ($t_{InAs} = 11$ nm) and an outer AlSb barrier shell ($t_{AlSb} = 5$ nm). Note that the thicknesses of the InAs and GaSb shells are the same as in Fig. 9.8(a), but the order of the layers have been changed, and the GaSb and InAs shells are closer to the core, since the inner AlSb barrier is moved to the outermost part of the structure. This structure shows a hybridization gap of $E_g = 4.6$ meV, larger than that for the corresponding QW. However, this structure might not be realistic to grow, due to the lack of an inner AlSb shell (that could be extended to cover the full core). Nevertheless, one could consider growing an AlSb core, covered by an inner GaSb shell and an outer InAs shell, but without the outermost AlSb shell. This structure is however hard to model with our $\mathbf{k} \cdot \mathbf{p}$ solver since it yields spurious solutions. We have found that this is because we in these structures need to include an AlSb barrier next to the InAs layer. An alternative is to use both inner and outer AlSb barriers in the model. This would solve the problem with spurious solutions, but would instead introduce a problem with very large matrices, due to the increased number of radial basis functions that would be needed to describe four different material regions.

In contrast to the bands for the QWs, the bands for the core-shell-shell nanowires are doubly degenerate everywhere. This is because the nanowires obeys structural inversion symmetry, while for the QWs this symmetry is broken in the z direction. Together with the time-reversal symmetry this results in doubly degenerate bands for all k_z. This is because while time-reversal causes Kramers degeneracy, $E_+(k_z) = E_-(-k_z)$, for the Kramers partners $E_\pm$, inversion symmetry causes an additional degeneracy $E_+(k_z) = E_+(-k_z)$, so that in total we must have $E_+(k_z) = E_-(k_z)$ [7].

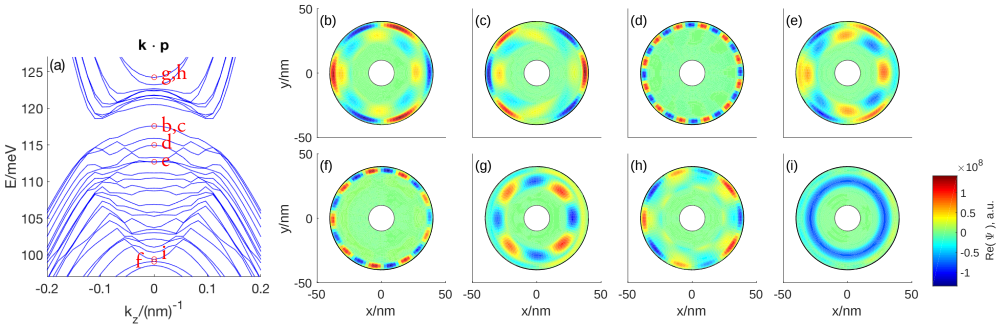

Figure 9.9: (a) The same band structure as in Fig. 9.8(b), but plotted with a larger energy span. (b) Real parts of the wave functions for $k_z = 0$, corresponding to bands marked b-i in (a). Parameters for the $\mathbf{k} \cdot \mathbf{p}$ calculations taken from Ref. [36].

To simulate a nanowire of finite length, we take open boundary conditions in the y-direction in the BHZ model. The QW edge states gap out in this system, but leave quantized bound states localized at the nanowire ends. These end states are doubly degenerate for each Kramers pair, so that they are four fold degenerate in total. The degenerate pairs can be chosen to be localized at opposite edges in the y-direction.

9.2.1 Wave functions of the core-shell-shell nanowires

In Fig. 9.9(b) – (i) we show the real part of the wave functions corresponding to the bands in Fig. 9.9(a), for $k_z = 0$. This is the same band structure as in Fig. 9.8(a), but for a larger energy range, and with states indicated.

First we study some of the wave functions corresponding to VB like bands, marked b-f in Fig. 9.9(a), then we address wave functions corresponding to some of the CB like bands, marked g-i in Fig. 9.9(a). However, in most of the states, the wave functions have weights in both the InAs and the GaSb shells.

In the states shown in Fig. 9.9(b)-(d), corresponding to marks b-d in Fig. 9.9(a), we see that the wave functions have their weight in the outer (GaSb) shell. This comes as no surprise - the corresponding bands show VB-like curvatures. In Fig. 9.9(d), the wave functions has a much higher angular momentum than the states in b and c, and the corresponding band has a visibly larger curvature. In Fig. 9.9(e) we show the wave function corresponding to one of the bands marked e in Fig. 9.9(a). These two bands are *almost* degenerate, and their curvature close to $k_z = 0$ cannot be deduced by looking at the bands. These states have large weights in both shells, and have different angular momenta in the two different material regions.

In Fig. 9.9(f) the state corresponding to the highest in energy, non-hybridizing state below the gap is shown (mark f in Fig. 9.9a). It is confined to the GaSb shell, and we see that the state has a large angular momentum, an expected feature this far from the band gap.

In Fig. 9.9(g) and (h), we continue with the CB like states above the band gap. Here we show the two lowest in energy, seemingly non-hybridizing states, above the band gap (corresponding to marks g and h in Fig. 9.9a). While the state in Fig. 9.9(g) has most of its weight in the InAs shell, the state in Fig. 9.9(h) has more weight in the GaSb shell. This shows that looking at the curvature of the bands can sometimes be deceiving! However, this close to the hybridization gap, it is hard to predict the strength of hybridization for individual energy bands. A change of the curvature that is not seen on this scale can occur close to $k_z = 0$.

In Fig. 9.9(i) we show the wave function for the lowest lying CB-like state (mark i in Fig. 9.9a). The state has almost all of its weight in the InAs shell, and no angular momentum. That a state, with no mixing of the CB- and VB-like states, is seen this far in energy from the band gap strengthens that the gap we see is caused by hybridization, and not by confinement. One interesting feature, seen in several of the states in Fig. 9.9, is that the angular momentum is different in the InAs and GaSb shells (this is easiest to see in Fig. 9.9e). This shows that mixing of states with different angular momenta is present in the nanowire.

We stress that some arbitrary symmetry breaking is seen in some of the plots, due to the fact that all the states doubly degenerate, and only one of the Kramers partners is shown. The total wave function for the degenerate states, $|\Psi_{tot}|^2 = \sum_i = 1, 2(|\psi_1|^2 + |\psi_2|^2)$ (i runs over the two Kramers degenerate states) must obey a higher symmetry. However, they do not have to be rotationally symmetric in the plane (in the $\mathbf{k} \cdot \mathbf{p}$ model) since the underlying crystal structure can impose visible peaks in the angular direction of the wave function.

9.3 Core-shell-shell nanowires with disorder

To analyze the character of the end states we have found for the core-shell-shell nanowire, we introduce disorder to our system by adding a disorder term $H_{dis} = V(x, y)\,\mathbb{1}_{4\times 4}$ to the BHZ Hamiltonian. The introduced disorder respects time-reversal symmetry, and has a random uniform distribution with amplitude V_{dis} and is applied either in the axial (V_{dis}^{ax}) or in the radial direction (V_{dis}^{rad}).

Figure 9.10 shows the energies of the system for applied disorder. In Fig. 9.10(a), axial disorder is applied. Between the bulk states at the top and bottom of the figure, we see that the mid-gap end states split linearly with increasing disorder strength. Figure 9.10(b) shows the probability densities for the states marked in in Fig. 9.10(a). The four fold-degenerate

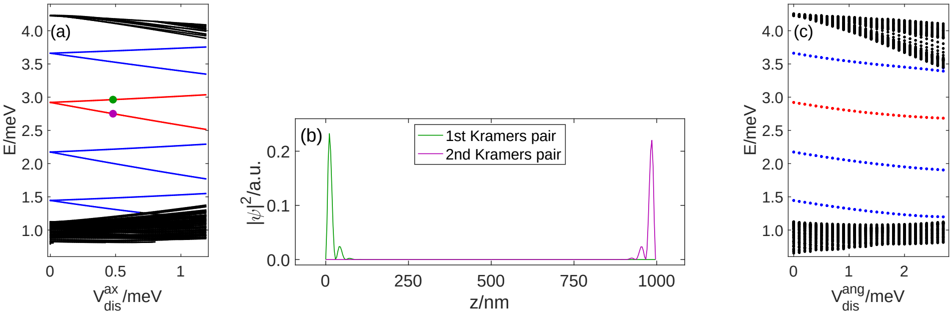

Figure 9.10: Energy spectrum as a function of disorder strength for the quantum well with periodic boundary conditions in x and open boundary conditions in y. Only energies in the band gap are displayed. The degeneracy of these end states split with increasing disorder strength. The parameters for the BHZ model can be found in Table 9.1.

Table 9.1: Parameters used in the BHZ model throughout this chapter and in Paper II (if nothing else is stated). Parameters not listed are set to zero.

Parameters and values

A/(meV·nm)	B/(meV·nm^2)	D/(meV·nm^2)	M/meV	R_0/(meV·nm)	T_0/(meV·nm^3)
30.5	-710	-450	-4.6	10	300

states (for $V_{dis}^{ax} = 0$) are split into Kramers pairs, residing at opposite ends of the nanowire, even for increasing disorder strength.

In Fig. 9.10(c), we show the energy spectrum under applied disorder in the radial direction. For this type of disorder the ends states do not split, but show only a slight shift in energy. However, at large disorder strengths (large V_{dis}^{rad}) the bulk states are closer in energy, so that the band gap becomes smaller.

Since disorder can split the degeneracy of the end states, these states are not robust against disorder, which confirms that that they are not topologically protected.

Chapter 10

Results and discussion about Papers III and IV

Papers III and IV treat DQDs coupled in parallel to source and drain contacts, subject to a magnetic field. The DQD system consists of an epitaxially confined single QD in a zincblende InAs nanowire, between wurtzite segments that act as walls. Positively charged side gates applied to the QD creates a double-well potential, creating two electron pockets at the sides of the disc shaped QD, so that we effectively have a DQD. Data from tunneling spectroscopy experiments are analyzed using a theoretical model including a few-body Hamiltonian with SOC and B-field, together with a master equation method for the transport.

Paper III is mainly focused on tuning the interdot coupling to control the B-field dependent singlet- triplet ground state transition in the regime where one electron populates each QD. Around the ground state transition the singlet and triplet states anticross.

In Paper IV the same system is studied, but with a level detuning between the single-electron energy levels on each QD. In this paper there are three main focuses: the transition $(1,0)-(1,1)-(2,0)$, the evolution of the $T(1,1)$ states under a magnetic field, and the hybridization of the $(1,1)$ and $(2,0)$ states.

In Paper III we model the single electron energy levels to be degenerate, while in Paper IV a level detuning is introduced. All parameters in the Hamiltonian in equation 6.1 are chosen carefully to reproduce the experimental transport data. In particular, V_x and U_{12} are chosen to yield the correct J, while α is taken so as to give us the correct size of the anticrossing minimum Δ^*_{ST} of the $S(1,1)$ and $T(1,1)$ states. The value for $|g^*|$ is taken so that this minimum occurs at the "correct" value of the B-field. The value of t is extracted from the splitting between the anti-bonding (AB) and bonding (B) one-electron states, $t = \frac{E_{AB}-E_{A}}{2}$.

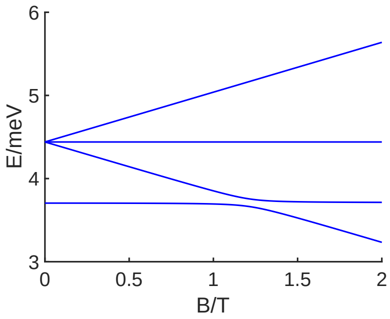

Figure 10.1: Evolution of the singlet and triplet (1,1) states under an external magnetic field, calculation. Data set A from Table 10.1 is used.

We assume t to be independent of small changes in the gate voltages, so that we use the same t when the DQD is doubly occupied.

In Paper III we additionally tune t by sweeping a back gate voltage (while keeping the direction of $V_{L,R}$ fix). This can be viewed in a simple wave function picture, where the wave functions will overlap more when t is lowered. In Paper IV we detune the one-electron energy levels in the QDs, using V_L and V_R, and study the $(2,0) \rightarrow (1,1)$ transition. In addition to the already mentioned parameter sweeps in Papers III and IV, an external B-field is varied to study how the spin states evolve.

The focus of Paper III lies on the one- to two-electron transition including the $S(1,1)$ and $T(1,1)$, the singlet and triplet states with one electron in each QD. The singlet and triplet states with both electrons in the same QD (e.g., $S(2,0)$) are high in energy, due to the large charging energy for having two electrons on the same QD. They can thus be omitted from the analysis when the single electron levels align in the QDs (these states are not seen in the experimental data for Paper III). However, in Paper IV the DQD is studied under a level detuning between the QDs, for a relatively weak coupling t. The level detuning results in a lower relative energy for the $(2,0)$ states, compared to that for the $(1,1)$ states.

10.1 Anti-crossing between the $S(1,1)$ and $T_+(1,1)$ states

In Paper III we study the B-field evolution of the 2e ground states, transitioning from $S(1,1)$ to $T_+(1,1)$ (the lowest lying triplet state). The SOC couples the singlet and triplet states, so that a we see an anticrossing of these states, see Fig. 10.1. Figure 10.2 shows experimental data for the corresponding anticrossing. We find that the magnitude of the anticrossing is $\Delta^*_{ST} = 230$ eV when the tunnel coupling is given by $t = 2.3$ meV (data set B in Table 10.1). Where this happens in B depends on t; when t (and hence J) increases, the value of B where the ground state transition takes place also increases (cf. Fig. 10.1). In

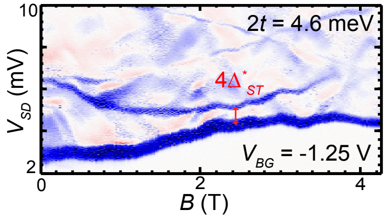

Figure 10.2: Experimental transport data showing the evolution of the singlet and triplet (1,1) states under an external magnetic field. Figure adapted from Paper III.

Table 10.1: Values for the parameters used in the calculations. The electron temperature used is $T = 46$ mK.

Data set	$2t/\text{meV}$	V_x/meV	U_{11}/meV	U_{22}/meV	U_{12}/meV	α	$\lvert g^*\rvert$	t_2/t_1	t_S/t_D
A	3.12	0.0548	14.4	16.4	4.49	0.08	10.37	25	1
B	4.6	0.258	9.6	12.9	4.46	0.08	-	25	1
C	0.28	0	14.8	13.3	2.58	0.6	8.9	1	2

general Δ^*_{ST} has a linear t-dependence. We can estimate the spin-orbit length based on this, $l_{SO} \sim \frac{t}{t_{SO}} l_{dot} \approx 400$ nm, where $l_{dot} = 34$ nm is taken as the radius of the disc-shaped QD (i.e., the radius of the nanowire).

Figure 10.3 shows charge stability diagrams, resulting from measurements and from calculations, for the case when $B = 1.2$ T. At this value of the B-field the $S(1,1)$ and $T(1,1)_+$ anticross. The magnitude of the anticrossing is here $2\Delta^*_{ST}$ by definition (under the assumption that this is where the ground state transition happens , i.e., where $S(1,1)$ and $T(1,1)_+$ would have crossed without SOC present). Note that all possible transition lines are visible in the experimental data except two: $B_\downarrow - T_0$ and $AB_\downarrow - T_0$ – these two lines both start from an excited states and end in an excited state. However, these lines can be seen in the calculated transport (there is no relaxation of excited states included in these calculations).

10.2 Anticrossing between the $S(2,0)$ and the $T(1,1)$ states

In Paper IV we study the $(2,0) \to (1,1)$ transition under level detuning Δ of the one-electron states in each QDs, subject to an external magnetic field. We see hybridization of $(2,0)$ and $(1,1)$ states, resulting in anticrossings. In the experimental data for Paper IV all three triplet states and the singlet states are seen, including the excited $T(1,1)$ states. When populating the DQD with up to three electrons, the DQD shows a symmetry between the one- to two-electron and two- to three-electron transitions, as expected due to Kramers degeneracy in the single-electron levels. With one level on each QD, three electrons correspond to one hole, meaning that three electrons is the hole equivalent to the one-electron states. However, if Kramers degeneracy is broken, the corresponding electron and hole states will not have the same energy: for example, the state $|2,\uparrow\rangle_e$ (with two electrons in

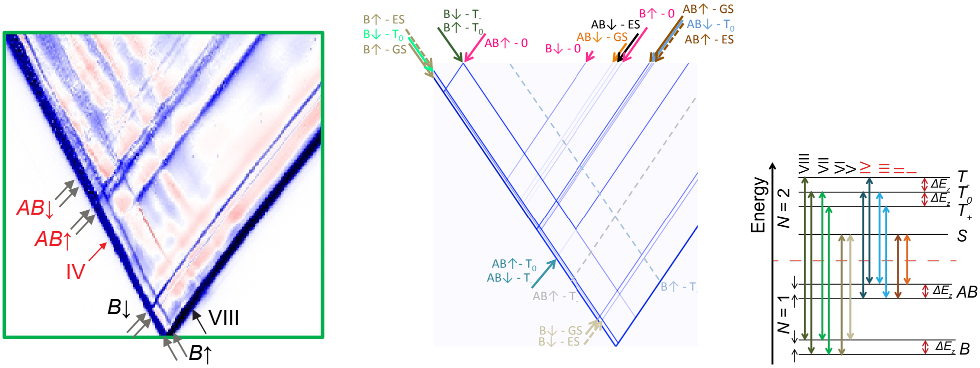

Figure 10.3: Left: Experimental transport data for $B = 1.2$ T. Middle: Calculated transport corresponding to the measurement data. Data set A from Table 10.1 is used. All transitions are indicated. Right: Allowed transitions between one- and two-electron states. Figures adapted from Paper III.

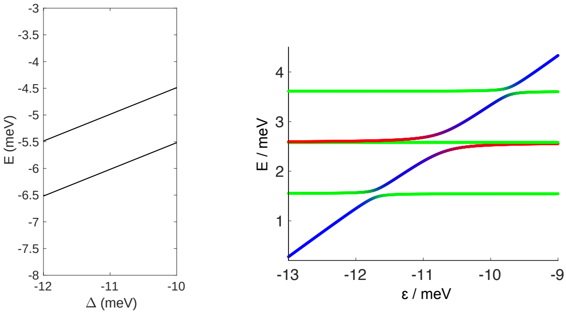

Figure 10.4: Evolution of the DQD states under level detuning (calculated). Data set C from Table 10.1 is used. Left: One-electron states Right: Two-electron states. The contribution to the eigenstates are color-coded using red, blue and green for the $S(1,1)$, $S(2,0)$ and $T(1,1)$ states, respectively. Figures adapted from Paper IV.

the left QD and one electron in the right QD) will not correspond to the hole state $|0, \downarrow\rangle_h$ if the single electron spin states are split.

Figure 10.4 shows how the energy levels evolve with Δ, for $B = 2$ T. In the right panel the coloring of the lines shows the contribution of the $S(1,1)$, $S(2,0)$ and $T(1,1)$ states, to the total wave function Ψ, i.e., the coefficient p_i for the basis states ψ_i: $\Psi = \sum_i p_i \psi_i$. The $S(2,0)$ state, where the two electrons reside in one of the QDs, exhibits a slope, while the spatially symmetrical states do not. This is because we do not change the overall energy by the detuning, but only the relative one-electron QD levels.

Figure 10.5 shows experimental data and calculated differential conductance as a function of detuning, for both corresponding to the state evolution in Fig. 10.4, and we can again see

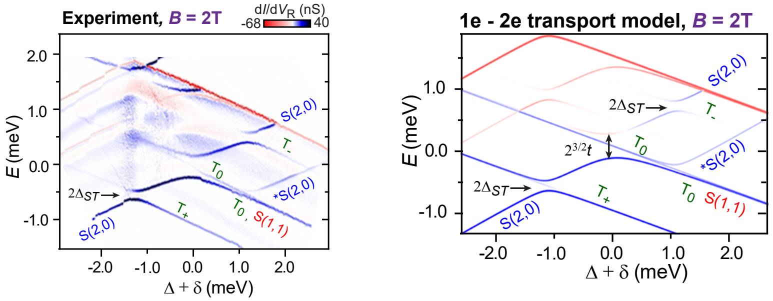

Figure 10.5: Differential conductance for the double quantum dot under level detuning. Left: Data from measurements. Right: Corresponding calculated transport. Data set C from Table 10.1 is used. In the calculations the three-electron states were omitted. The parameter δ is chosen so that $\Delta + \delta = 0$ at the anticrossing. Figures adapted from Paper IV.

how the states evolve with Δ. In the vicinity of the hybridization of the $S(2,0)$ and $T(1,1)$ states spin is mixed. We note that Fig. 10.4 looks like a rotated version of the two-electron evolution in Fig. 10.5; this is because the quantities on the x-axes differ: in Fig. 10.4 the x-axis is given by the one-electron energy ϵ_1 , while in Fig. 10.5 the x-axis shows the detuning between the two one-electron levels ϵ_1 and ϵ_2.

We can see some lines from transport starting from excited one-electron states. An example of a line originating from a process starting from a ground state can be seen in the lower panel of Fig. 10.5, as a line going through the $S(2,0) - T_+(1,1)$ anticrossing. However, while some lines overlap, it is expected that transport line contributions corresponding to transport starting from one-electron ground states will dominate, since, it is in general much more likely for a ground state to be populated. A reason for the visible line in the calculated transport is that relaxation is not taken into account. This means that in reality the weak lines from transport processes starting from an excited state should be even weaker. By setting a constant relaxation time for all states in the DQD, we can investigate how relaxation affects the transport, and find that the above mentioned excited states do not contribute to the transport. Avoided crossings between $S(2,0)$ and $T(1,1)$ and a transition between $D(\uparrow,0)$ and $T_-(1,1)$, normally forbidden, can be seen close to the hybridization of the $S(2,0)$ and $T(1,1)$ states, since spin-mixing caused by SOC allows for it.

10.3 Comparison between the two anticrossings

The states $S(2,0)$ and $T(1,1)$ are related by a spin-flipping tunneling process only, while the states $S(1,1)$ and $T(1,1)$ mixes through second order tunneling. To go from $S(1,1)$ to $T(1,1)$ an electron first needs to tunnel (to the intermediate $S(2,0)$ state), and then tunnel back while flipping its spin. This is since no local spin flipping process is allowed here, meaning that $S(1,1)$ and $T(1,1)$ cannot couple in first order in t.

In Paper III the $S(1,1)$ and $T(1,1)$ couples, resulting in an anticrossing of $2\Delta_{ST}^{*} \sim t t_{SO}/U = \alpha t^2/U$ (where U is a function of U_{11}, U_{22} and U_{12}) . In Paper IV we saw that there is instead mixing between $S(2,0)$ and $S(1,1)$, and between $S(2,0)$ and $T(1,1)$. The anticrossing $S(2,0) - S(1,1)$ has a gap size of $\Delta E = 2\sqrt{2}t$, while between $S(2,0)$ and $T(1,1)$ the gap is $2\Delta_{ST}$, where $\Delta_{ST} \sim t_{SO} = \alpha t$. However, the numerical value of Δ_{ST} is much smaller in Paper IV compared to Δ_{ST}^{*} in Paper III, due to that t is much smaller in Paper IV ($t = 170$ eV in Fig. 10.5). Furthermore, in the two papers a different SOC parameter α is needed for the measurement data sets in the two papers, corresponding to two different cooldowns of the DQD system. The different cooldowns might cause a change in the SOC vector from changes in the QD shape and the internal electric field, meaning that the system is subject to more differences than just a change of t.

Chapter 11

Outlook

In this thesis we have discussed two types of nanostructures based on InAs nanowires: InAs/GaSb core-shell(-shell) nanowires, and parallel DQDs made from single QDs, epitaxially defined in InAs nanowires.

It would be interesting to investigate how the end states in the core-shell-shell nanowires are affected by changing the empty core radius; for a large radius (tending to infinity), the system would effectively be a QW. In addition, it would be good to study the full parameter space of InAs and GaSb shell thicknesses, to see where the hybridization gap opens and closes, and where it is largest. To bridge Paper I and Paper II, one could imagine a study of the gap size and the end states when filling up the empty core. However, for the InAs/GaSb core-shell and core-shell-shell nanowires, one interesting bigger step would be to induce superconductivity in the system. The system would then be in the topological class DIII, known to be able to host Majorana bound states at the ends of the system in one dimension. Majorana bound states are one of the most promising candidates for qubits, due to their topological robustness and non-local properties - they are suggested to ideally being able to perform quantum computations without errors [79].

The DQDs have been further investigated in the group of Claes Thelander. In transport measurements, both spin and orbital Kondo effects are seen [80], and by tuning the parameters of the DQD, ring-like QDs are formed [81]. For further studies of the DQDs, like for the core-shell-shell nanowires, introducing superconductivity is suggested as an interesting direction. As a first step measurements using superconducting contacts are being performed.

In the future, it would be interesting (but challenging) to use the DQDs in quantum technologies. For such applications several DQDs would have to be contacted to each other, possibly by creating several DQDs inside one nanowire, and using different side gate pairs to control them (maybe inspired by Ref. [82]). The DQDs have advantages such as large level spacings, huge and controllable g-factors, and that a large number of QDs can be epitaxially grown in one structure [81]. However, if such applications are implemented is up to the future to show.

References

[1] Richard M. Martin. *Electronic Structure: Basic Theory and Practical Methods*. Cambridge University Press, 2004.

[2] Laszlo Solymar and Donald Walsh. *Electrical Properties of Materials*. Oxford University Press, 2004.

[3] Gianluca Stefanucci and Robert van Leeuwen. *Nonequilibrium Many-Body Theory of Quantum Systems: A Modern Introduction*. Cambridge University Press, 2013.

[4] Morten Willatzen and Lok C. Lew Yan Voon. *The kp Method*. Springer, Berlin Heidelberg, 2009.

[5] John H. Davies. *The Physics of Low-Dimensional Semiconductors*. Cambridge University Press, 1998.

[6] C.J. Foot. *Atomic Physics*. Oxford University Press, 2004.

[7] Roland Winkler. *Spin Orbit Coupling Effects in Two-Dimensional Electron and Hole Systems*. Springer, New York, 2003.

[8] I. Vurgaftman, J. R. Meyer, and L. R. Ram-Mohan. Band parameters for III-V compound semiconductors and their alloys. *Journal of Applied Physics*, 89:5815–5875, 2001.

[9] Y. Naveh and B. Laikhtman. Excitonic Instability and Electric-Field-Induced Phase Transition Towards a Two-Dimensional Exciton Condensate. *Physical Review Letters*, 77:900–903, 1996.

[10] Fabrizio Nichele, Morten Kjaergaard, Henri J. Suominen, Rafal Skolasinski, Michael Wimmer, Binh-Minh Nguyen, Andrey A. Kiselev, Wei Yi, Marko Sokolich, Michael J. Manfra, Fanming Qu, Arjan J. A. Beukman, Leo P. Kouwenhoven, and Charles M. Marcus. Giant spin-orbit splitting in inverted InAs/GaSb double quantum wells. *Physical Review Letters*, 118:016801, 2017.

[11] Chaoxing Liu, Taylor L. Hughes, Xiao Liang Qi, Kang Wang, and Shou Cheng Zhang. Quantum spin hall effect in inverted type-II semiconductors. *Physical Review Letters*, 100:236601–236604, 2008.

[12] Ivan Knez, Rui Rui Du, and Gerard Sullivan. Evidence for helical edge modes in inverted InAs/GaSb quantum wells. *Physical Review Letters*, 107:1–5, 2011.

[13] Malin Nilsson, Luna Namazi, Sebastian Lehmann, Martin Leijnse, Kimberly A. Dick, and Claes Thelander. Electron-hole interactions in coupled InAs-GaSb quantum dots based on nanowire crystal phase templates. *Physical Review B*, 94:115313, 2016.

[14] Bahram Ganjipour, Martin Leijnse, Lars Samuelson, H. Q. Xu, and Claes Thelander. Transport studies of electron-hole and spin-orbit interaction in GaSb/InAsSb core-shell nanowire quantum dots. *Physical Review B*, 91:161301, 2015.

[15] Lincoln J. Lauhon, Mark S. Gudiksen, Deli Wang, and Charles M. Lieber. Epitaxial core-shell and core-multishell nanowire heterostructures. *Nature (London)*, 420:57–61, 2002.

[16] Bozhi Tian, Xiaolin Zheng, Thomas J. Kempa, Ying Fang, Nanfang Yu, Guihua Yu, Jinlin Huang, and Charles M. Lieber. Coaxial silicon nanowires as solar cells and nanoelectronic power sources. *Nature (London)*, 449:885–889, 2007.

[17] Benedikt Mayer, Daniel Rudolph, Joscha Schnell, Stefanie Morkötter, Julia Winnerl, Julian Treu, Kai Müller, Gregor Bracher, Gerhard Abstreiter, Gregor Koblmüller, and Jonathan J. Finley. Lasing from individual GaAs-AlGaAs core-shell nanowires up to room temperature. *Nature Communications*, 4:2931, 2013.

[18] Martin Ek, B. Mattias Borg, Anil W. Dey, Bahram Ganjipour, Claes Thelander, Lars Erik Wernersson, and Kimberly A. Dick. Formation of the axial heterojunction in GaSb/InAs(Sb) nanowires with high crystal quality. *Crystal Growth & Design*, 11:4588–4593, 2011.

[19] Bahram Ganjipour, Martin Ek, B. Mattias Borg, Kimberly A. Dick, Mats-Erik Pistol, Lars-Erik Wernersson, and Claes Thelander. Carrier control and transport modulation in GaSb/InAsSb core/shell nanowires. *Applied Physics Letters*, 101:103501, 2012.

[20] Luna Namazi, Malin Nilsson, Sebastian Lehmann, Claes Thelander, and Kimberly A. Dick. Selective GaSb radial growth on crystal phase engineered InAs nanowires. *Nanoscale*, 7:10472–81, 2015.

[21] Stefan Birner. *Modeling of Semiconductor Nanostructures and Semiconductor - Electrolyte Interfaces*. PhD thesis, Technische Universität München, 2011.

[22] Evan O. Kane. Band structure of indium antimonide. *Journal of Physics and Chemistry of Solids*, 1:249–261, 1957.

[23] Thomas B. Bahder. Eight-band kp model of strained zinc-blende crystals. *Physical Review B*, 41:11992–12001, 1990.

[24] D. Gershoni, C. H. Henry, and G. A. Baraff. Calculating the Optical Properties of Multidimensional Heterostructures: Application to the Modeling of Quaternary Quantum Well Lasers. *IEEE Journal of Quantum Electronics*, 29:2433–2450, 1993.

[25] Bradley Foreman. Effective-mass Hamiltonian and boundary conditions for the valence bands of semiconductor microstructures. *Physical Review B*, 48:4964–4967, 1993.

[26] Per-Olov Löwdin. A note on the quantum mechanical perturbation theory. *The Journal of Chemical Physics*, 19:1396–1401, 1951.

[27] Jun Li, Wen Yang, and Kai Chang. Spin states in InAs/AlSb/GaSb semiconductor quantum wells. *Physical Review B*, 80:1–11, 2009.

[28] A. Zakharova, S. Yen, and K. Chao. Hybridization of electron, light-hole, and heavy-hole states in InAs/GaSb quantum wells. *Physical Review B*, 64, 2001.

[29] V. V. Ravi Kishore, N. Čukarić, B. Partoens, M. Tadić, and F. M. Peeters. Hole subbands in freestanding nanowires: six-band versus eight-band kp modelling. *Journal of Physics: Condensed Matter*, 24:135302, 2012.

[30] Ning Luo, Gaohua Liao, and H. Q. Xu. k.p theory of freestanding narrow band gap semiconductor nanowires. *AIP Advances*, 6:125109, 2016.

[31] Bradley A. Foreman. Elimination of spurious solutions from eight-band $\mathbf{k} \cdot \mathbf{p}$ theory. *Physical Review B*, 56:R12748–R12751, 1997.

[32] B. Lassen, R. V. N. Melnik, and M. Willatzen. Spurious solutions in the multiband effective mass theory applied to low dimensional nanostructures. *Communications in Computational Physics*, 6:699–729, 2009.

[33] P. C. Klipstein. Structure of the quantum spin Hall states in HgTe/CdTe and InAs/GaSb/AlSb quantum wells. *Physical Review B*, 91:035310, 2015.

[34] Lun Hui Hu, Chao Xing Liu, Dong Hui Xu, Fu Chun Zhang, and Yi Zhou. Electric control of inverted gap and hybridization gap in type-II InAs/GaSb quantum wells. *Physical Review B*, 94:1–7, 2016.

[35] Ning Luo, Guang-Yao Huang, Gaohua Liao, Lin-Hui Ye, and H. Q. Xu. Band-inverted gaps in InAs/GaSb and GaSb/InAs core-shell nanowires. *Scientific Reports*, 6:38698, 2016.

[36] E. Halvorsen, Y. Galperin, and K. Chao. Optical transitions in broken gap heterostructures. *Physical Review B*, 61:16743–16749, 2000.

[37] Milton Abramowitz. *Handbook of Mathematical Functions, With Formulas, Graphs, and Mathematical Tables,*. Dover Publications, Incorporated, 1974.

[38] Martin Leijnse and Karsten Flensberg. Introduction to topological superconductivity and Majorana fermions. *Semiconductor Science and Technology*, 27:124003, 2012.

[39] Alexander Altland and Martin R. Zirnbauer. Nonstandard symmetry classes in mesoscopic normal-superconducting hybrid structures. *Physical Review B*, 55:1142–1161, 1997.

[40] M. Z. Hasan and C. L. Kane. Colloquium: Topological insulators. *Reviews of Modern Physics*, 82:3045–3067, 2010.

[41] B.A. Bernevig and T.L. Hughes. *Topological Insulators and Topological Superconductors*. Princeton University Press, 2013.

[42] B. Andrei Bernevig, Taylor L. Hughes, and Shou-Cheng Zhang. Quantum Spin Hall Effect And Topological Phase Transition in HgTe Quantum Wells. *Science*, 314:1757–1761, 2006.

[43] C. L. Kane and E. J. Mele. Quantum Spin hall effect in graphene. *Physical Review Letters*, 95:1–4, 2005.

[44] Markus König, Steffen Wiedmann, Christoph Brüne, Andreas Roth, Hartmut Buhmann, Laurens W. Molenkamp, Xiao-liang Qi, and Shou-Cheng Zhang. Quantum Spin Hall Insulator State in HgTe Quantum Wells Markus. *Science*, 318:766–771, 2007.

[45] Y. Naveh and B. Laikhtman. Band-structure tailoring by electric field in a weakly coupled electron-hole system. *Applied Physics Letters*, 66:1980, 1995.

[46] Xiao-Liang Qi and Shou-Cheng Zhang. Topological insulators and superconductors. *Reviews of Modern Physics*, 83:1057–1110, 2011.

[47] Simon Wozny, Karel Vyborny, Wolfgang Belzig, and Sigurdur I. Erlingsson. Gap formation in helical edge states with magnetic impurities. *Physical Review B*, 98(16):1–6, 2018.

[48] C. L. Kane and E. J. Mele. Z2 topological order and the quantum spin hall effect. *Physical Review Letters*, 95:3–6, 2005.

[49] János K. Asbóth, László Oroszlány, and András Pályi. *A Short Course on Topological Insulators*. Springer, 2016.

[50] Di Xiao, Ming-Che Chang, and Qian Niu. Berry phase effects on electronic properties. *Reviews of Modern Physics*, 82:1959–2007, 2010.

[51] Ilse van Weperen, Sébastien R. Plissard, Erik P. A. M. Bakkers, Sergey M. Frolov, and Leo P. Kouwenhoven. Quantized Conductance in an InSb Nanowire. *Nano Letters*, 13:387–391, 2013.

[52] Steven Chuang, Qun Gao, Rehan Kapadia, Alexandra C. Ford, Jing Guo, and Ali Javey. Ballistic InAs nanowire transistors. *Nano Letters*, 13:555–558, 2013.

[53] Jakob Kammhuber, Maja C. Cassidy, Hao Zhang, Önder Gül, Fei Pei, Michiel W. A. de Moor, Bas Nijholt, Kenji Watanabe, Takashi Taniguchi, Diana Car, Sébastien R. Plissard, Erik P. A. M. Bakkers, and Leo P. Kouwenhoven. Conductance Quantization at Zero Magnetic Field in InSb Nanowires. *Nano Letters*, 16:3482–3486, 2016.

[54] L. D. Hicks and M. S. Dresselhaus. Thermoelectric figure of merit of a one-dimensional conductor. *Physical Review B*, 47:16631–16634, 1993.

[55] Mark Lundstrom. *Fundamentals of Carrier Transport*. Cambridge University Press, New York, 2nd edition, 2002.

[56] Neil W. Ashcroft and N. David Mermin. *Solid State Physics*. Saunders College, 1976.

[57] Melvin Cutler and N. F. Mott. Observation of Anderson localization in an electron gas. *Physical Review*, 181:1336–1340, 1969.

[58] R. Hanson, L. P. Kouwenhoven, J. R. Petta, S. Tarucha, and L. M. K. Vandersypen. Spins in few-electron quantum dots. *Rev. Mod. Phys.*, 79:1217–1265, Oct 2007.

[59] Thomas Ihn. *Semiconductor Nanostructures: Quantum States and Electronic Transport*. 2010.

[60] Andreas Fuhrer. *Phase coherence, orbital and spin states in quantum rings*. PhD thesis, ETH Zürich, 2003.

[61] Malin Nilsson. *Charge and Spin Transport in Parallel-Coupled Quantum Dots in Nanowires*. PhD thesis, Lund University, 2018.

[62] A. C. Johnson, J. R. Petta, C. M. Marcus, M. P. Hanson, and A. C. Gossard. Singlet-triplet spin blockade and charge sensing in a few-electron double quantum dot. *Phys. Rev. B*, 72:165308, Oct 2005.

[63] S. Nadj-Perge, S. M. Frolov, J. W. W. van Tilburg, J. Danon, Yu. V. Nazarov, R. Algra, E. P. A. M. Bakkers, and L. P. Kouwenhoven. Disentangling the effects of spin-orbit and hyperfine interactions on spin blockade. *Phys. Rev. B*, 81:201305, May 2010.

[64] J. Danon and Yu. V. Nazarov. Pauli spin blockade in the presence of strong spin-orbit coupling. *Phys. Rev. B*, 80:041301, Jul 2009.

[65] A. Pfund, I. Shorubalko, K. Ensslin, and R. Leturcq. Suppression of spin relaxation in an inas nanowire double quantum dot. *Phys. Rev. Lett.*, 99:036801, Jul 2007.

[66] A. Pfund, I. Shorubalko, K. Ensslin, and R. Leturcq. Spin-state mixing in inas double quantum dots. *Phys. Rev. B*, 76:161308, Oct 2007.

[67] T. Hatano, M. Stopa, and S. Tarucha. Single-electron delocalization in hybrid vertical-lateral double quantum dots. *Science*, 309(5732):268–271, 2005.

[68] T. Hatano, S. Amaha, T. Kubo, Y. Tokura, Y. Nishi, Y. Hirayama, and S. Tarucha. Manipulation of exchange coupling energy in a few-electron double quantum dot. *Phys. Rev. B*, 77:241301, Jun 2008.

[69] T. Hatano, T. Kubo, Y. Tokura, S. Amaha, S. Teraoka, and S. Tarucha. Aharonov-bohm oscillations changed by indirect interdot tunneling via electrodes in parallel-coupled vertical double quantum dots. *Phys. Rev. Lett.*, 106:076801, Feb 2011.

[70] T. Hatano, Y. Tokura, S. Amaha, T. Kubo, S. Teraoka, and S. Tarucha. Excitation spectroscopy of few-electron states in artificial diatomic molecules. *Phys. Rev. B*, 87:241414, Jun 2013.

[71] Dimitrije Stepanenko, Mark Rudner, Bertrand I. Halperin, and Daniel Loss. Singlet-triplet splitting in double quantum dots due to spin-orbit and hyperfine interactions. *Phys. Rev. B*, 85:075416, Feb 2012.

[72] J. Paaske, A. Andersen, and K. Flensberg. Exchange cotunneling through quantum dots with spin-orbit coupling. *Phys. Rev. B*, 82:081309, Aug 2010.

[73] Martin Leijnse. *Transport spectroscopy and control of molecular quantum dots*. PhD thesis, RWTH Aachen University, Aachen, 2009.

[74] C. W. Gardiner. *Quantum Noise*. Springer-Verlag, Berlin, 1993.

[75] C. W. J. Beenakker. Theory of coulomb-blockade oscillations in the conductance of a quantum dot. *Phys. Rev. B*, 44:1646–1656, Jul 1991.

[76] Liney Halla Kristinsdottir. *Interaction effects in the transport of particles in nanowire quantum dots*. PhD thesis, Lund University, 2015.

[77] J. J. Sakurai and Jim Napolitano. *Modern Quantum Mechanics*. Cambridge University Press, 2 edition, 2017.

[78] Ning Luo, Gaohua Liao, and H. Q. Xu. k.p theory of freestanding narrow band gap semiconductor nanowires. *AIP Advances*, 6(12):125109, 2016.

[79] Chetan Nayak, Steven H. Simon, Ady Stern, Michael Freedman, and Sankar Das Sarma. Non-abelian anyons and topological quantum computation. *Rev. Mod. Phys.*, 80:1083–1159, Sep 2008.

[80] Heidi Potts, Martin Leijnse, Adam Burke, Malin Nilsson, Sebastian Lehmann, Kimberly A. Dick, and Claes Thelander1. Selective tuning of spin-orbital Kondo contributions in parallel-coupled quantum dots. pages 1–8, 2019.

[81] H Potts, I.-J. Chen, A Tsintzis, M Nilsson, S Lehmann, K A Dick, M Leijnse, and C Thelander. Electrical control of spins and giant g-factors in ring-like coupled quantum dots. *Nature Communications*, 10(1):5740, 2019.

[82] D. Barker, S. Lehmann, L. Namazi, M. Nilsson, C. Thelander, K. A. Dick, and V. F. Maisi. Individually addressable double quantum dots formed with nanowire polytypes and identified by epitaxial markers. *Applied Physics Letters*, 114(18), 2019.

[83] B. Lassen, M. Willatzen, R. Melnik, and Lok C. Lew Yan Voon. Electronic structure of free-standing InP and InAs nanowires. *J. Mater. Res.*, 21:2927–2935, 2006.

Appendix

Appendix A

Kane Hamiltonian for the [111] direction

In Papers I and II we consider nanowires grown in the [111] crystallographic direction. When calculating for a nanowire grown in another crystal direction than [001], we need to rotate the coordinate system. The reason for this is that for the Kane Hamiltonian in Eq. 2.11 it is assumed that the x, y and z axes align with the crystallograpic [100], [010] and [001] directions, respectively. This means that we rotate the coordinate system such that the original z axis, pointing in the [001] direction, will be rotated into z', pointing in the [111] direction. We follow the rotation process from Refs. [4, 83, 30], and rotate the coordinate system by the azimuthal and the polar angles ϕ and θ, respectively, see Fig. A.1.

The Kane Hamiltonian for the [111] direction is given by

$$H_{[111]} = S^* W^* H_0^{rot} W^\dagger S^\dagger + H_{SO} \tag{A.1}$$

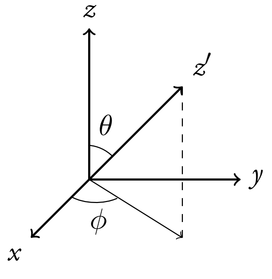

Figure A.1: Original coordinate system and the rotated z' axis.

where H_0^{rot} is the Kane Hamiltonian, without the spin-orbit part H_{SO}, given in in Eqs. 2.11–2.12, with rotated coordinates ($k_i \to k_i'$). In Fig. A.1 we show this rotation of coordinates. The diagonal, non-k-dependent part of H_0, and the full spin-orbit matrix H_{SO} are invariant under rotations. The matrix W is a rotation matrix, and the matrix S accounts for an additional change of the basis to

$$\{|S\uparrow\rangle, |S\downarrow\rangle, |HH\uparrow\rangle, |LH\uparrow\rangle, |LH\downarrow\rangle, |HH\downarrow\rangle, |SO\uparrow\rangle, |SO\downarrow\rangle\}. \tag{A.2}$$

This basis relates to the original one in Eq. 2.8 according to Eq. 2.10.

The rotation matrix W is given by

$$W = A\hat{U}, \tag{A.3}$$

with

$$A = \begin{pmatrix} e^{-i\frac{\phi}{2}} \cos\frac{\theta}{2} \mathbb{1}_{4\times4} & e^{i\frac{\phi}{2}} \sin\frac{\theta}{2} \mathbb{1}_{4\times4} \\ -e^{-i\frac{\phi}{2}} \sin\frac{\theta}{2} \mathbb{1}_{4\times4} & e^{i\frac{\phi}{2}} \cos\frac{\theta}{2} \mathbb{1}_{4\times4} \end{pmatrix}, \tag{A.4}$$

$$\hat{U} = \begin{pmatrix} 1 & 0 & 0 & 0 \\ 0 & U & 0 & 0 \\ 0 & 0 & 1 & 0 \\ 0 & 0 & 0 & U \end{pmatrix}, \tag{A.5}$$

and

$$U = \begin{pmatrix} \cos\phi\cos\theta & \sin\phi\cos\theta & -\sin\theta \\ -\sin\phi & \cos\phi & 0 \\ \cos\phi\sin\theta & \sin\phi\sin\theta & \cos\theta \end{pmatrix}. \tag{A.6}$$

The resulting Hamiltonian for the $[111]$ direction (with N symmetrized and $B = 0$) is given by

$$H = \left(\begin{array}{c|c|c} H_{CC} & H_{CV8} & H_{CV7} \\ \hline \dagger & H_{V8V8} & H_{V8V7} \\ \hline \dagger & \dagger & H_{V7V7} \end{array}\right), \tag{A.7}$$

with

$$H_{CC} = (E_c + k_x A k_x + k_y A k_y + k_z A k_z)\mathbb{1}_{2\times2}, \tag{A.8}$$

$$H_{CV8} = \begin{pmatrix} i\frac{1}{\sqrt{2}}Pk_+ & -i\sqrt{\frac{2}{3}}Pk_z & -i\frac{1}{\sqrt{6}}Pk_- & 0 \\ 0 & i\frac{1}{\sqrt{6}}Pk_+ & -i\sqrt{\frac{2}{3}}Pk_z & i\frac{1}{\sqrt{2}}Pk_- \end{pmatrix}, \tag{A.9}$$

$$H_{CV7} = \begin{pmatrix} i\frac{1}{\sqrt{3}}Pk_z & -i\frac{1}{\sqrt{3}}Pk_- \\ i\frac{1}{\sqrt{3}}Pk_+ & i\frac{1}{\sqrt{3}}Pk_z \end{pmatrix}, \tag{A.10}$$

$$
\begin{aligned}
&H_{V8V8} = \\
&\frac{1}{6}\begin{pmatrix} N(\mathbf{k}^2 - 3k_z^2) & H^{1,2}_{V8V8} & H^{1,3}_{V8V8} & 0 \\ \dagger & -N(\mathbf{k}^2 - 3k_z^2) & 0 & -H^{1,3}_{V8V8} \\ \dagger & \dagger & -N(\mathbf{k}^2 - 3k_z^2) & H^{1,2}_{V8V8} \\ \dagger & \dagger & \dagger & N(\mathbf{k}^2 - 3k_z^2) \end{pmatrix} \\
&+ \frac{1}{6}(6E_v' + 2\Gamma_1 \mathbf{k}^2)\,\mathbb{1}_{4\times 4},
\end{aligned}
$$

$$
H_{V8V7} = \begin{pmatrix} -\frac{1}{6\sqrt{2}} H^{1,2}_{V8V8} & \frac{1}{3\sqrt{2}} H^{1,3}_{V8V8} \\ \frac{N}{3\sqrt{2}}(\mathbf{k}^2 - 3k_z^2) & \sqrt{3} H^{1,1}_{V8V7} \\ H^{3,1}_{V8V7} & H^{2,1}_{V8V7} \\ H^{4,1}_{V8V7} & -\frac{1}{\sqrt{3}} H^{3,1}_{V8V7} \end{pmatrix}, \tag{A.11}
$$

and

$$
H_{V7V7} = \frac{1}{3}(3E_v' - 3\Delta + \Gamma_1 \mathbf{k}^2)\,\mathbb{1}_{2\times 2}. \tag{A.12}
$$

The matrix elements are given by

$$
H^{1,2}_{V8V8} = \frac{1}{\sqrt{6}}[2(\Gamma_2 - N)k_+^2 - \sqrt{2}(2\Gamma_2 + N)\{k_-, k_z\}] \tag{A.13}
$$

$$
H^{1,3}_{V8V8} = \frac{1}{\sqrt{3}}[-(\Gamma_2 + 2N)k_-^2 + \sqrt{2}(\Gamma_2 - N)\{k_+, k_z\}] \tag{A.14}
$$

$$
H^{3,1}_{V8V7} = \frac{1}{6}\left[(\Gamma_2 - N)k_-^2 - \frac{1}{\sqrt{2}}(2\Gamma_2 + N)\{k_+, k_z\}\right] \tag{A.15}
$$

$$
H^{4,1}_{V8V7} = \frac{1}{3\sqrt{6}}\left[(\Gamma_2 + 2N)k_+^2 - \sqrt{2}(\Gamma_2 - N)\{k_-, k_z\}\right]. \tag{A.16}
$$

The terms of the form Qk_i^2 are to be interpretated as $k_i Q k_i$, $\{k_i, k_j\} = k_i k_j + k_j k_i$ denotes the anti-commutator, and

$$
\begin{aligned}
\Gamma_1 &= L + 2M \\
\Gamma_2 &= L - M.
\end{aligned}
$$